



Studies Toward a Demonstration of Relativistic Electron  
Beam Energy Modulation by Interaction with Terahertz  
Radiation in Free Space

Thesis submitted in accordance with the requirements of  
the University of Liverpool for the degree of Doctor in Philosophy by

**David Holder**

March 2013



# Abstract

This thesis details the experimental studies leading to initial attempts to measure an interaction in free space between a short pulse of terahertz radiation (generated from a 40 fs, 800 nm titanium-sapphire (Ti:S) laser pulse) and bunches of medium-energy relativistic electrons within the ALICE accelerator [1]. The work undertaken included optimization of the terahertz source itself, which is a large-area photoconductive antenna with high-voltage electrodes; the aim being to maximize the potential that can be applied before breakdown occurs. The key feature of such terahertz sources is the radially-polarized ( $\text{TEM}_{10}$ -like) nature of the radiation generated. Further work included characterization of the temporal structure and transverse profile of the terahertz radiation pulse in the ALICE Diagnostics Room; duplication of this experimental arrangement inside the ALICE accelerator; modification of the operating parameters of ALICE to produce the most conducive situation for detecting an interaction. The final step was the installation of additional electron beam diagnostics and the experimental search for a definite interaction signal. The work described in this thesis is part of a project named *ALICE Energy Modulation Induced by Terahertz Radiation*, also known as *AEMITR*.



# Contents

<b>Abstract</b>	<b>iii</b>
<b>Contents</b>	<b>v</b>
<b>List of Figures</b>	<b>ix</b>
<b>List of Tables</b>	<b>xii</b>
<b>Acknowledgements</b>	<b>xiii</b>
<b>1 Overview</b>	<b>1</b>
1.1 Introduction . . . . .	1
1.2 The Lawson-Woodward theorem . . . . .	4
1.3 Radially-polarized EM waves . . . . .	6
1.3.1 Introduction . . . . .	6
1.3.2 Radially-polarized terahertz pulses . . . . .	8
1.3.3 Terahertz generation from antennae . . . . .	10
1.3.4 Radially-polarized terahertz generation from antennae . . . . .	11
1.3.5 Modelling the terahertz radiation field from rotationally-symmetric antennae (DN) . . . . .	13
1.4 Detection and measurement of terahertz radiation . . . . .	15
1.4.1 Introduction . . . . .	15
1.4.2 Terahertz generation and measurement apparatus . . . . .	16
1.5 Examples of experimental results . . . . .	19
1.5.1 Calibration of the terahertz electric field (DL) . . . . .	19
1.5.2 Calculation of the transmission through a ZnTe crystal and crossed polarizer in the presence of terahertz radiation (SPJ) . . . . .	22
1.5.3 Sources of departure from the ideal case . . . . .	24
1.6 Modelling the interaction of the terahertz radiation with the electron beam (AW) . . . . .	25
1.7 Overview of thesis layout . . . . .	26
1.8 Chapter summary . . . . .	28
<b>2 Modelling and Optimization of the Antenna Design</b>	<b>29</b>
2.1 Introduction . . . . .	29
2.2 Problems with the existing antenna design . . . . .	30
2.3 Improvements to the antenna design and its operation . . . . .	30
2.3.1 Pulsed power supply . . . . .	31

2.3.2	Electrode profile . . . . .	33
2.3.3	Optimization of the geometry . . . . .	33
2.3.4	Final design used . . . . .	38
2.3.5	Further enhancements . . . . .	39
2.4	Antenna construction . . . . .	41
2.4.1	Attachment of the electrodes . . . . .	41
2.4.2	Electrical connections . . . . .	42
2.5	Results . . . . .	42
2.6	Chapter summary . . . . .	43
<b>3</b>	<b>Measurements in the ALICE Diagnostics Room</b>	<b>45</b>
3.1	Introduction . . . . .	45
3.2	Experimental arrangement . . . . .	46
3.3	Laser operation . . . . .	48
3.4	Analysis of the experimental measurements (DL) . . . . .	49
3.4.1	Calibration of the terahertz electric field as a function of the quarter-waveplate angle at minimum intensity . . . . .	49
3.4.2	Measurement of the terahertz electric field across the ZnTe crystal	50
3.4.3	Terahertz electric field as a function of the antenna alignment . . .	51
3.4.4	Terahertz electric field as a function of the antenna voltage . . . .	52
3.4.5	Terahertz electric field as a function of pump laser intensity . . . .	52
3.5	Chapter summary . . . . .	54
<b>4</b>	<b>Set Up and Assembly of the Equipment in the ALICE Accelerator Hall</b>	<b>55</b>
4.1	Introduction . . . . .	55
4.2	Terahertz generation . . . . .	56
4.2.1	Laser beam transport . . . . .	57
4.2.2	Optical tables for terahertz generation and measurement . . . . .	60
4.3	Accelerator modifications for AEMITR . . . . .	61
4.3.1	Interaction hardware . . . . .	62
4.3.2	Terahertz electric field strength measurement . . . . .	63
4.3.3	Additional electron beam diagnostics . . . . .	63
4.3.4	Electron beam - laser synchronization . . . . .	65
4.4	Alignment of new components and establishment of the experimental axis	66
4.5	Selection of ALICE beam parameters . . . . .	68
4.5.1	Beam energy and energy spread . . . . .	68
4.5.2	Bunch charge and bunch length . . . . .	70
4.5.3	Emittance . . . . .	71
4.5.4	Train repetition rate and the number of bunches per train . . . . .	71
4.5.5	Beam stability . . . . .	71
4.5.6	Summary of ALICE electron beam parameters . . . . .	72
4.6	ALICE electron optics for AEMITR (AW) . . . . .	72
4.6.1	Reconciliation of the MAD model with beam measurements . . . . .	74
4.6.2	Quadrupole scans in Straight 2 . . . . .	74
4.6.3	Dispersion measurements . . . . .	80
4.6.4	Tomography measurements in the ALICE-to-EMMA injection line	80

4.7	Chapter summary . . . . .	82
<b>5</b>	<b>Measurements in the ALICE Accelerator Hall</b>	<b>83</b>
5.1	Introduction . . . . .	83
5.2	Terahertz field strengths using the ZnTe crystal integrated into ALICE . .	83
5.2.1	Initial measurements . . . . .	84
5.2.2	Investigation into the degree of polarization . . . . .	86
5.2.3	Initial terahertz electric field strength measurements . . . . .	87
5.2.4	Investigation into the effect of transverse alignment of the terahertz and probe beams . . . . .	87
5.2.5	Terahertz signal as a function of antenna voltage . . . . .	93
5.2.6	Signal as a function of terahertz focussing . . . . .	93
5.2.7	Investigation of the signal as a function of the transverse antenna alignment . . . . .	96
5.2.8	Effect of part-illumination of the antenna . . . . .	96
5.3	ALICE beam set up and measurement . . . . .	99
5.3.1	Establishment of the basic beam parameters . . . . .	99
5.3.2	RF system settings . . . . .	99
5.3.3	Obtaining the desired beam waists via quadrupole scans (AW) . .	102
5.3.4	Dispersion measurements . . . . .	105
5.3.5	Steering through the apertures in Straight 2 . . . . .	105
5.3.6	Setting up laser-accelerator synchronization . . . . .	107
5.4	Searches for interaction between the terahertz radiation and the electron beam . . . . .	109
5.4.1	Introduction . . . . .	109
5.4.2	Measurements on 6/11/11 . . . . .	110
5.4.3	Measurements on 24/11/11 . . . . .	118
5.5	Chapter summary . . . . .	121
<b>6</b>	<b>Summary and Conclusions</b>	<b>123</b>
6.1	Introduction . . . . .	123
6.2	Is there any signal demonstrating interaction between terahertz radiation and electron bunches? . . . . .	124
6.3	Why did we not see a signal demonstrating interaction? . . . . .	124
6.3.1	Poor signal-to-noise ratio . . . . .	124
6.3.2	Apparent failure to replicate the terahertz radiation electric field strength measured in the ALICE Diagnostics Room inside the ALICE accelerator . . . . .	125
6.3.3	Inadequate spatial alignment of the terahertz radiation and the electron beam . . . . .	127
6.3.4	Inadequate synchronization . . . . .	127
6.4	Chapter summary . . . . .	127
	<b>Bibliography</b>	<b>129</b>



## List of Figures

1.1	New Straight 2 components . . . . .	3
1.2	Coordinate convention . . . . .	6
1.3	Transverse sections of electric field (1) . . . . .	8
1.4	Transverse sections of electric field (2) . . . . .	9
1.5	Longitudinal sections of electric field . . . . .	9
1.6	Terahertz pulses generation . . . . .	11
1.7	Radiation field generated by a converging pump laser . . . . .	12
1.8	Nearly-complete antenna assembly . . . . .	13
1.9	Terahertz electric field from wafer breakdown . . . . .	15
1.10	Schematic of the terahertz generation and detection apparatus . . . . .	17
1.11	Schematic of the terahertz generation with camera detection . . . . .	18
1.12	Schematic of the terahertz generation with photodiode detection . . . . .	19
1.13	Images of the ZnTe crystal vs. time . . . . .	20
1.14	Lock-in amplifier sum voltage at 50 kV . . . . .	20
1.15	Calculated probe beam intensity . . . . .	22
1.16	Quarter-wave plate angle at the minima . . . . .	23
1.17	Calculated probe beam intensity (1) . . . . .	23
1.18	Calculated probe beam intensity (2) . . . . .	24
1.19	Simulated effect of energy modulation on electron beam size . . . . .	25
1.20	Simulated effect of modulation on electron beam energy spread and profile . . . . .	26
1.21	Simulated effect of energy modulation on H and V electron beam size . . . . .	27
2.1	Initial antenna design . . . . .	30
2.2	High-voltage power supply . . . . .	31
2.3	Antenna enclosure . . . . .	32
2.4	Probe circuitry inside antenna enclosure . . . . .	32
2.5	Ideal and actual centre electrode geometries . . . . .	33
2.6	Outer electrode . . . . .	34
2.7	Wafer electric field strengths . . . . .	35
2.8	Initial Opera geometry . . . . .	35
2.9	Opera simulation results . . . . .	36
2.10	Improved Opera region definition . . . . .	36
2.11	Opera simulation of asymmetric centre electrode . . . . .	37
2.12	Asymmetric centre electrode simulation results . . . . .	37
2.13	Opera radial field simulation results . . . . .	38
2.14	Opera model of the final design . . . . .	38
2.15	Opera simulation of the final design . . . . .	39
2.16	Cross-section through the final antenna design . . . . .	39
2.17	Opera 2D model of potential future electrode geometries . . . . .	40
2.18	Opera simulation of potential future electrode geometries . . . . .	40

2.19	Stages of antenna assembly . . . . .	41
2.20	Detail of electrical connection . . . . .	42
3.1	A schematic of the optical setup used in the ALICE Diagnostics Room . . . . .	46
3.2	Photomontage of the optical table in the ALICE Diagnostics Room . . . . .	48
3.3	Probe beam intensity at three different quarter-waveplate angles . . . . .	49
3.4	Terahertz electric field strength as a function of quarter-wave plate angle . . . . .	50
3.5	ZnTe crystal images vs. terahertz and probe beam timing . . . . .	51
3.6	Calculated terahertz electric field strength . . . . .	51
3.7	Terahertz electric field strength at ten points in a horizontal line . . . . .	52
3.8	Terahertz pulse intensity vs. timing . . . . .	53
3.9	Integrated terahertz pulse intensity as a function of antenna voltage . . . . .	53
3.10	Terahertz electric field strength vs. laser power . . . . .	54
4.1	Layout of the ALICE complex . . . . .	56
4.2	Laser beam transport from Area 1 to Area 2 . . . . .	57
4.3	A section of the completed laser beam transport system . . . . .	59
4.4	Schematic of the two optical tables in ALICE Area 2 . . . . .	60
4.5	Composite photograph of terahertz-generation optical table . . . . .	61
4.6	New and original accelerator components used by the AEMITR project . . . . .	62
4.7	ST2-LM-YAG-01 assembly . . . . .	63
4.8	New AEMITR accelerator components in Straight 2 of ALICE . . . . .	64
4.9	ST2-DIA-YAG-01, illuminated by light scattered inside ALICE . . . . .	65
4.10	Laser-electron timing synchronization in Straight 2 of ALICE . . . . .	66
4.11	Alignment of the mirror and aperture plate apertures in ALICE . . . . .	68
4.12	Transverse particle displacement resulting from energy modulation . . . . .	69
4.13	Example Twiss parameters for ALICE configured for AEMITR . . . . .	73
4.14	ALICE beam transport components relevant for AEMITR . . . . .	73
4.15	Layout of Straight 2, showing components used for quadrupole scanning . . . . .	75
4.16	Example of Gaussian curve fitting to a screen image . . . . .	75
4.17	Example of Gaussian curve fitting to horizontal quadrupole scan data . . . . .	76
4.18	Example of Gaussian curve fitting to vertical quadrupole scan data . . . . .	77
4.19	A comparison of measured and calculated Twiss parameters . . . . .	79
4.20	The layout of the ALICE-to-EMMA injection line . . . . .	81
4.21	Beam images from the three consecutive screens in the EMMA injection line . . . . .	81
5.1	First image of the probe beam illuminating the ZnTe crystal inside ALICE . . . . .	85
5.2	ZnTe crystal image from the first attempt to generate and detect terahertz . . . . .	85
5.3	Positions of the first Glan–Thompson prism . . . . .	86
5.4	Results from polarization measurements in two locations . . . . .	87
5.5	Photodiode output showing a possible weak signal . . . . .	88
5.6	Probe and pump beams overlapping on the ZnTe crystal . . . . .	89

5.7	Pump beam (antenna removed) motion on ZnTe crystal as a function of ITO motor position . . . . .	89
5.8	Terahertz signal vs. relative timing as function of ITO motor position . . . .	90
5.9	Terahertz signal vs. optical delay line translation stage position . . . . .	91
5.10	Terahertz signal as function of ITO horizontal motor position . . . . .	91
5.11	Terahertz signal as function of ITO vertical motor position . . . . .	92
5.12	Terahertz signal after ITO alignment optimization . . . . .	92
5.13	Terahertz signal as the antenna voltage is increased from 80 to 130 kV . . .	93
5.14	Terahertz signal vs. optical delay line translation stage position at 130 kV .	93
5.15	Terahertz signal vs. optical delay stage and terahertz focus positions (1) . .	94
5.16	Terahertz signal vs. optical delay stage and terahertz focus positions (2) . .	95
5.17	Terahertz signal vs. optical delay stage and HV enclosure positions (1) . . .	97
5.18	Terahertz signal vs. optical delay stage and HV enclosure positions (2) . . .	97
5.19	Terahertz signal vs. optical delay line translation stage position and antenna part-illumination (1) . . . . .	98
5.20	Terahertz signal vs. optical delay line translation stage position and antenna part-illumination (2) . . . . .	98
5.21	Image of the electron beam on screen INJ-DIA-YAG-05 . . . . .	101
5.22	Image of the electron beam on screen AR1-DIA-OTR-01 . . . . .	101
5.23	Screen images from ST2-DIA-OTR-01 vs. quadrupole ST2-MAG-QUAD-02 gradient . . . . .	102
5.24	$\sigma^2$ vs $(1 - k_1L)$ , for both horizontal and vertical directions . . . . .	103
5.25	Comparison of Twiss parameters derived from screen measurements with the MAD model values . . . . .	104
5.26	Electron beam improvement from manual quadrupole adjustment . . . . .	104
5.27	Images of the electron beam on ST2-DIA-YAG-01 . . . . .	107
5.28	BPM and photodiode signal on oscilloscope . . . . .	107
5.29	Electron to terahertz timing measurement scheme . . . . .	108
5.30	Coherent Synchrolock-AP calibration . . . . .	109
5.31	Electron-terahertz interaction scan (7) . . . . .	111
5.32	Electron-terahertz interaction scan (1) . . . . .	112
5.33	Electron-terahertz interaction scan (2) . . . . .	113
5.34	Electron-terahertz interaction scan (3) . . . . .	114
5.35	Electron-terahertz interaction scan (4), when signal was expected . . . . .	115
5.36	Electron-terahertz interaction scan (5) . . . . .	116
5.37	Electron-terahertz interaction scan (6) . . . . .	117
5.38	Electron-terahertz interaction scan (8), when signal was expected . . . . .	118
5.39	Electron-terahertz interaction scan (9), with terahertz focus moved . . . . .	119
5.40	Electron-terahertz interaction scan (10), with terahertz focus moved and no aperture plate . . . . .	120
5.41	Electron-terahertz interaction scan (11), with the pump laser off . . . . .	120

## List of Tables

1.1	Laser and wafer parameters used for simulation . . . . .	14
4.1	Initial vessel survey positions before re-alignment . . . . .	67
4.2	Fixed machine and beam parameters used for calculations . . . . .	70
4.3	ALICE machine settings for AEMITR experiments . . . . .	72
4.4	An example of the results of the analysis of quadrupole scan data . . . . .	76
5.1	Key to figure 5.8 . . . . .	90
5.2	Key to figure 5.15 . . . . .	94
5.3	Key to figure 5.16 . . . . .	95
5.4	Twiss parameters and emittance from analysis of quadrupole scans . . . . .	103
5.5	Dispersion calculation using the average beam centroid position . . . . .	105
5.6	Dimensions and timings for synchronization measurement . . . . .	108
5.7	Experimental data sets recorded on 6/11/11 . . . . .	111

# Acknowledgements

The author wishes to thank his supervisors, Profs. Andrzej Wolski and John Dainton for their help and support with this project and STFC who funded his time as a student. In addition to those individuals credited below for their individual contributions to the project, the author would like to thank the myriad individuals within the Cockcroft Institute, ASTeC and Daresbury Laboratory as a whole who played some part in it.

The work reported in this thesis is the combination of contributions from many talented individuals; where appropriate their work is explicitly flagged with their initials. In general, Prof. Andrzej Wolski (AW) led the project and was responsible for many of the accelerator physics contributions as well as being an all-round physics sage; Dr. Steven Jamison (SPJ) whose crazy idea it was in the first place and without whose laser expertise and (sometimes) unfounded optimism nothing would have been achieved; Dr. David Newton (DN) valiantly attempted to simulate the underlying physics and reproduce the experimental measurements from first principles (these three individuals seemingly having the ability to switch seamlessly between the real world and some kind of Maxwellian-Equation space without pausing); Drs. David Laundry (DL) and Trina Thakker (TT) with whom the author spent many (happy) hours in darkened rooms and uncomfortable eye-wear. Rob Smith (RS) developed the high-voltage pulsed power supply. Yuri Saveliev (YS) provided both advice and practical expertise in setting up the ALICE accelerator in order to have the best chance possible of getting a result.

In order to provide a complete picture of this experiment, it was necessary to include some work undertaken primarily by someone other than the author. Where this is the case, the section heading includes the initials (the key to which can be found in the text above) of the person primarily responsible for the work recorded in that section; any figure not produced by the author is similarly acknowledged, in such cases where it is referenced in the body text. Nonetheless all the actual text was written by the author himself.



# Chapter 1

## Overview

### 1.1 Introduction

This chapter provides an introduction to the experiment that was undertaken, including analysis of the present state of the art and an outline of the theoretical basis for the experimental results recorded later. Subsequent chapters will:

- Record the work done by the author in modelling and optimizing the terahertz-generating antenna;
- Record the experimental work done to characterize the improved antenna design and to verify the experimental procedure used to measure the electric field strength of the terahertz radiation thus produced;
- List the work done to the ALICE accelerator, both in terms of hardware changes and the establishment of new operating regimes, required for the experiment to be a measurable success;
- Record the experimental work done with the ALICE accelerator, for both establishing in-situ terahertz generation and measurement, and searches for interaction between the terahertz radiation and the electron beam;
- Analyse what was achieved and what might be possible in the future.

The manipulation of the properties of an electron beam within an accelerator by the interaction with a laser beam is a well-established technique. It has been applied to provide beam heating [2], seeding of Free-Electron Lasers (FEL) [3] and for storage ring beam slicing [4]. Developments in this field are being widely pursued due to their importance in the development of future light-source facilities. Existing implementations have almost universally employed optical or near-IR laser beams and the interaction between the electrons and the laser beam has been coupled via a magnetic field provided by an undulator. Laser beam heating is employed to increase the electron beam's intrinsic energy spread in order to mitigate the adverse effects of coherent interactions within the electron bunch. In FEL seeding schemes the oscillating electric field of the laser

promotes the development of a particular mode in the FEL process, rather than relying on the amplification of random noise components, thus significantly reducing the length of undulator required. The long electron bunches in storage rings can have a localized modulation of the electron energy spread induced by the few femtosecond electric field oscillations of a laser pulse of several tens of femtoseconds long. This allows a small section of the bunch to be isolated in order to generate much shorter pulses of synchrotron radiation than are obtained from a whole bunch.

This thesis details the experimental studies leading to attempts to measure an interaction in *free space* between a short pulse of terahertz radiation (generated from a 40 fs, 800 nm titanium-sapphire (Ti:S) laser pulse) and bunches of medium energy electrons within the ALICE [1, 5] accelerator. Once demonstrated, the induced energy modulation from such an interaction could, for example, be converted into micro-bunching of the electron bunch via a suitable magnetic compression chicane. Such micro electron bunches would be very bright sources of coherent synchrotron radiation or the ideal drive beam for an FEL.

The initial work concentrated on the optimization of the terahertz sources themselves, which are based on large-area photoconductive antennae with high-voltage electrodes shaped to maximize the potential that can be applied before breakdown occurs. The key feature of such terahertz sources is their ability to generate radially polarized (TEM<sub>10</sub>-like) radiation, whose temporal structure and transverse profile were characterized in the ALICE Diagnostics Room.

The next step was to replicate the terahertz source characterization experimental equipment, not just in the ALICE accelerator hall but within the accelerator itself, thus allowing the measurements to be made at the nominal point of interaction between the terahertz pulse and the electrons. The capability to operate the equipment remotely was also added, so that the measurements could be made when the accelerator was searched-up (all personnel excluded and safety interlocks set) and operating.

In order to maximize the signal from any interaction between the electron beam and the terahertz pulse it was necessary to develop a particular set of electron beam parameters and then reliably reproduce these conditions each time they were required. A dependable means of synchronizing the electron bunches and the terahertz pulses, both spatially and temporally, was also required.

Modifications to the ALICE accelerator itself were also designed and installed. Figure 1.1 shows schematically the key new components for AEMITR placed in Straight 2 of ALICE. As well as adding a terahertz source, additional screens and chambers were installed in ALICE in order to:

1. Allow the combination of the terahertz radiation with the electron beam;
2. Allow in-situ temporal and spatial characterization of the terahertz radiation within the ALICE beam pipe;
3. Measure the position of a single electron bunch at the nominal interaction point;

4. Provide the option of halting the co-propagation of terahertz radiation and electron beam by introducing a terahertz-diffracting aperture;
5. Provide signals from the electron bunches and laser system in order to synchronize their passage;
6. Detect any change in the energy distribution of the electrons after the interaction via measurement of spatial profile of the electron bunch.

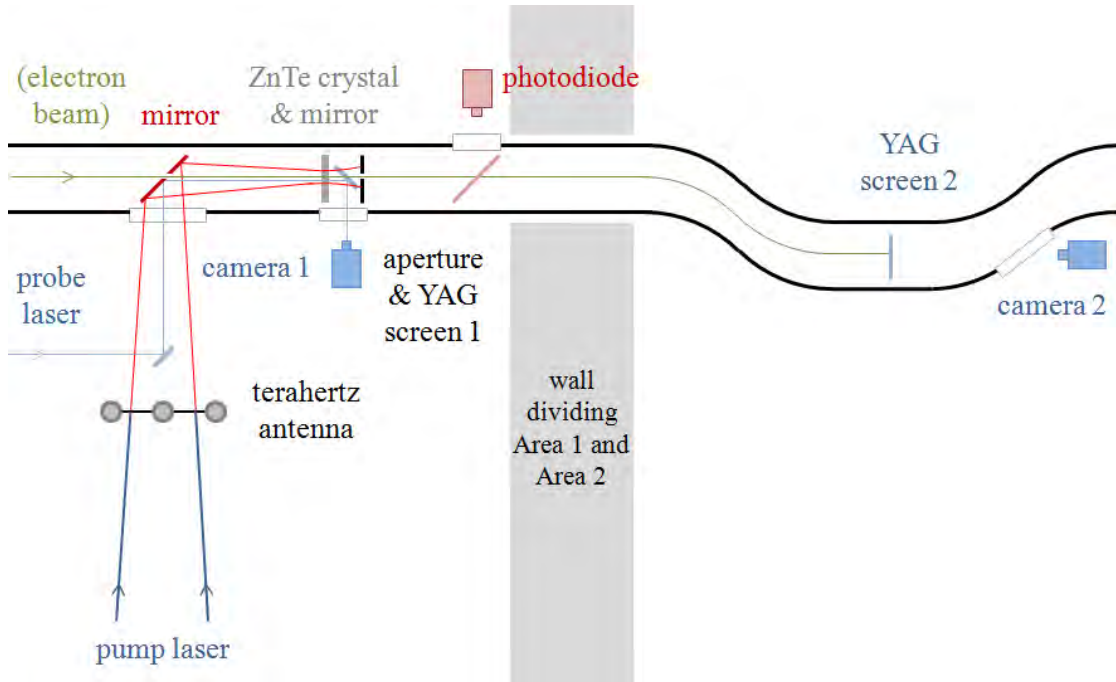


FIGURE 1.1: The key new components for AEMITR placed in Straight 2 of ALICE

For this experiment to have been a success the critical issues were:

1. Generation of a terahertz pulse with sufficiently high longitudinal electric field inside the accelerator;
2. Establishment of suitable electron beam properties (principally stable low emittance and energy spread);
3. Steering both the electron and terahertz beams so that they co-propagate along the same axis within the accelerator;
4. Achieving picosecond synchronization of the terahertz pulse with the electron bunch;
5. Installation of adequate electron beam diagnostics to detect any interaction.

Secondary issues included implementation of electron beam optics that were optimized to maximize the interaction with the terahertz whilst simultaneously giving a

reasonable chance of detecting any interaction further downstream and establishment of these optics and electron beam properties reproducibly whenever the opportunity for experimental studies was available.

## 1.2 The Lawson-Woodward theorem

The idea that there can be no net energy gain by a charged particle from an Electro-Magnetic (EM) wave in a free-space vacuum has become known as the Lawson-Woodward (LW) theorem, with [6, 7] being the two papers most commonly referenced. The usefulness of this idea is somewhat limited as it only holds in an ideal case and the ideal case cannot be tested experimentally. Amongst the restrictions that must hold for the LW theorem to be true are:

1. The interaction region is infinite;
2. The EM wave fills the infinite interaction region;
3. No static magnetic or electric fields are present;
4. The interaction region is a vacuum;
5. There are no boundaries present in the interaction region.

In addition, the force on a particle of charge  $e$  and velocity  $\mathbf{v}$  co-propagating with an EM wave ( $-e\mathbf{v} \times \mathbf{B}$ ) is also excluded from the LW theorem.

Without the application of Radio-Frequency (RF) cavities to accelerate charged particles the modern era of particle accelerators could not exist. This is clearly an extreme example of a regime that violates restrictions 1, 2 and 5. However, most discussion of the applicability of the LW theorem concentrates on attempts to accelerate electrons (usually) with the high-power beams available from optical lasers. A modern table-top laser can produce peak powers of several tens of terawatts for femtosecond-scale pulses, with very large electric fields generated at the focus. With the relentless drive to extend the particle accelerator energy frontier, and its associated increases in size and cost, the motivation to make practical use of these fields is obvious.

Although the LW theorem is much quoted and its implications debated [8, 9], it would appear that it is more akin to folklore than science. Neither of the author's original papers [6, 7] make any claim for the existence of such a theorem; and it would appear that subsequent authors have rather lazily referred to the "LW theorem" without reading the references they cite themselves. However, for the purposes of this thesis we will go along with the idea that the LW theorem is a useful idea, as much of the work published in this field is predicated on its existence.

The two major obstacles to direct acceleration of charged particles by EM waves are:

- In a plane EM wave the electric field is perpendicular to the propagation direction (and thus perpendicular to the direction we would wish the acceleration to be in);

- In vacuum the wave will have velocity  $c$ ; any particle that could potentially be accelerated will have a velocity less than  $c$  so there is an inevitable phase slippage between the two.

An overview of the application of the LW theorem to various electron acceleration-by-laser schemes is given by [10] and concludes that apart from limiting the interaction distance with mirrors that are not technologically possible at present, the only method by which an electron can be accelerated by a laser beam makes use of the  $(-e\mathbf{v} \times \mathbf{B})$  force, excluded from the LW theorem, the so-called Vacuum Beat Wave Accelerator (VBWA) or Ponderomotive Acceleration Scheme (PAS) [11].

The applicability of the LW theorem is extended to a focussed EM wave [12], so long as the particle interacting with the wave starts at  $-\infty$  and ends at  $+\infty$ .

However, particle acceleration schemes operating in regimes excluded from the LW theorem are widespread; for example an Inverse Free-Electron Laser Accelerator (IFELA) uses the static magnetic field of an undulator to couple the radiation field to the electron beam, for example [13], thus violating point 3. An Inverse Cerenkov Accelerator (ICA) violates point 4 with the presence of a background gas which reduces the phase velocity of the EM wave to match that of the electrons [14] allowing interaction to occur. Numerous Laser Wake Field Acceleration (LWFA) schemes extend this further by replacing the background gas with a plasma [15]. Finally, dielectric photonic structures can be used to deflect and focus a relativistic electron beam, for example to produce an ultra-compact undulator [16]. An overview of various laser accelerator schemes is in [17].

The area of interest for us is the combination of a finite (transverse) EM pulse (violating point 2) and a bounded interaction region (violating points 1 and 5). It was noted [18] that the small on-axis (of propagation) field component required in order to obey Maxwell's equations might provide a useful accelerating electric field for a high-power optical laser brought to a small focus. A mechanism of producing the small focal spot required for direct acceleration along with interaction with a particle beam was suggested in [19]. Such direct acceleration has been further developed using either a single [20, 21] or crossed Hermite-Gaussian (also called Bessel) beams [22].

Recent work at Brookhaven National Laboratory's Accelerator Test Facility (BNL-ATF) [23] has pursued the concept of a tightly focussed CO<sub>2</sub> laser, producing a 5 ps long pulse of 5 J, as a realistic prospect for direct acceleration. This relies on the observation that there is a channel at the laser focus where the phase velocity of the EM wave is less than the speed of light in a vacuum; thus if electrons travel along this channel they are captured and accelerated. This channel is at a small angle to the laser propagation direction. First experiments were undertaken in 2012 and from preliminary analysis of the data evidence of an interaction has been claimed; however results are not yet published. This is described as a proof-of-principle experiment and many times more laser power will be required to demonstrate significant acceleration. Indeed one proposal is that the experiment makes use of the laser available at the National Ignition Facility

(NIF); it is not clear how the limitations of mirror technology identified in [10] would be overcome.

## 1.3 Radially-polarized EM waves

### 1.3.1 Introduction

Throughout this thesis, the coordinate convention shown in Figure 1.2 is used, where (unless stated otherwise) any EM wave is propagating in the  $z$ -direction, the  $x$ -axis is both perpendicular to the  $z$ -axis and in the horizontal plane, while the  $y$ -axis is both perpendicular to the  $z$ -axis and in the vertical plane. The radial direction  $r$  is in the  $z=0$  plane at an angle  $\theta$  to the  $x$ -axis.

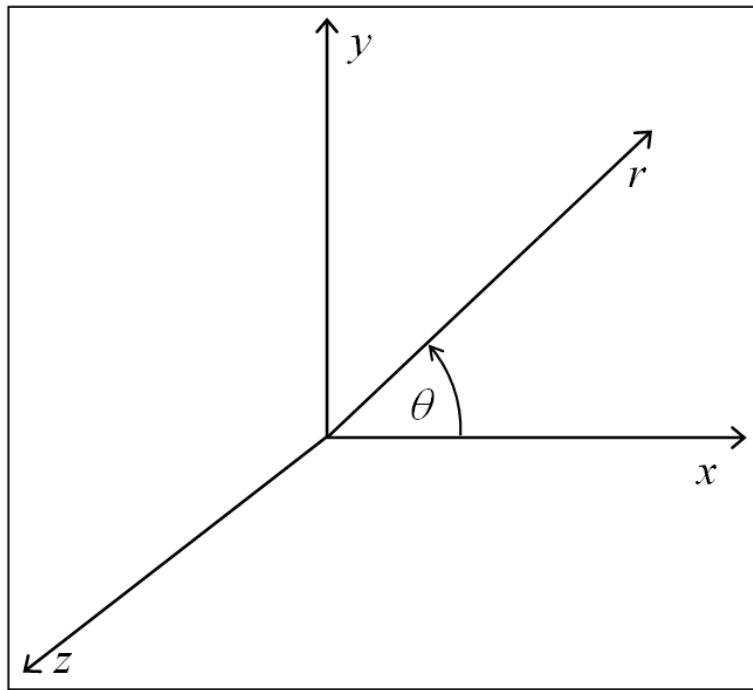


FIGURE 1.2: Coordinate convention

Unlike polarization states of EM radiation where the direction of the electric field is exclusively perpendicular to the propagation direction (albeit possibly rotating from the  $x$ -direction to the  $y$ -direction as it propagates [circular polarization] or changing magnitude as it does so [elliptical polarization]), radially-polarized EM radiation also has an  $E_z$  component. In order to satisfy Maxwell's equations, as the EM wave propagates the electric field vector must rotate to be perpendicular to the  $z$ -axis and then become longitudinal again but in the opposite direction. Furthermore, when viewed in the direction of propagation, the electric vector radiates out from the centre of the beam (except when fully longitudinal), hence the alternative term radially-polarized.

Thus a high-power, large diameter, radially-polarized beam has an  $E_z$  component that can have significant magnitude (for our purposes) when brought to a focus. Furthermore, at the point of maximum  $E_z$ , the radial field  $E_r$  is zero. Also, the only magnetic field is not only azimuthal, but also is zero on the propagation axis. Clearly if an electron beam can interact with such an EM wave for a restricted distance around the focus (determined by a combination of the Rayleigh length of the focus and the phase slippage between the EM wave and the electrons) then we have a mechanism for particle acceleration by a laser beam. A description of the properties of a radially-polarized Gaussian laser beam can be found in [24] and its proposed application as a GeV-scale electron accelerator in [25]. Radially-polarized laser beams can be generated interferometrically [26] or by using an axicon mirror; the results of simulations of the interaction of such a beam with an electron bunch are described in [27], which describes a purely longitudinal vector potential for a laser beam propagating in the  $z$ -direction. The vector potential:

$$\mathbf{A}(r, \theta, z, t) = \hat{\mathbf{z}} A_0 \Psi(r, z) \exp i(\omega t - kz) \quad (1.1)$$

satisfies both the wave equation  $\nabla^2 \mathbf{A} = \frac{1}{c^2} \frac{\partial^2 \mathbf{A}}{\partial t^2}$  and is related to the scalar potential:

$$\Phi = \frac{ic}{k} \nabla \cdot \mathbf{A}(r, \theta, z, t) = \frac{ic}{k} \frac{\partial A_z(\mathbf{x}, t)}{\partial z} \quad (1.2)$$

by the Lorentz gauge condition:

$$\nabla \cdot \mathbf{A} + \frac{1}{c^2} \frac{\partial \Phi}{\partial t} = 0. \quad (1.3)$$

The magnitude of the vector potential is given as (assumed to converge for small  $\epsilon$ ):

$$A_z = A_0(\Psi_0 + \epsilon^2 \Psi_2 + \epsilon^4 \Psi_4 + \dots) \exp i(\omega t - kz), \quad (1.4)$$

where  $\epsilon = \frac{2}{kw_0}$ ,  $w_0$  is the beam radius at its focus and  $k$  is the wavenumber. Furthermore, the Rayleigh range  $z_r = \frac{kw_0^2}{2}$ , so that  $\epsilon = \frac{w_0}{z_r}$ . Defining  $\rho = \frac{r}{kw_0}$  and  $\zeta = \frac{z}{z_r}$ , then the terms in the expansion for the vector potential are:

$$\Psi_0 = f \exp(-f\rho^2) \quad (1.5)$$

$$\Psi_2 = \left( \frac{f}{2} - \frac{\rho^4 f^3}{4} \right) \Psi_0 \quad (1.6)$$

$$\Psi_4 = \left( \frac{3f^2}{8} - \frac{3\rho^4 f^4}{16} - \frac{\rho^6 f^5}{8} + \frac{\rho^8 f^6}{32} \right) \Psi_0 \quad (1.7)$$

where  $f = \frac{i}{\zeta+i}$ . Finally, equation 9 in ref [27] can be expanded to give:

$$E_x = -\frac{ic}{k} \frac{\partial^2 A_z}{\partial x \partial z}, \quad (1.8)$$

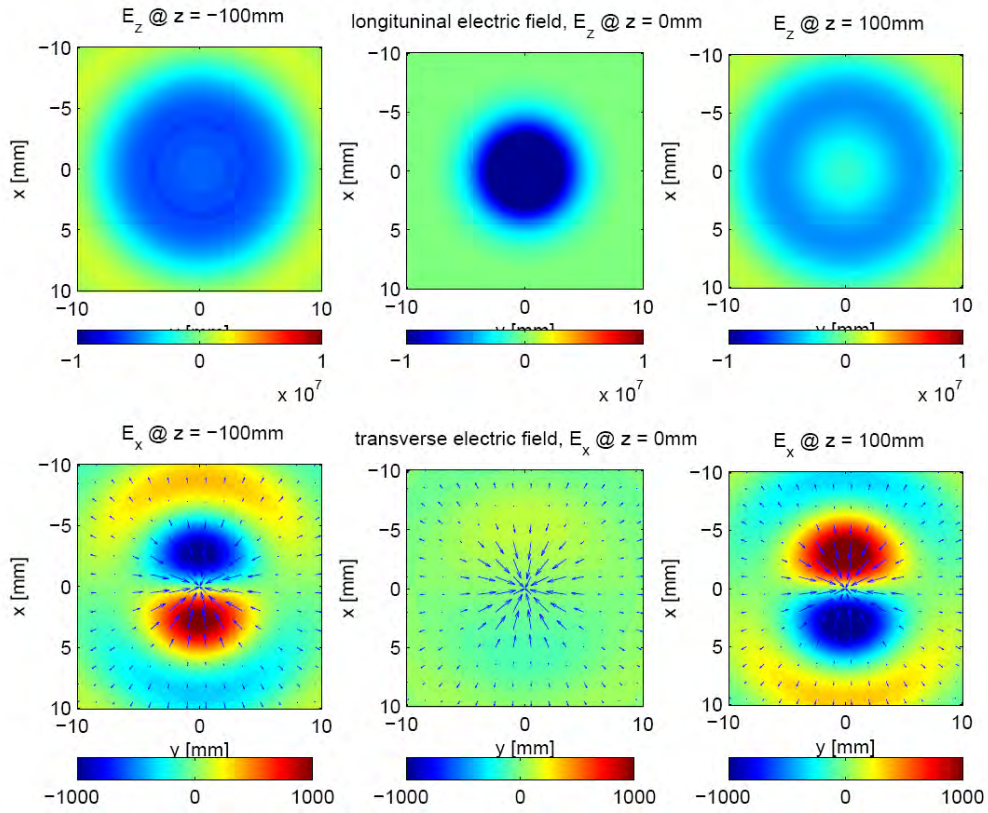


FIGURE 1.3: Transverse sections of the electric field of a radially-polarized EM wave, at  $z=0$  (the focus) and  $z = \pm 100$  mm

$$E_y = -\frac{ic}{k} \frac{\partial^2 A_z}{\partial y \partial z}, \quad (1.9)$$

$$E_z = -i\omega A_z - \frac{ic}{k} \frac{\partial^2 A_z}{\partial z^2}. \quad (1.10)$$

Figure 1.3 (SPJ) shows the electric field at transverse sections (at  $z=0$  mm and  $z = \pm 100$  mm) calculated with the method in [24]; for a wavelength  $\lambda=1$  mm forming a beam radius at the focus ( $z=0$  mm) of  $w_0=4$  mm. Figure 1.4 (SPJ) shows the situation at a later time, the interval being equivalent to one half-cycle of the radiation.

Figure 1.5 (SPJ) shows the electric field in longitudinal sections at these three positions. Note the absence of any transverse electric field on axis.

### 1.3.2 Radially-polarized terahertz pulses

One of the topics of this thesis is the generation of radially-polarized terahertz pulses which can then be used to induce energy modulation in an electron bunch. So rather than taking a high-power optical laser and attempting directly to accelerate particles with it, we convert the optical laser beam, which is conventionally plane-polarized, into a short, radially-polarized terahertz pulse. The advantages of this approach include the relative ease with which the terahertz beam can be manipulated (simple metal mirrors

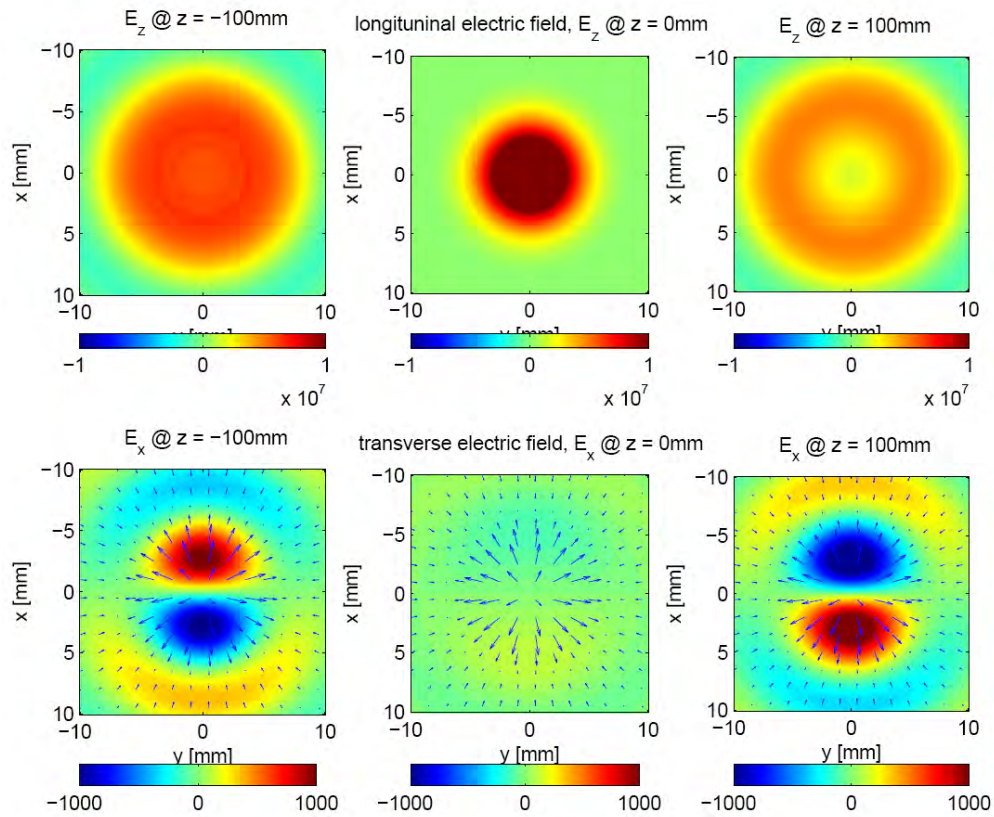
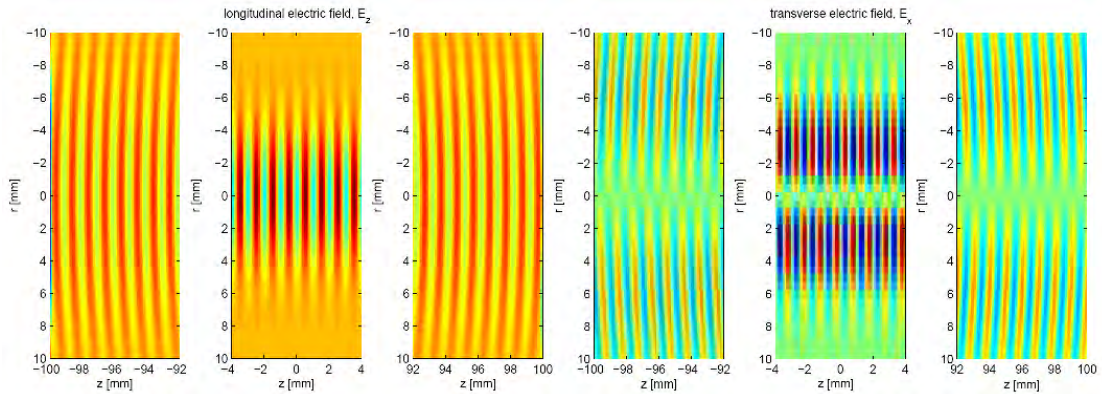


FIGURE 1.4: Repeat of figure 1.3 but one half-cycle of the radiation later

FIGURE 1.5: Longitudinal sections of the electric field of a radially polarized EM wave, at  $z=0$  (the focus) and approximately  $z = \pm 100$  mm

can be used; mirrors for very high-power optical-wavelength radiation are technologically difficult) and the similarity of the scale of the terahertz wavelength with typical electron bunch lengths in accelerators in the energy range for which this experiment was conceived. The larger the fraction of the electron bunch that sees the longitudinal terahertz electric field, the easier the effect will be to detect. A further advantageous feature of a radially-polarized beam is that it is possible to bring it to a smaller focus than a linearly-polarized one, for example [28] [29].

### 1.3.3 Terahertz generation from antennae

In order to produce pulses of terahertz radiation the experiment described in this thesis uses a simple antenna, constructed from two electrodes attached to a semiconductor wafer. The electrodes can have a simple linear geometry, or as described more fully later in this section, rotational symmetry, depending on the desired properties of the terahertz radiation field. A pulse of terahertz radiation is produced by triggering the electrical breakdown of a high voltage held between the two electrodes attached to the wafer. One of the first applications of the short current pulse produced in a biased semiconductor by laser-stimulated breakdown was in a one-dimensional device, which acts as a fast closing switch [30]. In two-dimensions this technique was initially developed on small scale devices (though the dimensions of the device  $\gg$  mean radiated wavelength) [31], but it was soon realized that it could be scaled up to much larger devices [32, 33]. When pumped with a femtosecond-scale large-diameter high peak-power infrared laser pulse such devices will produce very short and intense terahertz pulses. A standard 75 mm or 100 mm diameter gallium arsenide (GaAs) or indium phosphide (InP) wafer (standard semiconductor industry substrates) does not conduct when a grounded and high-voltage (either DC or pulsed) electrode are attached to the surface. However, if the semiconductor is made conducting by illuminating it with a very short infrared laser pulse, so that electrons are promoted into the conduction band, a large photocurrent flows briefly. This produces broadband radiation in both directions from the surface (a forward flux and a backward flux). Due to the interaction of the forward flux (which must pass through the wafer) with the excited carriers in the GaAs, unlike the backward flux, there are differences in the temporal profile of the forward and backward radiation [34]. Also, as the EM pulse leaves the wafer, the longer wavelengths will expand transversely more rapidly than the shorter wavelengths, due to diffraction. On the axis of radiation the minimum pulse duration is seen; further off-axis the pulse length will increase due to the timing differences between the source components of the wave.

Another interesting and important feature of the radiation field produced is that to first order, it preserves the angle of the incoming pump beam relative to the semiconductor surface. The implication of this is that if the pump beam is diverging or converging (i.e. focussing) then the radiation field will do the same. This is most easily understood first of all by considering a plane laser wavefront (i.e. neither diverging nor converging) incident at an angle  $\theta$  to the normal, as shown in Figure 1.6. Because the spatial and temporal distribution of the photocurrent is determined by the arrival of the laser wavefront, it can be seen from simple geometric argument that the propagation axis of backward-going radiation will appear to be along that of simple specular reflection, as both the laser and the terahertz pulses are passing through the same medium. This of course ignores diffraction effects, which for the much longer wavelength terahertz (1 THz corresponds to a wavelength of 0.3 mm, so two-to-three orders of magnitude longer than the laser) will be much more significant. Similarly for an antenna constructed from

a thin semiconductor wafer, the forward-going radiation will appear to continue along the same path as the pump laser beam.

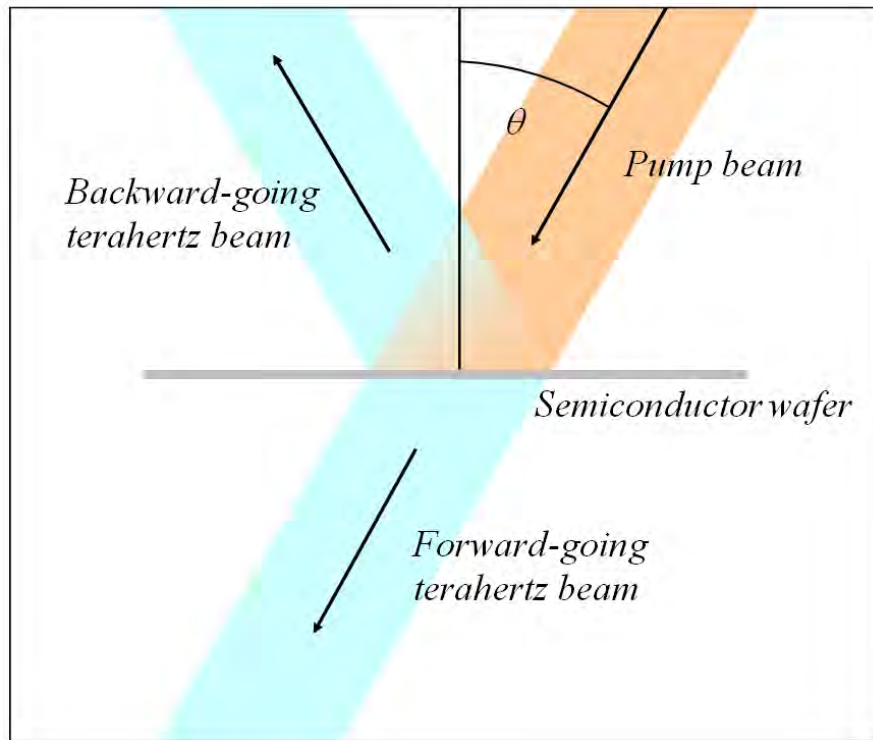


FIGURE 1.6: Generation of forward and backward terahertz pulses

A small fraction of the forward-going radiation will be reflected from the wafer-air (vacuum) interface on the back side leading to multiple internal reflections emerging from both faces. For a wafer of the order of 1 mm thick, these internal reflections will emerge on a picosecond timescale after the primary pulse. As our pulses are of femtosecond scale, these will appear long after the primary pulse and can be ignored.

Figure 1.7 shows the same arrangement but the pump laser beam is perpendicular to the wafer surface, and the laser has a curved wavefront, so that it is coming to a focus. For clarity the backwards-going radiation is omitted. Because of the curved wavefront of the pump laser, the edges of the beam fall on the wafer first, so that the radiation is produced from here first. Again ignoring diffraction, at a point beyond the wafer where the pump laser would have formed a focus, the radiation from different parts of the wafer will arrive at the same time (having to travel further but also starting earlier) and thus superimpose to give the maximum amplitude at the nominal laser focus.

### 1.3.4 Radially-polarized terahertz generation from antennae

From the simple geometry of the antennae described in the previous section, with two linear electrodes (one earthed and one at high voltage) attached to a large, flat semiconductor wafer, the terahertz radiation is clearly going to be plane polarized. However,

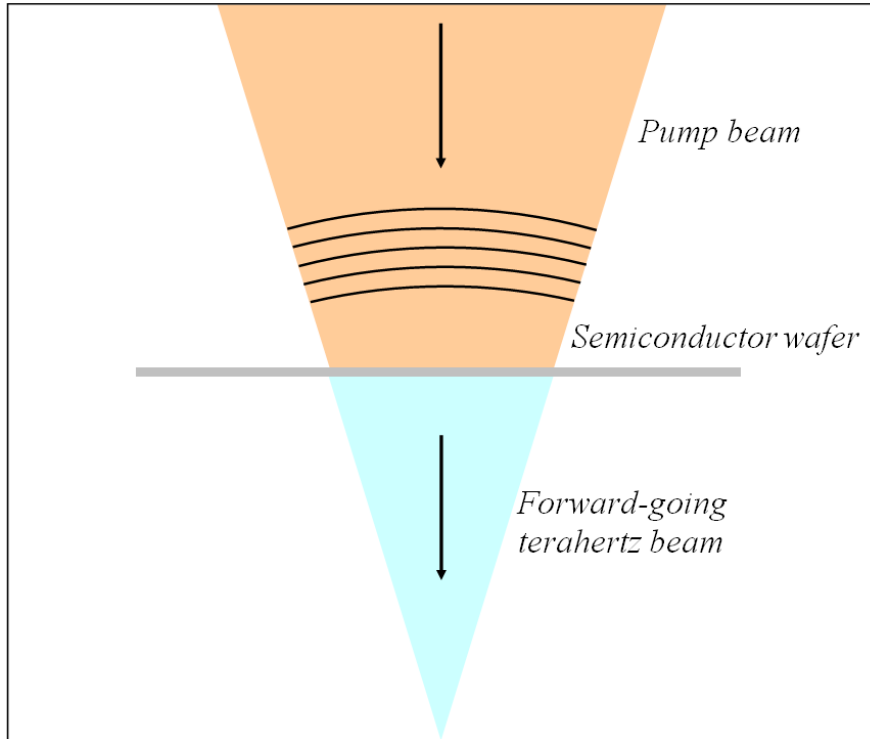


FIGURE 1.7: Radiation field generated by a converging pump laser

experiments aimed at improving the transmission of broadband terahertz pulses in coaxial waveguides were limited by the plane-polarized state of the radiation being poorly suited to this geometry. To overcome this, a rotationally symmetric antenna design was proposed [35] and the radiation field produced modelled both analytically and by the Finite Element Method (FEM) [36]. The rotationally-symmetric design described in these references has a  $5\ \mu\text{m}$  diameter centre electrode and only  $100\ \mu\text{m}$  gap between the centre and outer electrodes; in addition the rotational symmetry is broken by the method used to make electrical contact with the centre electrode. In fact quite complex electrode profiles have been experimented with in order to manipulate the polarization of the resultant terahertz pulse [37]. High repetition rate production of terahertz pulses has also been demonstrated [38], which have the interesting feature that the pulse energy increases significantly at the high repetition rate.

For our experiment we have developed a combination of the large photoconductive (semiconductor) wafer-based antenna described earlier but with rotationally-symmetric geometry. Figure 1.8 is a photograph of the antenna assembly, prior to placing it on the outer electrode. This example is a  $75\ \text{mm}$  diameter GaAs wafer with simple spherical cross-section electrodes.



FIGURE 1.8: Nearly-complete antenna assembly, showing the outer electrode on the right and the wafer with the centre electrode already attached (along with the electrical connection to the outer electrode) on the left. These are supported by two halves of the non-conducting holder that provide mechanical support.

### 1.3.5 Modelling the terahertz radiation field from rotationally-symmetric antennae (DN)

A number of different methods of terahertz generation have been given a unified theoretical framework in the frequency domain [39]. In order to model correctly the radiation produced from first principles it is first necessary to calculate the spatial and temporal distribution of the photocurrent on the wafer [40, 41] before calculating the radiation field. To do this it is necessary to make some assumptions about the properties of the GaAs itself, some of which are not well known as they vary from one batch of material to the next; for example the scattering rate and the trapping time. However, it was subsequently found that by judicious choice of these values, good agreement between the simulation and measurement could be achieved. After modelling the photocurrent, the next step is to calculate the electric field thus produced and then finally the propagation of the terahertz pulses to the observer's location [42–44]. In our case this is the focal point of the pump laser which is where the interaction with the electron bunches will take place. Table 1.1 lists the laser and wafer parameters used in the simulation.

The wafer is placed within the  $x$ - $y$  plane at  $z = 0$  in the coordinate system defined earlier and centred on the origin. The reference time,  $t = 0$  is defined to be when the centre of the laser pulse passes through  $(0,0,0)$ . The laser is perpendicular to the wafer and is incident from the negative  $z$ -direction. Only the forward-going radiation field (in the positive  $z$ -direction) is modelled. The converging beam (equivalent to a concave

Laser pulse length	$\sigma_t$	16.9	fs
Laser transverse radius	$r_l$	0.0377	m
Centre electrode radius	$r_1$	0.0075	m
Wafer radius	$r_2$	0.0377	m
Outer electrode radius	$r_3$	0.0025	m
Focus position	$f$	2	m
Wavefront curvature	$t' = t - (\sqrt{(f^2 + r^2)} - f)/c$		
Laser pulse energy	$E_{LP}$	1	mJ
Laser wavelength	$\lambda$	800	nm
Bias voltage	$V_b$	30	kV
Electric field	$E_b$	from Opera model†	
Reflectivity coefficient	$R$	0.5	
Scattering rate	$\tau$	$\approx 10^{12}$	$s^{-1}$
Effective electron mass	$m^*$	0.063	$m_e$
Trapping time	$T$	variable	s
Electron charge	$e$	$1.6 \times 10^{-19}$	C

TABLE 1.1: Parameters used in the simulation of radiation emission from the antenna (†the radial dependence of the electric field is a function of the geometry of the antenna; an example of this can be seen in figure 2.13 in Chapter 2)

laser wavefront) is included in the model by introducing a radially-dependent time delay to the laser pulse.

The laser flux density ( $\text{Wm}^{-2}\text{s}^{-1}$ ) through any area element of the wafer at time  $t$  (assuming a Gaussian time profile) is:

$$I = I_0 \exp\left(-\frac{(t_0 - t)^2}{\sigma_t^2}\right), \quad (1.11)$$

and if the laser beam completely fills the wafer (i.e.  $r_l = r_2$ ) and has a true top-hat profile then:

$$I_0 = \frac{E_{LP}}{\pi r_2^2}. \quad (1.12)$$

Although the following calculation considers only electrons, the contribution of holes is calculated in an identical fashion, (but with the correct parameters for holes rather than electrons). The two results are then simply summed. The surface current density at radius  $r$  and time  $t$  produced by the incident laser is:

$$\mathbf{J}_s(r, t, t_0) = n_e(r, t, t_0) \mathbf{v}_d(r, t, t_0), \quad (1.13)$$

where the surface charge density created at  $t_0$  is given by

$$n_e(r, t, t_0) = e(1 - R) \frac{I(r, t, t_0)}{h\nu} \exp\left(-\frac{t}{T}\right). \quad (1.14)$$

Applying the Drude model of conduction to the wafer (so that the current density is proportional to the field to first order) the drift velocity is given by:

$$\mathbf{v}_d(r, t, t_0) = \frac{eE_b(r)}{\tau m^*} \left(1 - \exp\left(-\frac{t - t_0}{\tau}\right)\right) \quad (1.15)$$

Finally integrating with respect to  $t_0$ ,

$$J_s(r, t) = \int_{-\infty}^t J_s(r, t, t_0) dt_0. \quad (1.16)$$

The next step is to calculate the radiation field from the moving charges in an area element  $dA$  using the Liénard-Wiechert potentials method [45]. For our case, the electric field radiated from an area element  $dA$  and observed at  $(\mathbf{x}, t)$  is given by:

$$\frac{d\mathbf{E}(\mathbf{x}, t)}{dA} = \frac{n_e}{4\pi\epsilon_0 c} \left( \frac{c(\mathbf{n} - \boldsymbol{\beta})}{\gamma^2 |\mathbf{R}|^2 (1 - \boldsymbol{\beta} \cdot \mathbf{n})^3} + \frac{\mathbf{n} \times [(\mathbf{n} - \boldsymbol{\beta}) \times \dot{\boldsymbol{\beta}}]}{|\mathbf{R}| (1 - \boldsymbol{\beta} \cdot \mathbf{n})^3} \right)_{ret} \quad (1.17)$$

where  $\mathbf{R}$  is the vector from the source point to the observation point,  $\mathbf{n}$  is the unit vector along  $\mathbf{R}$ ,  $\boldsymbol{\beta}$  is  $\mathbf{v}/c$  of the photocurrent electrons and the suffix  $ret$  indicates that this must be evaluated taking into account the time difference between the source and observation points.  $\boldsymbol{\beta}$  and  $\dot{\boldsymbol{\beta}}$  can be derived from our expression for the surface current density  $\mathbf{J}_s$  (equation 1.13 and 1.16). The final step is to numerically integrate equation 1.17 over the whole of the wafer surface. Figure 1.9 (DN) shows (a) the longitudinal, (b) the radial electric field strength of the terahertz generated by the electrical breakdown of the wafer, calculated using the parameter values given in Table 1.1.

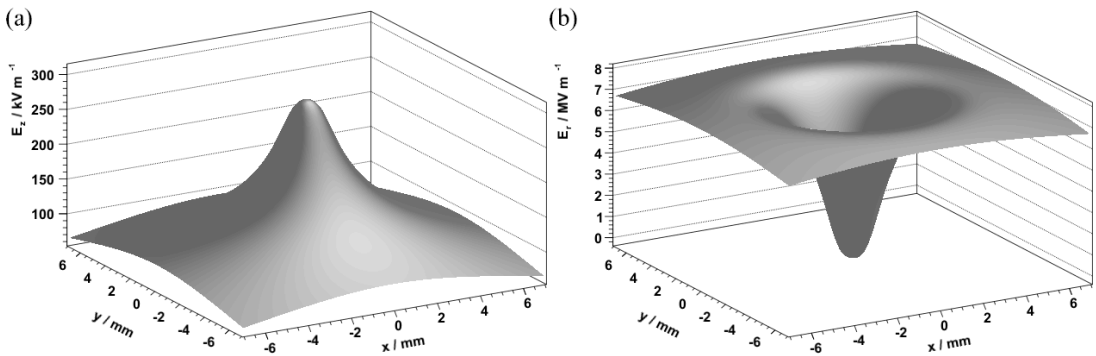


FIGURE 1.9: Terahertz electric field generated by the electrical breakdown of the wafer, in (a) the longitudinal, and (b) the radial directions

## 1.4 Detection and measurement of terahertz radiation

### 1.4.1 Introduction

In order to characterize the improved antenna designs that are a major part of this thesis, as well as providing data for modelling the strength of the interaction of the

terahertz radiation with the electron beam, it is necessary to measure the strength of the electric field in the terahertz pulses generated by the antenna. To do this we make use of the Electro-Optic (EO) effect [46, 47]. This is a phenomenon exhibited by certain materials (we use zinc telluride, ZnTe) in which an electric field (in our case that from the terahertz pulse) causes the material to become birefringent, with the degree of birefringence determined by the electric field strength.

In a birefringent material, the refractive index depends on the polarization of the wave. If the material is cut in a certain way (birefringent materials are typically crystals whose lattice structure has certain symmetry, although some plastics are also birefringent when under stress) then they can be used to modify the polarization state of the light that they are transmitting. This is because if the polarization state of the light is decomposed into a component along and a component perpendicular to the optical axis (a particular direction in the material), the effect of birefringence is to introduce a phase shift between these components. This is utilized in quarter-wave plates for example, which are used to change linearly polarized light to circular and vice versa by introducing a quarter-wavelength phase shift between the two components. Clearly, this will only happen for one combination of wavelength, crystal thickness and incident wave polarization.

In general, if linearly polarized light of arbitrary single wavelength passes through a birefringent crystal of arbitrary length, then the light exiting the crystal can have its polarization state modified to anything from elliptical to circular to linear again (but orthogonal to the incoming plane of polarization).

### 1.4.2 Terahertz generation and measurement apparatus

Because these measurements were undertaken in two different locations (the ALICE Diagnostics Room and within the ALICE accelerator hall) the description here is for a generic experimental set up; some of the details will be different in the two locations and these will be described more fully at the appropriate places in this thesis (Chapters 3 and 5). Figure 1.10 shows a schematic of the experimental arrangement. The 40 fs, 800 nm Ti:S laser pulses, available at up to 1 kHz repetition rate, are split by a 90/10% beamsplitter; the higher-power beam used to generate the terahertz (the pump beam) is first expanded and then focussed onto the ZnTe crystal (after temporarily adding several orders of magnitude attenuation) via reflection off the beam combiner. Once set up as described, the antenna assembly is then placed at an appropriate location in the converging pump beam to convert the optical beam into a converging terahertz beam.

Meanwhile the lower-power beam (the probe beam) bypasses the antenna assembly, passes through the beam combiner and the ZnTe crystal and onto the detection system. The simultaneous presence of terahertz radiation produces birefringence in the ZnTe crystal via the EO effect which then modifies the polarization state of the probe beam, allowing the presence of terahertz to be detected. The crystal can be cut so that it is only sensitive to an electric field in a particular direction (either along the direction of propagation of the terahertz or perpendicular to it). The linearly-polarized probe beam

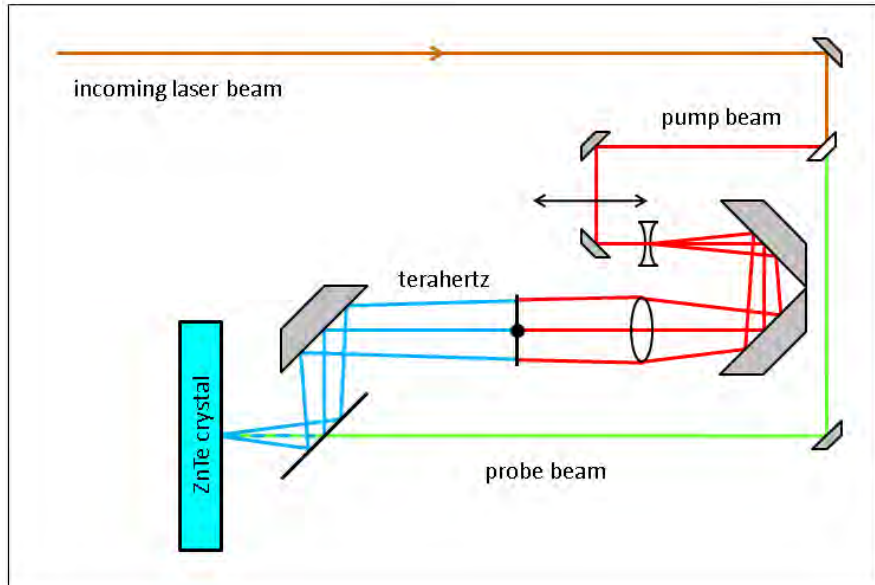


FIGURE 1.10: Schematic of the terahertz generation and detection apparatus

passing through the crystal then becomes elliptically polarized; the degree of ellipticity and the angle of the major axis of the ellipse is determined by the electric field strength of the simultaneously incident terahertz pulse. The modification to the polarization state of the probe beam thus provides a mechanism to detect the simultaneous presence of terahertz. In order to ensure that the time of arrival of the probe pulses and terahertz radiation are coincident it is necessary to:

- Ensure the optical pathlengths of both the pump and the probe beams, from the beamsplitter to the beam combiner, are the same to within a few millimeters (in  $\approx 1$  m);
- Be able to adjust the optical pathlength of the pump beam so that the timing of the arrival of terahertz pulse can be scanned from before, to during, then after, the probe pulse.

To achieve the first of these requires careful design and assembly of the optical layout; the second is achieved by using an optical delay line in the probe beam path. This consists of two mirrors mounted on a computer-controlled translation stage which can increase or decrease the optical pathlength in steps. The minimum step size is  $20 \mu\text{m}$ , which corresponds to a minimum time step of  $\approx 70$  femtoseconds.

Two alternative detection systems can be utilized:

- A crossed polarizer and camera to image the whole of the ZnTe crystal, providing information about the spatial extent of the terahertz pulse;
- A polarizing beamsplitter, two photodiodes and a lock-in amplifier, to measure the sum and difference signals from the diodes, providing more sensitivity but no spatial information.

In both of these arrangements the ZnTe crystal is also followed by a quarter-wave plate which has a different purpose in each case.

In the first arrangement, the ZnTe crystal is followed by a crossed polarizer (i.e. one perpendicular to the polarization plane of the probe beam), so that without any terahertz present almost no light from the probe beam reaches the camera. The quarter-wave plate between the ZnTe crystal and the crossed polarizer is required because the ZnTe crystal is not perfect - it may have a small amount of residual birefringence without any electric field present. This can be counteracted by judicious adjustment of this quarter-wave plate, leading to near total extinction of the probe beam at the camera. The simultaneous presence of the terahertz pulse's electric field is detected because the extinction of the probe beam is disrupted, and this is recorded by the camera. This arrangement is shown in figure 1.11. Furthermore, the magnitude of the EO effect and therefore the terahertz electric field strength can be measured by rotation of the quarter-wave plate (see next section).

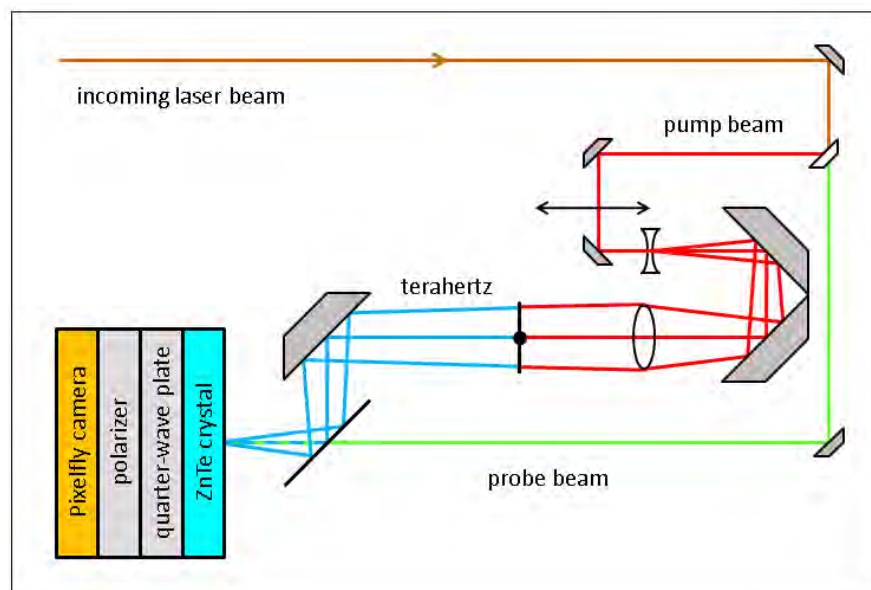


FIGURE 1.11: Schematic of the terahertz generation with camera detection

The second arrangement offers more sensitivity, but at the cost of sampling only one position on the ZnTe crystal. This is shown in figure 1.12. In this case, the quarter-wave plate following the ZnTe crystal is rotated in order to get equal intensity from two beams produced from a subsequent polarizing beamsplitter, when there is no terahertz electric field present. These beams are then detected by two photodiodes; one for each of the two orthogonal linear polarizations, which have been spatially separated by the polarizing beamsplitter. The birefringence subsequently induced by the terahertz pulse changes the relative intensity of the two diode signals. Using a lock-in amplifier to measure the sum and difference signals from the diodes, and subtracting a background signal (from when there is no terahertz present) makes this a very sensitive detector.

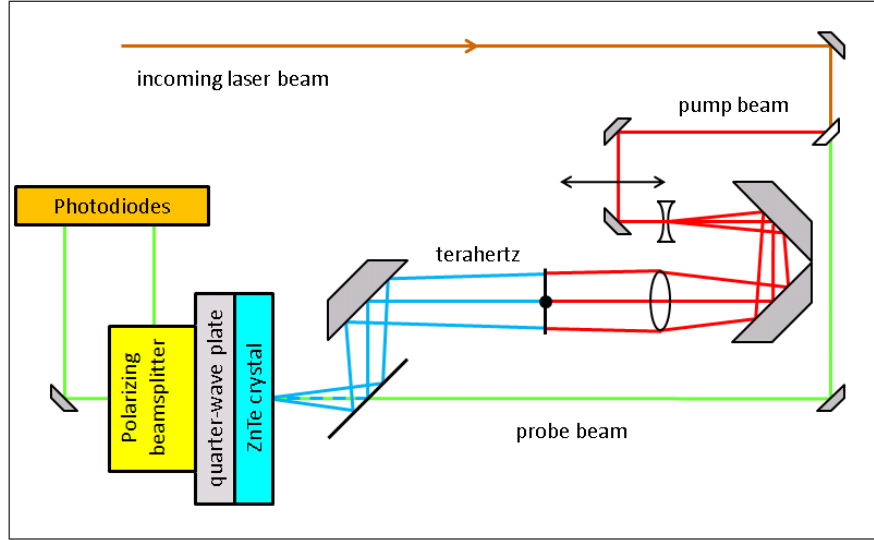


FIGURE 1.12: Schematic of the terahertz generation with photodiode detection

## 1.5 Examples of experimental results

Figure 1.13 shows a series of images recorded by the Pixelfly camera as the optical delay line translation stage position moves the arrival time of the terahertz pulse relative to the probe pulse; passing through the point of maximum intensity. The time step between images is 0.13 picoseconds. Each individual image can be compared to the simulation results of figure 1.17; the combination of a linearly polarized probe beam, a radially polarized terahertz pulse and a detection crystal cut and orientated to be sensitive to transverse electric field leads to a distinctive twin-lobe pattern. Small alignment errors lead to small timing differences in the horizontal plane which cause the left and right lobes to appear at slightly different times.

Figure 1.14 shows a typical result from a photodiode/lock-in amplifier measurement. The  $x$ -axis is the relative timing of the probe laser beam and the terahertz pulse while the  $y$ -axis is the lock-in amplifier sum voltage. The largest positive peak corresponds to the probe beam and terahertz pulse arriving at the detection crystal at the same time.

### 1.5.1 Calibration of the terahertz electric field (DL)

To analyze the effect on the probe beam of the combination of optical elements that make up the detection arrangement described above, it is best to use Jones calculus, where the polarization state of the light is represented by a vector and optical elements by matrices. A plane-polarized EM wave is decomposed into its components in the  $x$  and  $y$ -directions (the coordinate convention is the same as before; the beam is propagating in the  $z$ -direction) and represented in the following way:

$$\mathbf{E} = \begin{pmatrix} E_x \\ E_y \end{pmatrix} \exp i(\omega t - kz)$$

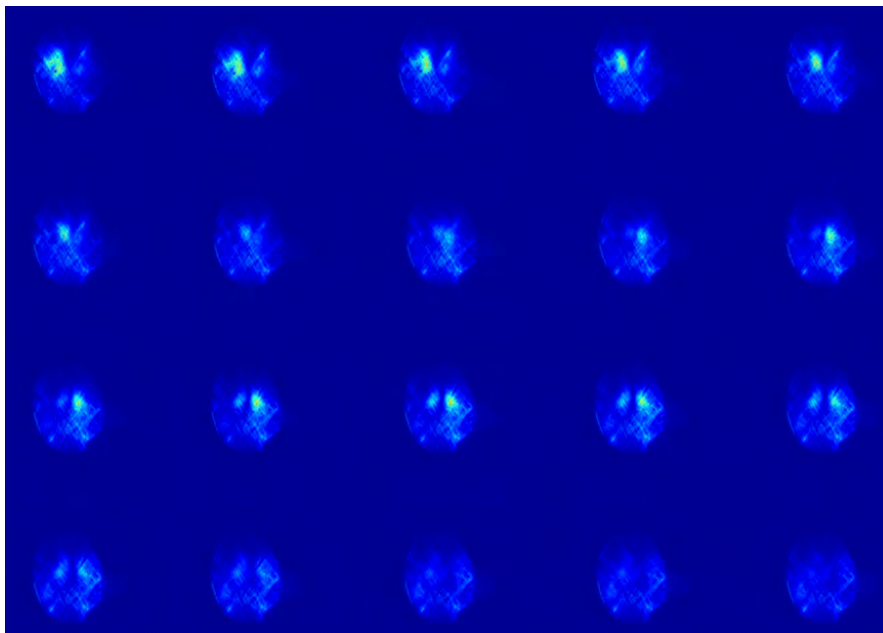


FIGURE 1.13: Images of the ZnTe crystal at 0.13 ps time steps of the terahertz pulse relative to the probe laser pulse

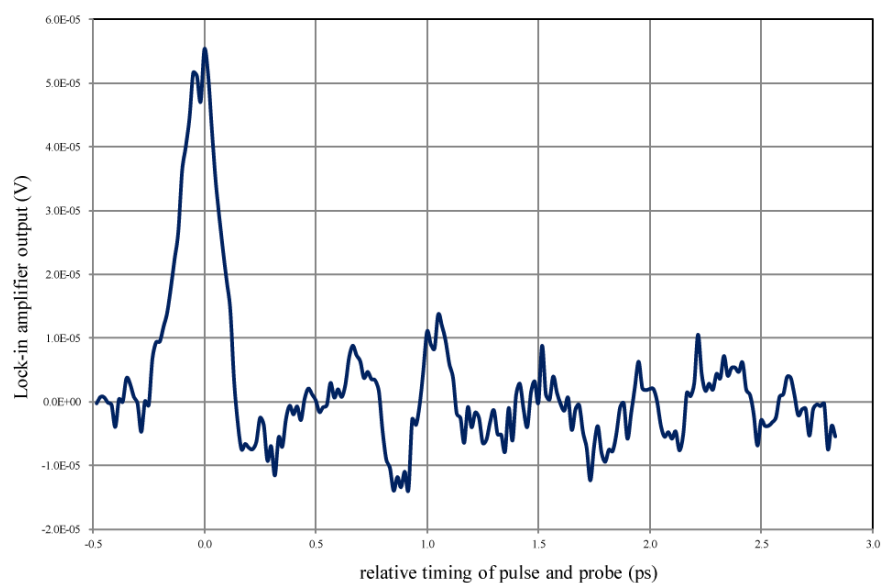


FIGURE 1.14: Photodiode/lock-in amplifier sum voltage recorded as a function of the time difference between the terahertz pulse and the probe laser beam, for a 0.5 mm ZnTe crystal and with the antenna operating at 50 kV

To simplify things further it is common to normalize the Jones vector so that the sum of the squares of the elements is one and discard the phase information (which is constant for our plane-polarized wave). The Jones vector for our horizontally-polarized probe beam thus becomes:

$$\begin{pmatrix} 1 \\ 0 \end{pmatrix}$$

The Jones matrix for a linear-polarizer that transmits in the vertical plane is:

$$\begin{pmatrix} 0 & 0 \\ 0 & 1 \end{pmatrix}$$

The Jones matrix for a quarter-wave plate is:

$$\begin{pmatrix} \exp(-\frac{i\pi}{4}) & 0 \\ 0 & \exp(\frac{i\pi}{4}) \end{pmatrix}$$

The Jones matrix for an element exhibiting the EO effect is:

$$\begin{pmatrix} \exp(-i\Phi_{EO}) & 0 \\ 0 & \exp(i\Phi_{EO}) \end{pmatrix},$$

where the phase shift due to the EO effect is:

$$\Phi_{EO} = \chi^{(2)} L_z E_{THz} n^3 \frac{\pi}{\lambda}. \quad (1.18)$$

$L_z$  is the length of the element exhibiting the EO effect,  $n$  is its refractive index,  $E_{THz}$  is the terahertz electric field strength,  $\lambda$  is the wavelength of the light. The tensor element  $\chi^{(2)}$  is the EO coupling coefficient, sometimes referred to as  $r_{41}$ .

It is also necessary to deal with rotation of optical elements represented by these matrices around the  $z$ -axis; the Jones matrix for the rotated element  $M(\theta)$  is constructed from that of the nominal matrix  $M$  by the following transformation:

$$M(\theta) = R(-\theta) M R(\theta),$$

where

$$R(\theta) = \begin{pmatrix} \cos \theta & \sin \theta \\ -\sin \theta & \cos \theta \end{pmatrix}.$$

In order to calculate the Jones vector of the probe beam after it has passed through the ZnTe crystal (in the presence of terahertz radiation), the quarter-wave plate (which can be rotated through an angle  $\theta$  around the  $z$ -axis) and the crossed-linear polarizer, the initial Jones vector is multiplied by appropriate Jones matrices to represent the subsequent elements:

$$\begin{pmatrix} E_x \\ E_y \end{pmatrix} = \begin{pmatrix} 0 & 0 \\ 0 & 1 \end{pmatrix} \begin{pmatrix} \cos(-\theta) & \sin(-\theta) \\ -\sin(-\theta) & \cos(-\theta) \end{pmatrix} \begin{pmatrix} \exp(-\frac{i\pi}{4}) & 0 \\ 0 & \exp(\frac{i\pi}{4}) \end{pmatrix} \begin{pmatrix} \cos \theta & \sin \theta \\ -\sin \theta & \cos \theta \end{pmatrix} \begin{pmatrix} \exp(-i\Phi_{EO}) & 0 \\ 0 & \exp(i\Phi_{EO}) \end{pmatrix} \begin{pmatrix} 1 \\ 0 \end{pmatrix}$$

The intensity of the signal recorded by the detector is proportional to the sum of the

square of the electric field amplitude in each plane:

$$I = E_x^2 + E_y^2. \quad (1.19)$$

When plotted against quarter-waveplate angle  $\theta$ , the intensity  $I$  has a minimum, the position of which is a function of the phase shift due to the EO effect. This is shown in figure 1.15 (DL), for a number of different terahertz electric field strengths. Figure 1.16 (DL) shows the relationship between the field strength and the angle of the quarter-waveplate at the minima. Thus by making measurements of the transmitted intensity at a range of quarter-waveplate angles and then fitting a curve to the data points, it is possible to determine the strength of the terahertz electric field.

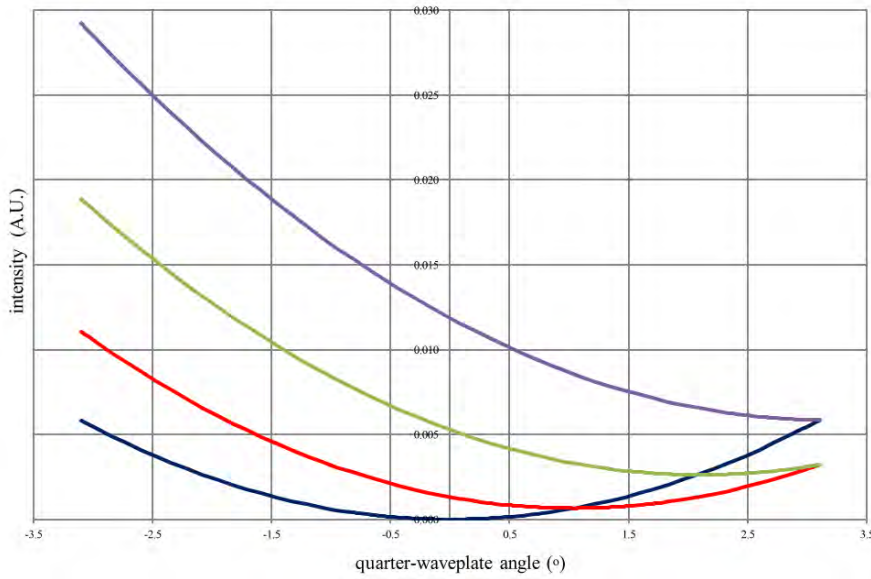


FIGURE 1.15: Calculated probe beam intensity transmitted by the ZnTe crystal and crossed-polarizer, as a function of quarter-wave plate angle, in the presence of a terahertz electric field of 0 V/m (blue);  $2 \times 10^5$  V/m (red);  $4 \times 10^5$  V/m (green);  $6 \times 10^5$  V/m (purple)

### 1.5.2 Calculation of the transmission through a ZnTe crystal and crossed polarizer in the presence of terahertz radiation (SPJ)

Similarly, it is possible to calculate the intensity at every point on the crystal, assuming that the whole of a ZnTe crystal (in  $\langle 110 \rangle$  orientation) is illuminated with a horizontally-polarized Ti:S laser beam with a Gaussian transverse profile. The ZnTe crystal is assumed to be perfect (i.e. it has no residual birefringence) and the crossed polarizer perfectly extinguishes the probe beam when there is no terahertz present. It is also assumed that there are no mis-alignments present which lead to a difference in the time of arrival of the terahertz and laser pulses across the crystal. Figure 1.17 (SPJ) shows the calculated intensity of the probe beam after passing through a ZnTe crystal which is simultaneously illuminated by a radially-polarized terahertz pulse, with the

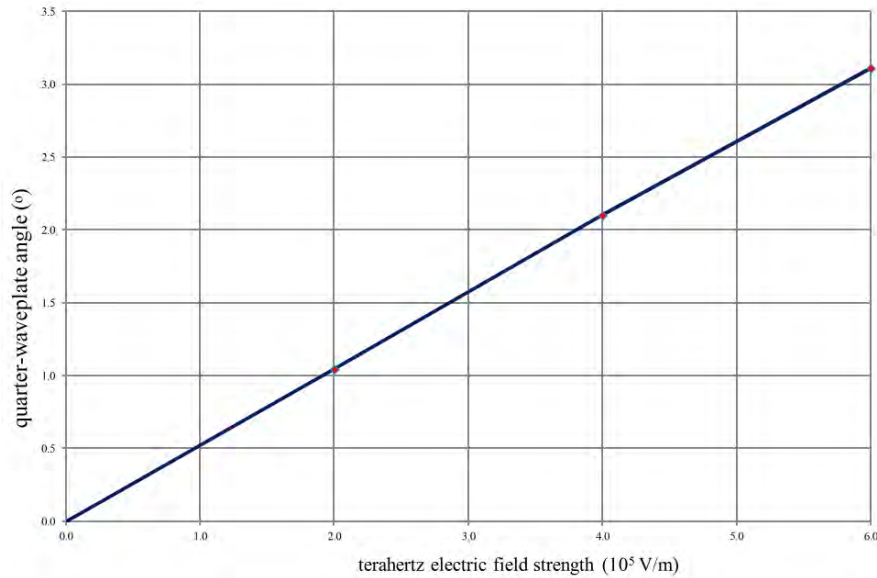


FIGURE 1.16: Quarter-wave plate angle at the minima of the plots in figure 1.15 as a function of terahertz electric field strength

combination of other optical elements as described in the previous section. As this is the light that emerges from the crossed-polarizer, it is therefore the image that should be seen on a camera looking at the crystal.

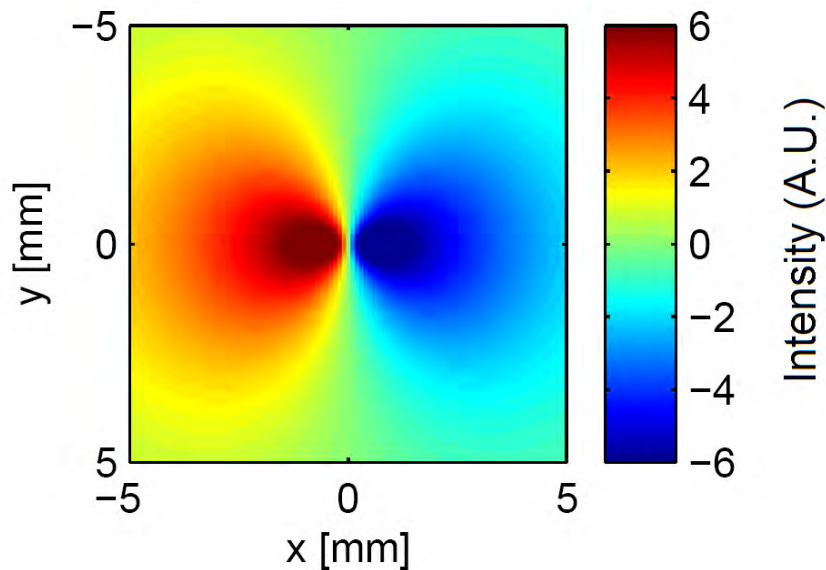


FIGURE 1.17: The calculated intensity of the probe beam after passing through a ZnTe crystal which is simultaneously illuminated by a radially-polarized terahertz pulse, with both the terahertz pulse and the probe beam filling the crystal

Figure 1.18 (SPJ) shows the calculated intensity of the probe beam at a single point after passing through a ZnTe crystal, as a function of its timing relative to a radially-polarized terahertz pulse also passing through the crystal.

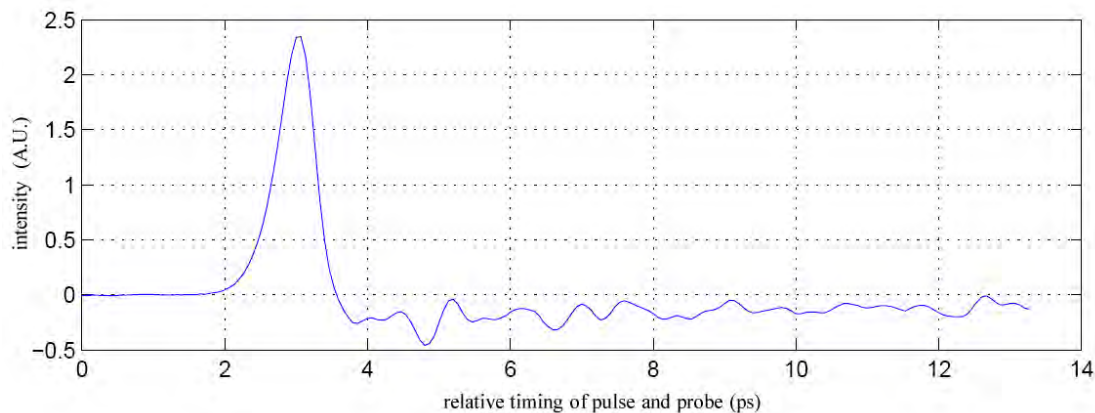


FIGURE 1.18: The calculated intensity of the probe beam at a single point after passing through a ZnTe crystal, as a function of its timing relative to a radially-polarized terahertz pulse also passing through the crystal

Both these figures represent the ideal case. In addition to the effects described below that will serve to disrupt this ideal, if the alignment of the two beams is not perfect there will also be timing differences in the horizontal plane, which will lead to the maxima seen each side of the centre not occurring at precisely the same time (i.e. the terahertz and laser pulses will not be present simultaneously across the whole crystal).

### 1.5.3 Sources of departure from the ideal case

There are a number of effects that are not included in this model of terahertz generation from an antenna and its subsequent detection and characterization via the EO effect. Looking at figure 1.14 again, apart from the main terahertz pulse with its rapid rise and fall, there follow a number of much smaller oscillations. These are primarily due to atmospheric absorption at particular wavelengths [48]; because the terahertz pulse is significantly chirped (so all frequencies present are not in phase) there are some spectral components that arrive after the main pulse. Other factors that contribute to an imperfect measurement include:

- The 800 nm probe beam and terahertz pulses will have different refractive indices in the ZnTe crystal. This will lead to some phase slippage in the crystal and the apparent broadening and reduction in amplitude of the terahertz pulse;
- Dispersion in ZnTe crystal, particularly at terahertz frequencies;
- Reflections off the surface of the ZnTe crystal producing interference effects with the incident beam.

## 1.6 Modelling the interaction of the terahertz radiation with the electron beam (AW)

The third of the experimental studies reported in this thesis is the attempt to use the radially-polarized terahertz radiation to induce an energy modulation in the electron bunches in the ALICE accelerator. The intention was to observe the energy modulation as a transverse beam blow-up on additional diagnostics installed at a point of high dispersion in the lattice; the middle of the chicane, a short distance downstream of the chosen interaction point. For the effect to be as clear as possible, the emittance contribution to the beam size should be minimized and the energy spread of the beam without modulation should be as small as possible. This is achieved by making the emittance and beta functions (at the detection point) as small as possible and by taking additional care in setting up and optimising the accelerator.

In order to assess whether a detectable interaction was possible, a number of parameter sets were modelled. The results then gave an indication of what terahertz electric field strength would be necessary; these could then be compared to the values being obtained from simulations of the generation process and also the measurements being made as the antenna design was optimized and characterized. Particular ALICE electron beam parameters were also chosen in order to maximize the signal from any interaction that takes place; these were usually a compromise between what was ideal for this experiment and what could be realistically achieved when required without dominating the time available for experimentation. The following example of the results of a simulated interaction were calculated with these parameters: electron energy 15 MeV, normalized emittance  $30 \mu\text{m}$ , initial electron energy spread 10 keV, bunchlength 4 ps, integrated energy modulation due to interaction with the terahertz field 200 keV. Figure 1.19 (AW) shows the transverse profile of the beam in the ALICE chicane, illustrating the increase in the horizontal beam size ( $\sigma_x$ ) from 1.10 to 1.85 mm when terahertz is present.

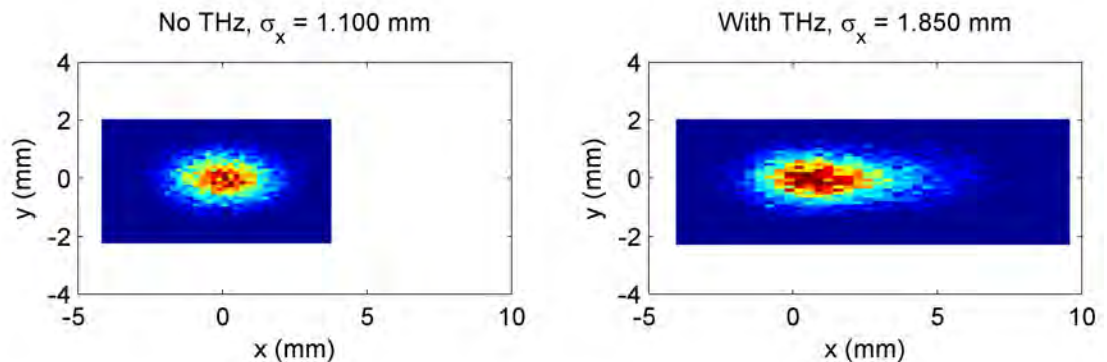


FIGURE 1.19: Simulation of the effect of the energy modulation due to interaction with terahertz radiation on the beam size in the ALICE chicane. The electron energy is 15 MeV, normalized emittance  $30 \mu\text{m}$ , energy spread 10 keV, bunchlength 4 ps, integrated energy modulation due to interaction with the terahertz field 200 keV

The upper plot of figure 1.20 (AW) shows the longitudinal phase space distribution of particles in a bunch; the black points are with no terahertz present while the red points are following interaction with a terahertz pulse. The lower plot shows the integrated intensity (in arbitrary units) plotted against horizontal position across the electron beam shown in figure 1.19, with the same colour coding.

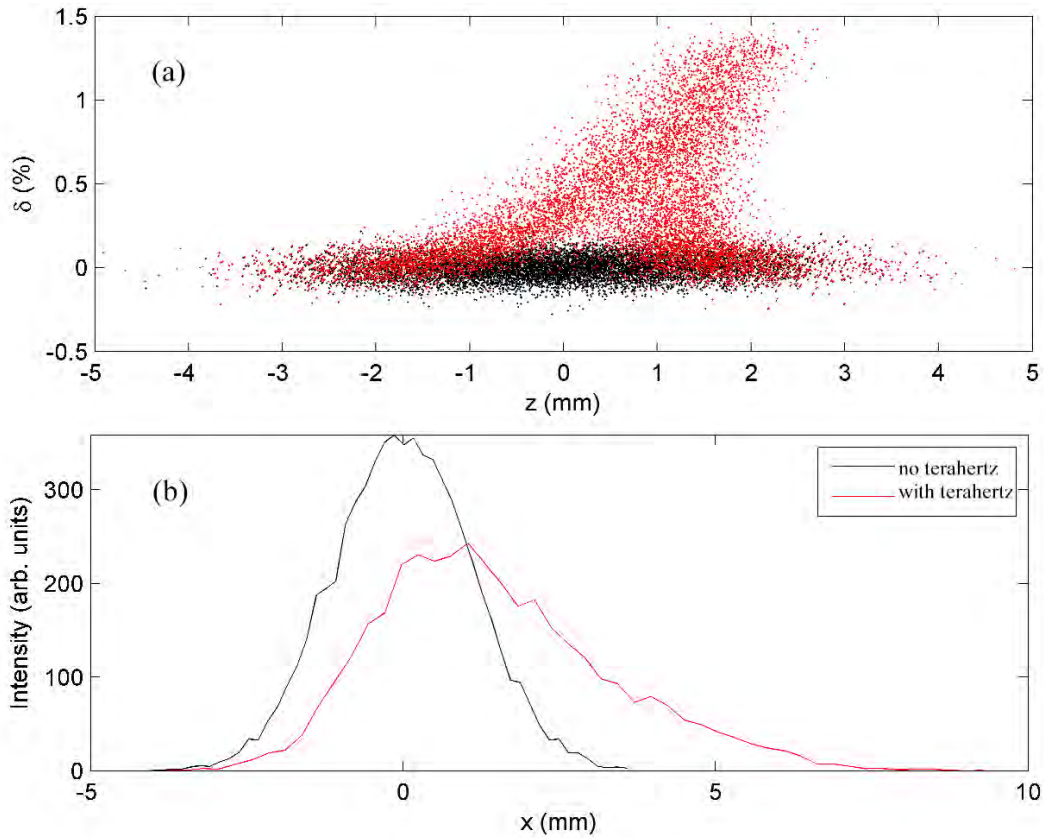


FIGURE 1.20: Simulation of the effect of terahertz-induced energy modulation on (a) energy spread and (b) integrated horizontal beam profile. All beam parameters the same as figure 1.19

Figure 1.21 shows a calculation of the effect of terahertz-induced energy modulation on the horizontal (black) and the vertical (red) beam sizes ( $\sigma_x$  and  $\sigma_y$ ) measured on the ALICE chicane YAG screen. All beam parameters and the magnitude of the energy modulation due to the interaction are the same as figure 1.19, while the noise level shown is representative of that observed in the real measurements recorded in Chapter 5. The results are plotted as a function of the relative timing of the electron bunch and the terahertz pulse. Each data point is a rolling average of five consecutive measurements, divided by the overall average. Note that this scenario is the best case, and the reality is likely to be significantly less optimal.

## 1.7 Overview of thesis layout

This material in this thesis is arranged in the following manner:

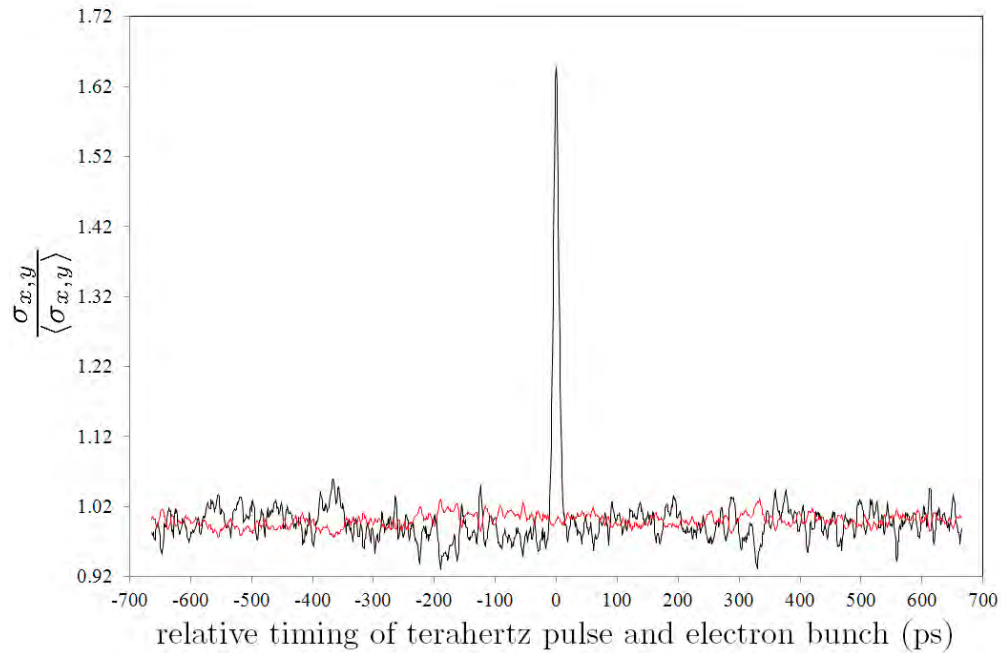


FIGURE 1.21: Simulation of the effect of terahertz-induced energy modulation on the horizontal (black) and the vertical (red) beam sizes ( $\sigma_x$  and  $\sigma_y$ ) on the chicane YAG screen beam image as a function of the relative timing of the electron bunch and the terahertz pulse. Each data point is a rolling average of five consecutive measurements, divided by the overall average. All beam parameters the same as figure 1.19, while the noise level shown is representative of that observed in the real measurements recorded in Chapter 5.

- Chapter 1 provides an introduction to the experiment that was undertaken, including analysis of the present state of the art and an outline of the theoretical basis for the experimental results recorded subsequently;
- Chapter 2 records the work done by the author in modelling and optimizing the terahertz-generating antenna;
- Chapter 3 records the experimental work done to characterize the improved antenna design and to verify the experimental procedure used to measure the electric field strength of the terahertz radiation thus produced;
- Chapter 4 lists the work done to the ALICE accelerator, both in terms of hardware changes and the establishment of new operating regimes, required for the experiment to be a measurable success;
- Chapter 5 records the experimental work done with the ALICE accelerator, for both establishing in-situ terahertz generation and measurement, and searches for interaction between the terahertz radiation and the electron beam;
- Chapter 6 is an analysis of what was achieved and what might be possible in the future.

## 1.8 Chapter summary

This chapter has provided an introduction to the experiment that was undertaken, including analysis of the present state of the art and an outline of the theoretical basis for the experimental results recorded subsequently.

## Chapter 2

# Modelling and Optimization of the Antenna Design

### 2.1 Introduction

This chapter records the work done by the author in modelling and optimizing the terahertz-generating antenna. Subsequent chapters will:

- Record the experimental work done to characterize the improved antenna design and to verify the experimental procedure used to measure the electric field strength of the terahertz radiation thus produced;
- List the work done to the ALICE accelerator, both in terms of hardware changes and the establishment of new operating regimes, required for the experiment to be a measurable success;
- Record the experimental work done with the ALICE accelerator, for both establishing in-situ terahertz generation and measurement, and searches for interaction between the terahertz radiation and the electron beam;
- Analyse what was achieved and what might be possible in the future.

Production of the short, intense pulse of terahertz radiation is achieved by triggering the electrical breakdown of a high voltage held between two electrodes attached to a piece of semiconductor. The semiconductor is briefly made conducting by illuminating it with a very short pulse (a few tens of femtoseconds) of infrared radiation from a Ti:S laser. In order to maximize the terahertz pulse's electric field strength at its focus point, it is necessary to maximize the voltage applied to the wafer between the electrodes. Earlier experiments had used relatively modest DC voltages (perhaps up to 10 kV) and electrodes cut from metal adhesive tape and stuck to the wafer, for example figure 2.1. It was clear that there was significant scope for improvement by applying standard high-voltage electrical engineering principles and by optimization of the dimensions using computer modelling.

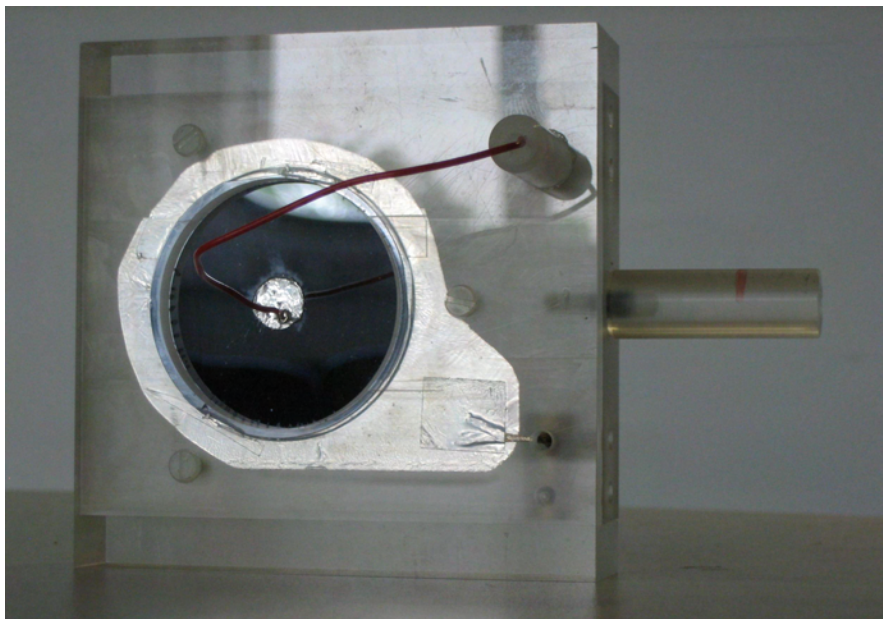


FIGURE 2.1: Initial antenna design, prior to the development recorded as part of this thesis

## 2.2 Problems with the existing antenna design

The main limitation on the electric field strength at the terahertz pulse's focus point is uncontrolled electrical breakdown between the high-voltage and ground electrodes on the wafer. The most likely breakdown mechanism is tracking on the surface of the wafer; initiated by the large electric field present at any sharp features on the high-voltage electrode. Because no surface can ever realistically be perfectly smooth or free of contaminants, there will always be surface features that mean the potential difference between any two points is not linearly distributed. This leads to a preferred route along which electrons can flow following these regions of higher field. Once a track has formed from the flow of charge between the electrodes, subsequent breakdowns are more likely along the established track, and will occur at a lower potential than the original breakdown. This is due to surface defects produced by the energy deposited by the flow of charge and chemical contamination deposited on the surface from the disassociation of atmospheric molecules.

## 2.3 Improvements to the antenna design and its operation

The traditional ways of controlling the environment to minimize high-voltage breakdown would be to either operate the device in a low pressure, low particulate-contaminated volume after careful cleaning or conversely in sulphur hexafluoride ( $\text{SF}_6$ ) gas at above atmospheric pressure. Although the first of these two approaches would have been feasible, it would have made the antenna assembly considerably more unwieldy and difficult to integrate onto a standard optical table. The potential for vibration from



FIGURE 2.2: High-voltage pulsed power supply (pulser)

attached vacuum pumps might also have been an issue, depending on what pumping system was employed. The option of employing a pressurized vessel containing  $\text{SF}_6$  was discounted from a safety and practicality standpoint; also the absorption of light by  $\text{SF}_6$  at the laser wavelength might have been an issue.

### 2.3.1 Pulsed power supply

Operation of the antenna with a pulsed high-voltage power supply enables a higher peak voltage to be achieved without breakdown [49]. As long as it is possible to synchronize the HV pulse and the laser, so that the wafer becomes conducting at or near the peak of the voltage waveform, this is a relatively straightforward way of improving the maximum voltage achievable. Existing high-voltage supplies were capable of 40 kV, 200 ns pulses at up to 100 kHz [50]. However, as we were developing a supply to operate at the same repetition rate as ALICE (which is capable of operating at up to 20 Hz) then an increase in maximum voltage could be traded for a reduction in the repetition rate.

The design and optimization of the pulsed HV supply was undertaken by RS, and makes use of a modified automobile ignition system, up-rated to give higher peak voltages. Figure 2.2 shows the HV pulser and figure 2.3 shows the enclosure built to house the antenna. The principal features of this are that it is constructed from non-conducting plastic but with an aluminium foil covering to restrict EM radiation emission from the terahertz generation process or electrical breakdown. The apertures that allow the laser light to fall onto the antenna and the terahertz radiation to leave are sufficiently small

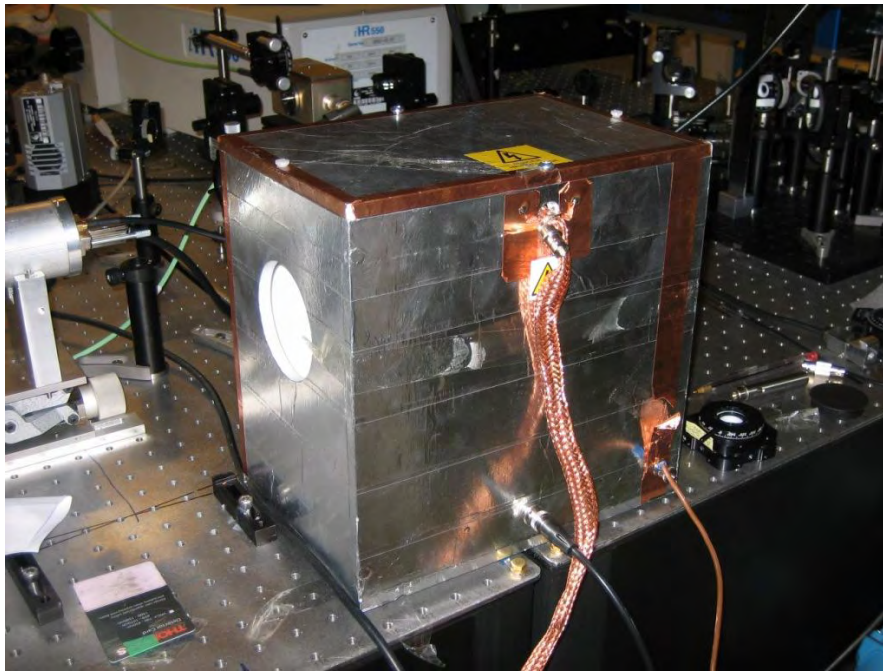


FIGURE 2.3: Antenna enclosure, showing the foil covering that was added to stop the EM pulse generated by the breakdown of the wafer interfering with other electronic equipment, the high-voltage connection (covered in copper braid), the voltage probe connection and the safety earth

that it is not possible to touch any high-voltage components when the enclosure is fully assembled. Inside the enclosure there is a voltage probe which provides a stepped down (by a factor of 4000) signal to allow measurement of the high-voltage pulse profile amplitude and timing. The circuit of this voltage probe is shown in figure 2.4.

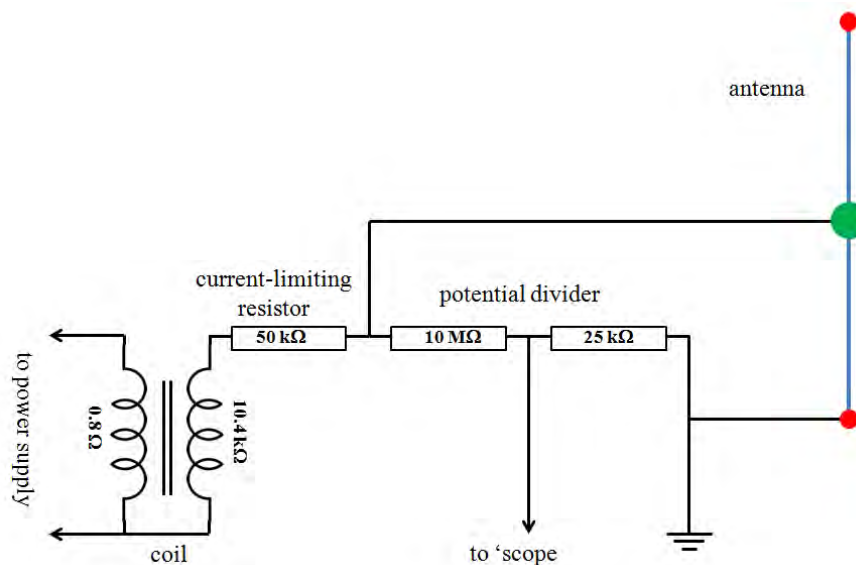


FIGURE 2.4: Probe circuitry inside antenna enclosure, providing a stepped-down voltage for measurement

### 2.3.2 Electrode profile

As explained earlier, the large electric field present at any sharp features on a high-voltage electrode will cause field emission and will act as the origin for breakdown tracks on the surface of the wafer. Thus the very sharp edge of the original electrodes (cut from metal adhesive tape) was clearly a significant weakness in the design. Although a mushroom-like cross-section would be ideal, as the edge of the electrode is then in a region of low potential gradient, for simplicity of manufacture a circular cross-section was used. The adoption of the mushroom-like cross-section is a potential future enhancement. To achieve a circular cross-section for the centre electrode, it was possible to use a standard ball-bearing of an appropriate radius, divided into two hemispheres. Figure 2.5 shows both the simple hemispherical centre electrode and the cross-section through the ideal geometry. An advantage of using a ball-bearing is that they have a very high quality surface finish (they are very highly polished to minimize friction) and thus they are ideal in high-voltage applications. To produce a spherical central electrode it is then necessary to sandwich the wafer between the two hemispheres. It is important to align both the halves concentrically, both to reconstruct the sphere correctly (so the cut edges do not become high field regions) and also so that there is no azimuthal variation in the field.

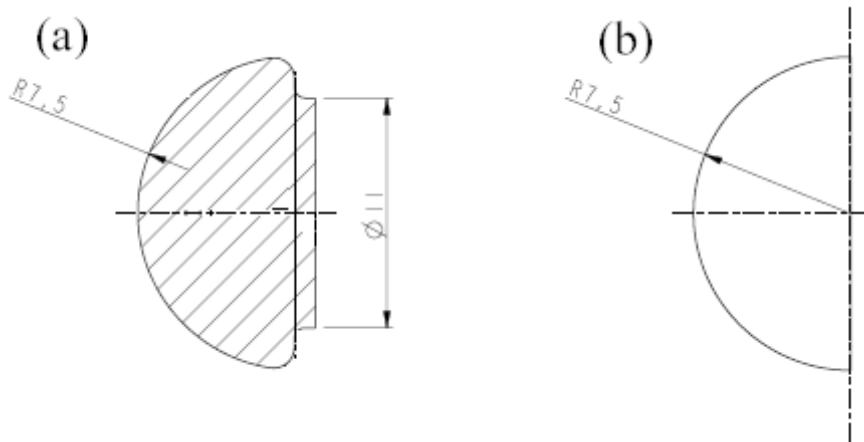


FIGURE 2.5: (a) Ideal centre electrode geometry, minimizing electric field strength at hemisphere edge, (b) geometry actually used, made from a bisected ball-bearing

To achieve a circular cross-section for the outer electrode, it was necessary to machine a torus with a niche into which the wafer would sit, as shown in figure 2.6.

### 2.3.3 Optimization of the geometry

In addition to removing all sharp edges to minimize any small areas of high electric field, which will potentially trigger electrical breakdown, it was hoped that by changing the radii of the two electrodes the potential distribution across the wafer could be manipulated to reduce the peak electric field level for any given potential difference between the electrodes. This would thus increase the potential difference between the two electrodes

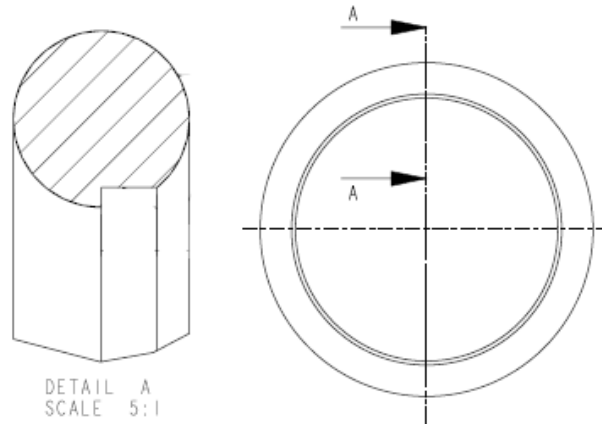


FIGURE 2.6: Outer electrode, with niche for the wafer to sit in

that could be maintained without breakdown, which would lead to a larger terahertz electric field in the pulse that is generated once the laser-stimulated breakdown occurs.

A rotationally-symmetric arrangement of a centre electrode mounted on a semiconducting wafer around which is wrapped another electrode can be considered as a thin slice of an infinitely long coaxial transmission line, for the purposes of estimating the electric field as a function of the radius  $r$ . If  $r_1$  is the radius of the centre electrode,  $r_2$  the radius of the wafer, which is also the inner radius of the torus of the outer electrode, and  $V$  is the potential difference between the two electrodes, then the electric field  $E$  at radius  $r$  is given by:

$$E(r) = \frac{V}{r \ln \frac{r_2}{r_1}} \quad (2.1)$$

The field is always greatest at  $r = r_1$ , whatever the ratio of  $\frac{r_2}{r_1}$  is. The minimum electric field at  $r = r_1$  is when  $\frac{r_2}{r_1} = e$ . This is illustrated in figure 2.7, which assumes  $r_2 = 37.5$  mm, corresponding to the model being based around a 75 mm diameter wafer.

In our real case, we do not have a thin slice of an infinitely long coaxial transmission line, but a structure that is rotationally symmetric (like the coaxial transmission line) which only extends a certain distance perpendicular to  $r$  ( $z$ -direction), thus introducing a  $z$ -dependence to the fields. As a starting point to simulating the antenna, we use the optimum dimensions suggested by the above analysis; for our 75 mm diameter wafer ( $r_2 = 37.5$  mm) this is  $r_1 = 13.8$  mm.

The Opera 2D electrostatic modelling software [51] was used to model a radial slice through the antenna; thus the whole antenna would be constructed by rotating the model around the  $r = 0$  axis. This approach is identical to creating a full 3D model, except that it is not possible to include any deviation from perfect radial symmetry, which the real antenna assembly will have if it is not carefully constructed. The electrodes are assigned the properties of a metal, while the wafer itself is a dielectric with relative permittivity (dielectric constant) of 13 and conductivity  $1 \times 10^{-6}$  S/m. For all models one electrode

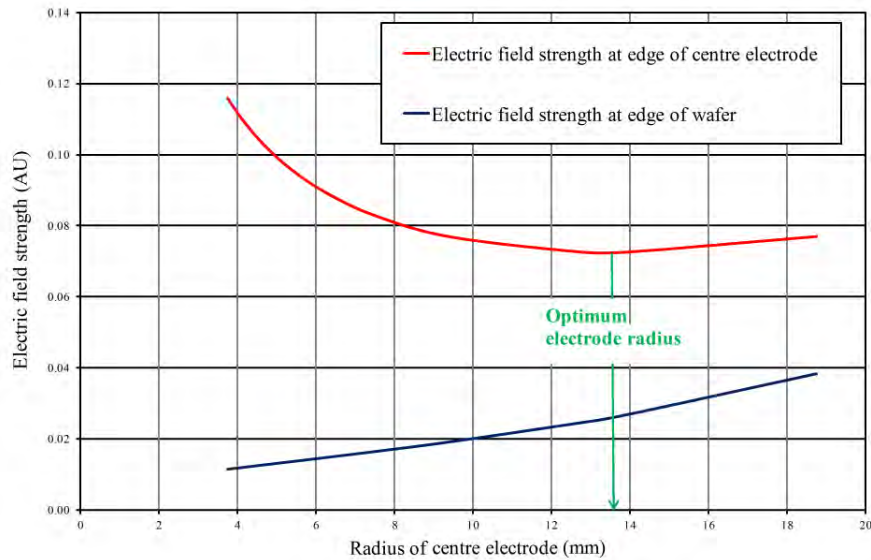


FIGURE 2.7: Electric field strength at the outer edge of the centre electrode (red) and the edge of the wafer (blue) as a function of the centre electrode radius, at a fixed voltage and wafer radius

is held at a nominal +30 kV and the other at ground. Apart from a couple of early simulations with non-spherical electrodes, the geometrical parameters varied were:

- $r_1$  = centre electrode radius;
- $r_3$  = the radius of the outer electrode cross-section.

$r_2$ , the inner radius of the torus of the outer electrode (the radius of the wafer) is of course fixed.

The size of the boundaries of the model were increased until they had no impact on the results of the simulation. Figure 2.8 shows two 2D slices through the antenna, one showing the regions defined in the Opera 2D model, and one showing the calculated potential when divided into ten regions with equally spaced (in potential) contour lines. This is the geometry chosen as starting point, where both the inner and outer electrodes have a circular cross-section with radius 13.75 mm.

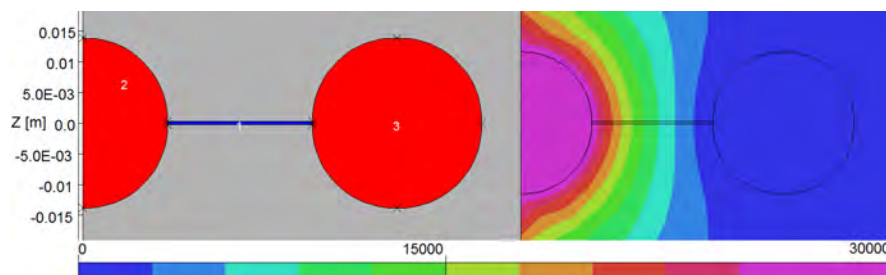


FIGURE 2.8: Opera 2D initial geometry and calculated potential distribution, used for antenna optimization.  $r_1 = r_3 = 13.75$  mm and centre electrode at +30 kV, outer electrode grounded

Figure 2.9 shows the calculated radial electric field ( $E_r$ ) along a radial line on the exposed part of the surface of the wafer between the electrodes. It also shows the analytical calculation of the field for a slice through an infinitely long coaxial cable with the same dimensions.

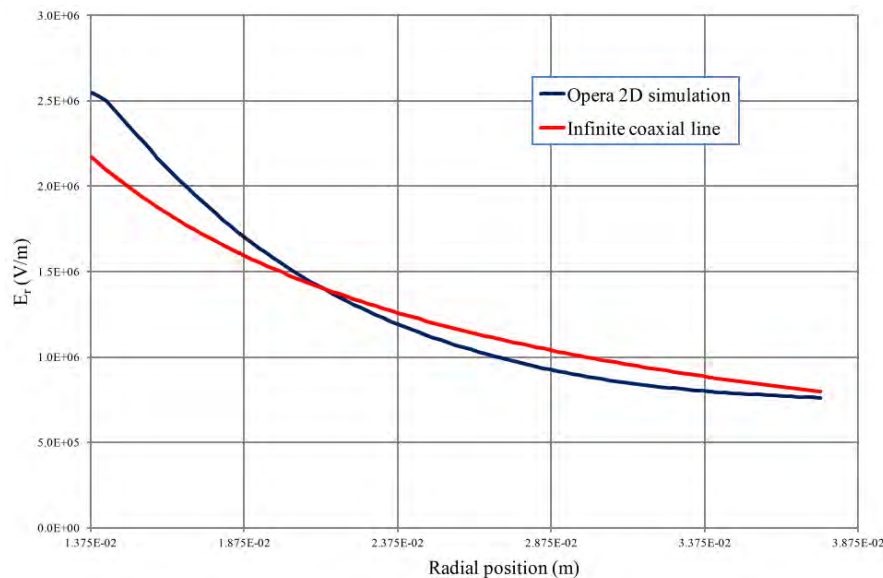


FIGURE 2.9: Opera 2D simulation result for the radial electric field ( $E_r$ ) (blue) and that for an analytical calculation of the field for a slice through an infinitely long coaxial cable with the same dimensions (red), along a radial line on the exposed part of the surface of the wafer between the electrodes

Subsequently the model was refined by replacing the semicircle of the central electrode with two quadrants sandwiching the wafer between them, representing the two hemispheres of the 3D wafer assembly. This is shown in figure 2.10. The effect of this change on the calculated electric field along the line on the wafer surface is visible only very close to the central electrode.

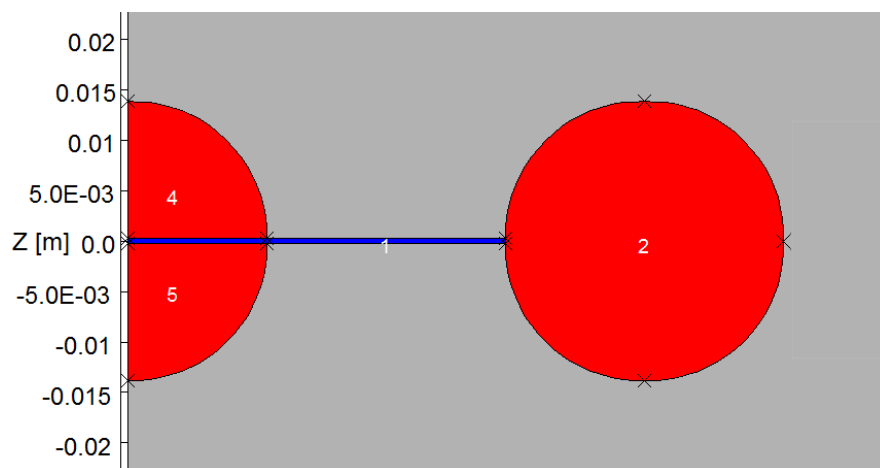


FIGURE 2.10: Improved Opera 2D region definition, showing the wafer (region 1) extending inside the central electrode (regions 4 and 5)

A demonstration of the importance of making the central electrode symmetrical was undertaken by modelling the antenna without the second hemisphere of the centre electrode present. This geometry is shown in figure 2.11, and the effect on the calculated field on figure 2.12. As expected, the effect of the edge of the hemispherical electrode is to increase the field strength, in this case by approximately 40 % .

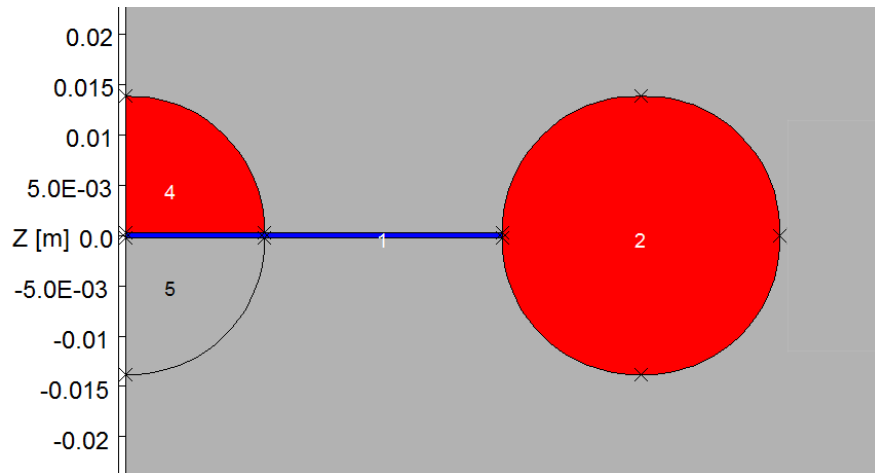


FIGURE 2.11: Opera 2D model used to confirm the desirability of employing two hemispherical electrode halves

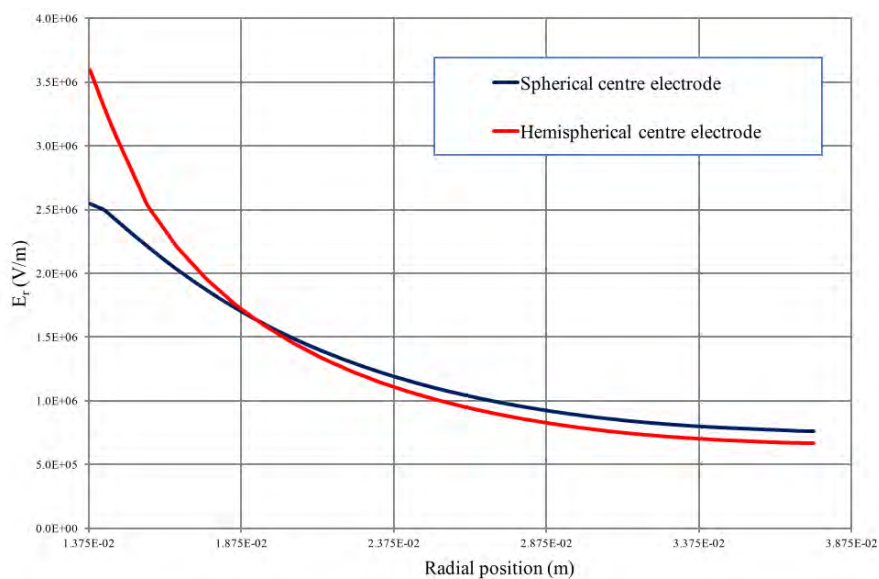


FIGURE 2.12: Opera 2D simulation result for the radial electric field ( $E_r$ ) with a spherical central electrode (blue) and for a hemispherical central electrode (red), along the same radial line on the surface of the wafer as figure 2.9

A number of Opera 2D models were produced to demonstrate the effect on the potential gradient across the surface of the wafer of changing the relative dimensions of the inner and outer electrodes. With the centre electrode positively charged and the outer electrode grounded, reducing the radius of the outer electrode relative to the inner electrode increases the field strength near the edge of the wafer and reduces it near the

centre electrode. As the electric field is always highest near the centre electrode, this leads to an overall reduction in the electric field. The results are shown in figure 2.13.

### 2.3.4 Final design used

As the variation of the electric field as a function of the relative sizes of the centre and outer electrodes does not have a sharp optimum, it was therefore possible to choose the sizes of the first electrodes manufactured somewhat arbitrarily within the range of dimensions explored in the simulations up to this point.  $r_1 = 7.5$  mm (as shown in figure 2.5 (b)) and  $r_3 = 5$  mm were chosen and the completed assembly can be seen in figure 2.16. The model of the final design and its potential distribution as calculated by Opera 2D is shown in figure 2.14 and the electric field on the surface of the wafer between the electrodes in figure 2.15.

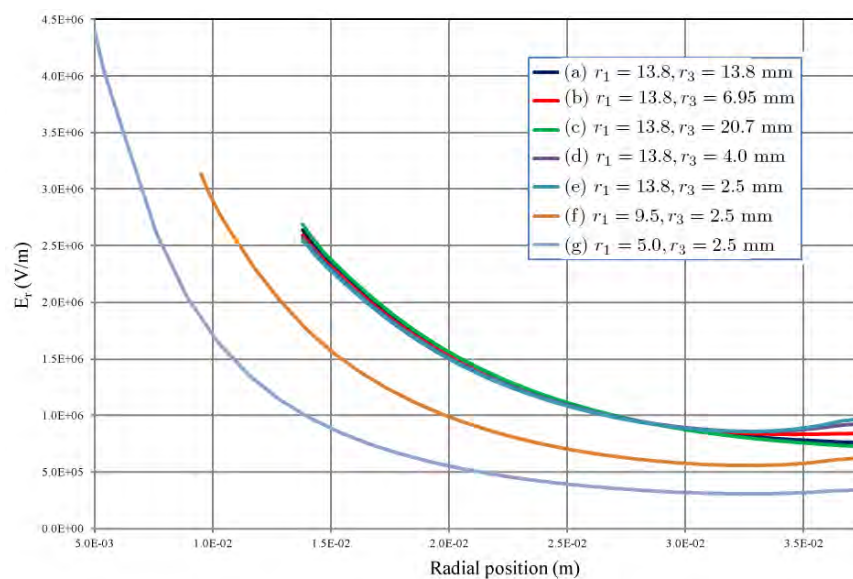


FIGURE 2.13: Opera 2D simulation result for the radial electric field ( $E_r$ ) for a range of values of  $r_1$  and  $r_3$

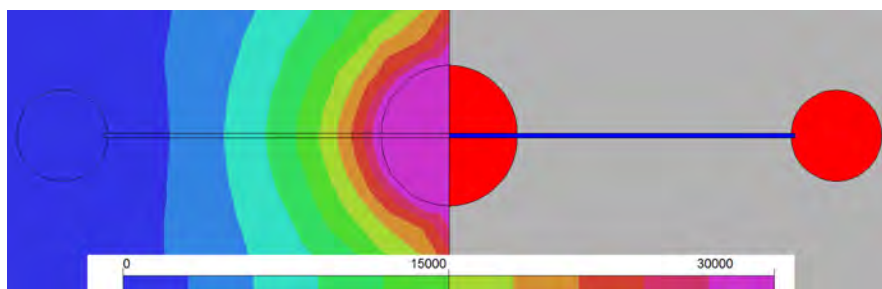


FIGURE 2.14: Opera 2D model of the final design and its calculated potential distribution

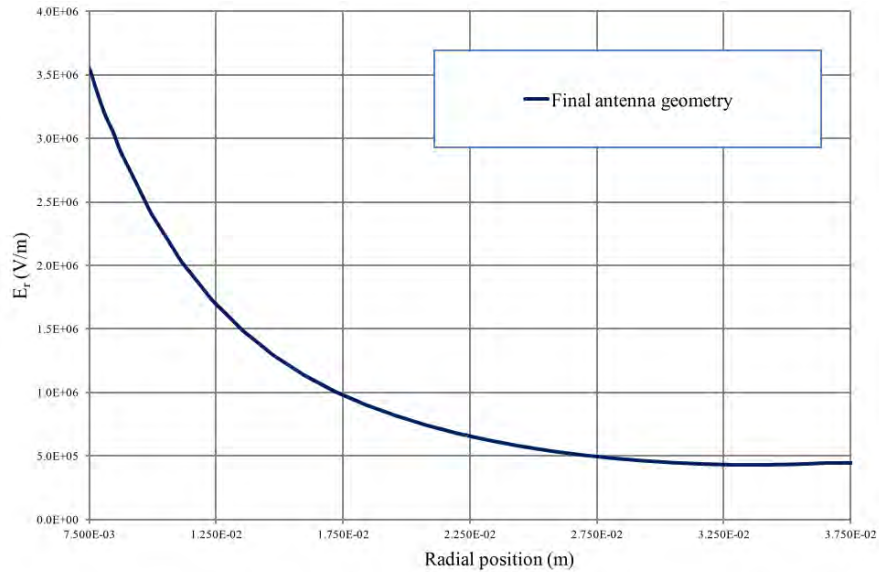


FIGURE 2.15: Opera 2D simulation of the radial electric field ( $E_r$ ) of the final design

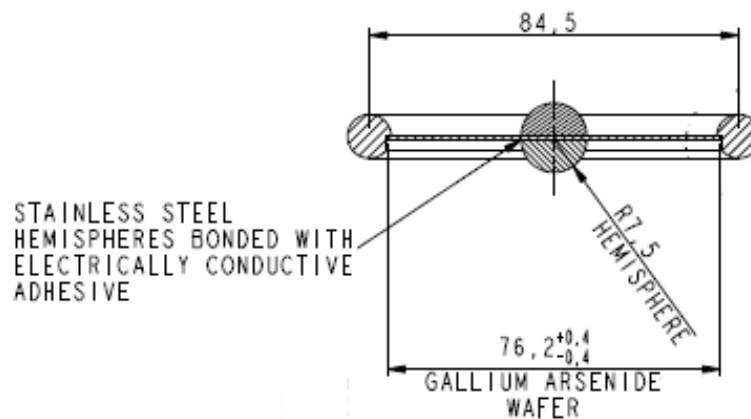


FIGURE 2.16: Cross-section through the final antenna design showing some construction details

### 2.3.5 Further enhancements

Possible enhancements for future experiments were also modelled in Opera. These consisted of modifying the cross-section of both the centre and outer electrodes of existing antenna design to shield the edge of the electrodes from high electric fields by moving them into a region of low potential gradient. Starting from the design shown in figure 2.14, only the centre electrode is modified initially (figure 2.17 (a)), then both electrodes are modified (figure 2.17 (b)).

The electric fields calculated by Opera, along the usual line on the wafer surface for the three cases, are shown in figure 2.18. The re-designed centre electrode seems to significantly reduce the peak field for a given voltage. As the existing centre electrode was undercut by 2 mm to create the new shape - the line on the wafer surface which Opera calculates the field starts at a radial distance 2 mm closer to the origin.

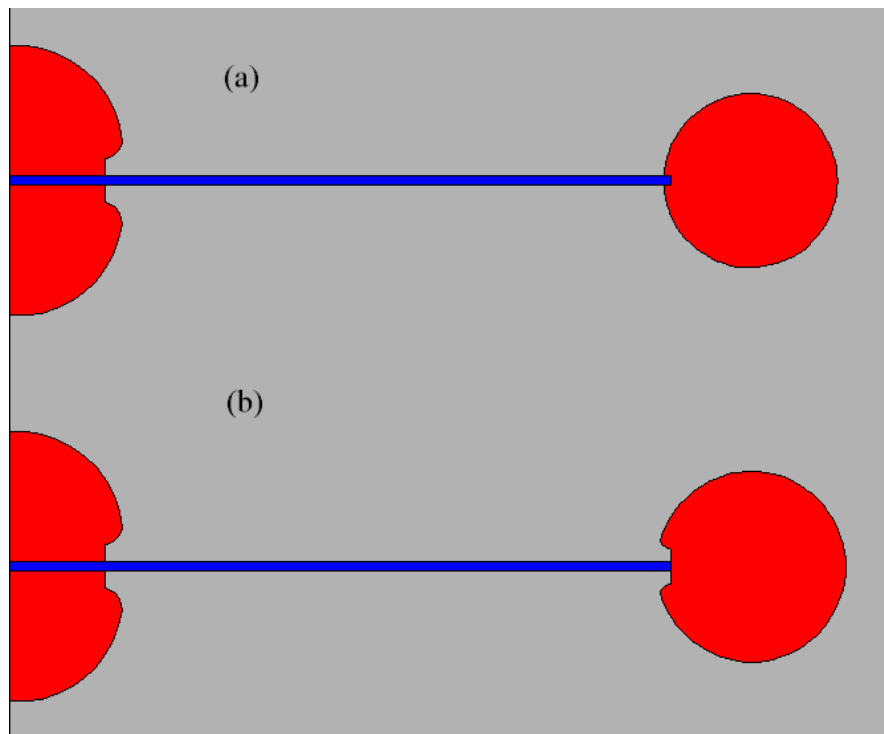
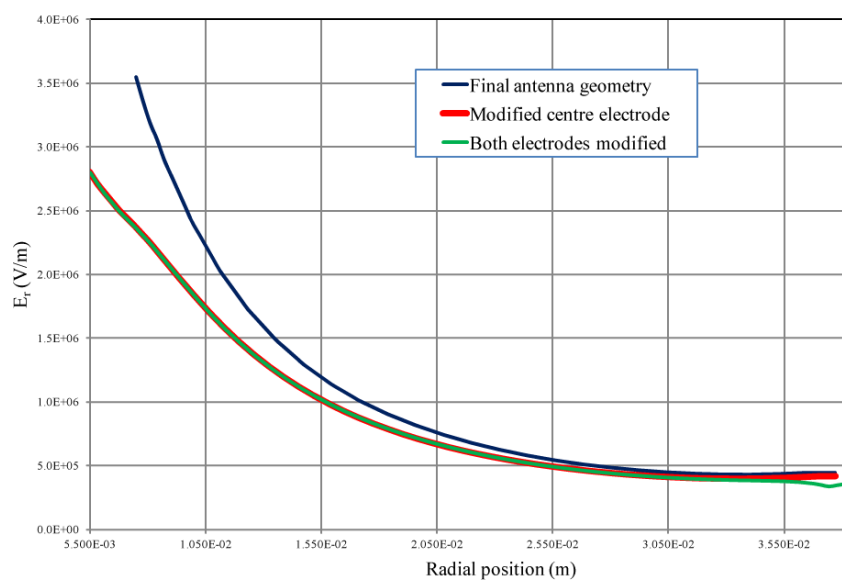


FIGURE 2.17: Opera 2D model of potential future electrode geometries

The reduction in the peak field is significant (even allowing for the extra 2 mm distance over which the 30 kV is distributed) and therefore the modified centre electrode design is being pursued for the next series of experiments (after the work recorded in this thesis). The additional difficulty and expense of modifying the outer electrode does not appear to give significant benefits.

FIGURE 2.18: Opera 2D simulation of the radial electric field ( $E_r$ ) of potential future electrode geometries

## 2.4 Antenna construction

### 2.4.1 Attachment of the electrodes

In order to attach the electrodes to the wafer, a silver-loaded epoxy was used. When assembling the antenna, the aims were:

1. To get the two hemispherical centre electrode components as concentric as possible with each other;
2. To get the centre electrode as concentric as possible with the wafer;
3. To get a smooth bead of adhesive at the edge of each centre electrode hemisphere so that a sharp edge which might generate field emission is eliminated;
4. Not to leave any contamination (adhesive, dirt, finger grease etc.) on the wafer which would provide a breakdown source.

The various stages of the assembly of the antenna are shown in figure 2.19. The outer electrode was not attached to the wafer with adhesive on the first example of this antenna built. Instead it relied on the fact that the whole antenna assembly was supported in a plastic holder to hold the outer electrode and the wafer together. The second antenna assembly built had the outer electrode attached to the edge of the wafer with the same conducting epoxy as was used for the centre electrode.



FIGURE 2.19: Stages of antenna assembly

### 2.4.2 Electrical connections

The next problem was how to make an electrical connection to the centre electrode without destroying the smooth feature-less form that was the overriding aim of the design. The initial solution, which was not subsequently improved upon, was to use a blob of the electrically conducting epoxy adhesive to attach the end of a wire to the centre of each hemisphere. As long as the blob of adhesive itself was reasonably smooth and feature-less, and the sharp ends of the wire were fully embedded in it, this appeared to be a reasonable method. This is illustrated in figure 2.20. No subsequent electrical breakdowns of the wafer were traced to this wire attachment method.

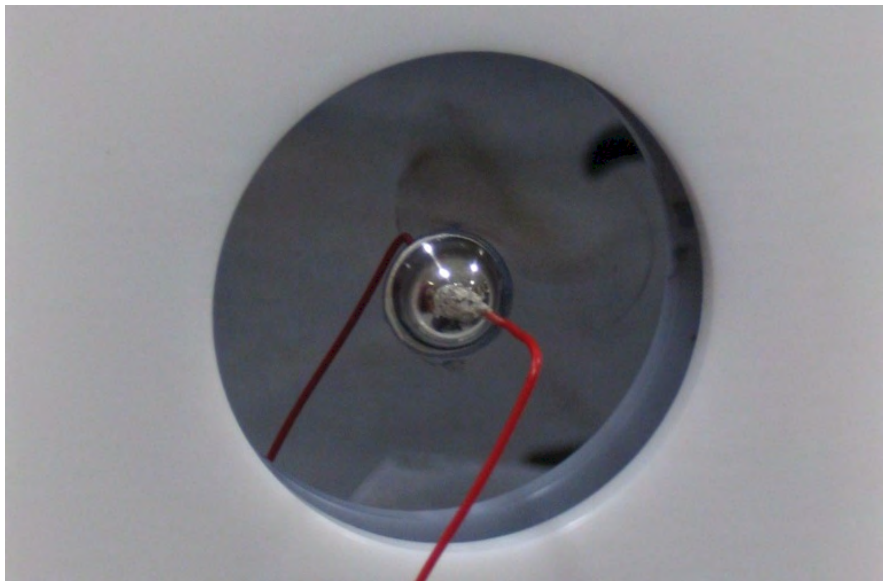


FIGURE 2.20: Detail of electrical connection

## 2.5 Results

The antenna design prior to this optimization (consisting of a DC power supply and electrodes cut from metal adhesive tape and stuck to the middle of the wafer, as seen in figure 2.1) could only be operated at less than 10 kV before breakdown occurred. The first example of the newly-optimized electrode design and pulsed HV power supply was operated routinely at 50 kV. The second model, which differed from the first only by having the two hemispherical centre electrode components much more concentric with each other and the outer electrode attached to the edge of the wafer with adhesive, could initially support 140 kV and was then operated routinely at 130 kV.

## **2.6 Chapter summary**

This chapter has recorded the work done by the author in modelling and optimizing the terahertz-generating antenna. The new antenna design, following this optimization process, was demonstrated to support an order of magnitude greater voltage as a result of the improvements made to its design by the author and improvements made to its power supply by RS.



## Chapter 3

# Measurements in the ALICE Diagnostics Room

### 3.1 Introduction

This chapter records the experimental work done to characterize the improved antenna design and to verify the experimental procedure used to measure the electric field strength of the terahertz radiation thus produced. Subsequent chapters will:

- List the work done to the ALICE accelerator, both in terms of hardware changes and the establishment of new operating regimes, required for the experiment to be a measurable success;
- Record the experimental work done with the ALICE accelerator, for both establishing in-situ terahertz generation and measurement, and searches for interaction between the terahertz radiation and the electron beam;
- Analyse what was achieved and what might be possible in the future.

Prior to working in the accelerator area, a set of measurements were made using apparatus in the ALICE Diagnostics Room. The purpose of these measurements was two-fold:

1. To measure the strength of the electric field of the terahertz radiation produced by the optimized antenna design whose development was described in Chapter 2, to confirm that the expected increase had been achieved;
2. To quantify the magnitude and distribution (both temporally and spatially) of the terahertz radiation in order to provide data to benchmark simulations of terahertz production and its detection via the EO effect or interaction with an electron beam.

As described in Chapter 1, we made use of the EO effect in order to measure the strength of the electric field in the terahertz pulse. The output of the Ti:S laser was used

both as the pump beam, generating the terahertz radiation from the antenna (about 90% of its intensity) and the probe beam (the remaining 10%) whose polarization state was modified as it passes through a ZnTe crystal in the simultaneous presence of the terahertz radiation.

### 3.2 Experimental arrangement

A schematic of the optical setup used in the ALICE Diagnostics Room is shown in figure 3.1. The detection system could either be a sensitive camera which could image the whole of the ZnTe crystal, providing information about the spatial distribution of the terahertz pulse; or a polarizing beamsplitter, two photodiodes and a lock-in amplifier to measure the sum and difference of the signal from the photodiodes. In addition, the latter arrangement required a chopper to block every other pump beam pulse, enabling a background signal to be subtracted from the photodiode signal. For temporal overlap of the terahertz and probe beams at the ZnTe crystal the pathlengths of the two arms must be identical to within a few millimetres. An optical delay line consisting of two mirrors mounted on a computer-controlled translation stage then allows the relative timing of the two pulses at the ZnTe crystal to be adjusted.

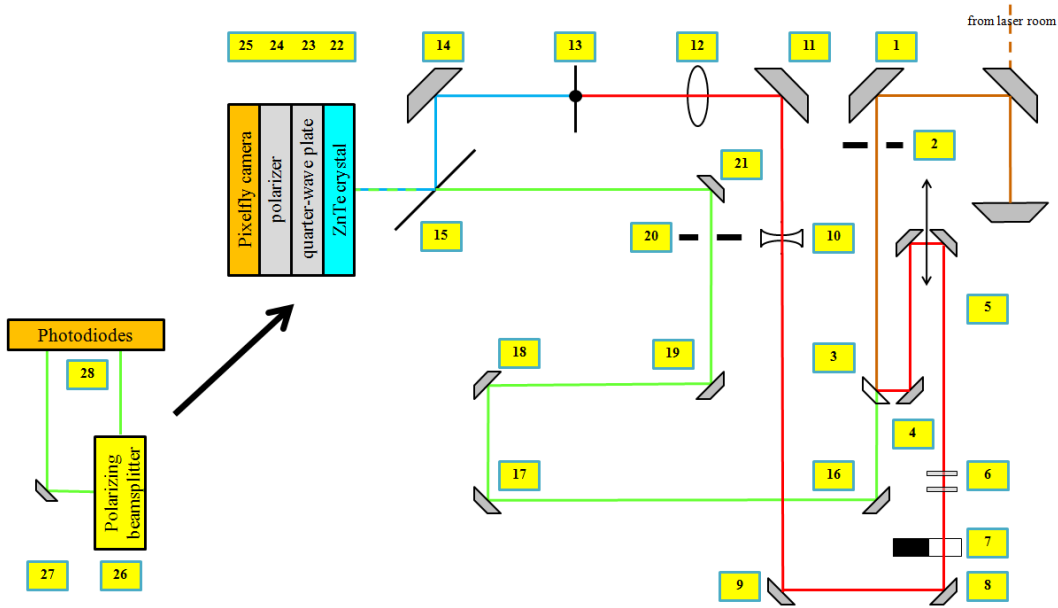


FIGURE 3.1: A schematic of the optical setup used in the ALICE Diagnostics Room

The output beam from the Ti:S laser enters the ALICE Diagnostics Room at floor level and is transported up to optical table height by a periscope. The first mirror (1) turns the beam through  $90^\circ$  (or is removed to check the temporal compression (see below) of the pulses) after which it passes through an iris (2). This is arranged to be centred on the beam and is useful to determine if any subsequent misalignment is due to components upstream of the optical table. A beamsplitter (3) reflects about 90% of the light through  $90^\circ$  to form the pump beam while 10% of the light passes through.

Another mirror (4) turns the pump beam through  $90^\circ$  and into the optical delay line (5). The beam exiting the optical delay line passes through two optional sets of neutral density filters (6) and then the mechanical chopper wheel (7). For measurements with the lock-in amplifier and photodiodes this operates at half the repetition rate of the laser and is synchronized to both the laser and the lock-in amplifier. For measurements with the camera it is parked at an open position. Two further mirrors (8 and 9) turn the pump beam through  $180^\circ$  before a diverging lens (10) is used to start the beam expanding. A mirror (11) turns the pump beam through  $90^\circ$  and onto a focussing lens (12) and then onto the antenna assembly (13), where it is converted into terahertz radiation.

Meanwhile the probe beam reflects off a number of mirrors (16 to 19) to increase its pathlength before passing through an iris (20) and by-passing the antenna assembly via another mirror (21) before passing through the optical element that must combine the probe and terahertz beams onto the same optical path. This is a thin piece of float glass with a coating of indium-tin oxide which is transparent to light at 800 nm (the probe laser for example) but reflects terahertz radiation. Due to its coating, this optical component is known as the ITO. The probe beam passes through the ITO (15) before arriving at the ZnTe crystal (22). (Omitted from this description and the schematic, to improve clarity, is a half-wave plate which can be used to rotate the plane of polarization of the probe beam and a neutral density filter used to attenuate the probe beam during alignment.)

The terahertz radiation is reflected off another plane mirror (14) and also the ITO before it too arrives at the ZnTe crystal. This is followed by a quarter-wave plate (23) to correct any residual birefringence in the ZnTe crystal (without any terahertz electric field present). If the camera-based detection system is being used, the ZnTe crystal is followed by a crossed polarizer (24) (i.e. one with its axis perpendicular to the polarization plane of the probe beam) and a Pixelfly camera (25) set up to image the ZnTe crystal. Alternatively, the polarizer is replaced by a polarizing beamsplitter (26) and a mirror (27) to rotate the straight-on beam onto one of two photodiodes (28). Figure 3.2 shows some photographs of the optical table taken during its assembly, the schematic of which was shown in figure 3.1.

Variables in the experimental set-up included the laser pulse repetition frequency (not important), the plane of polarization of the probe beam (affecting the orientation of the crossed polarizer only), the thickness of the ZnTe crystal (a thicker crystal is more sensitive, but has potentially more residual birefringence that might be difficult to eliminate with the quarter-wave plate) and the orientation of the ZnTe crystal. This can be produced so that it is sensitive to either longitudinal or transverse terahertz electric field. Part-way through the measurements the effective focal length of the diverging and converging lens combination in the pump beam was increased to replicate more accurately the layout that was being built in the accelerator, where these measurements were going to be repeated, with the aim of ultimately observing the effect of the interaction between the terahertz pulses and the electron beam.



FIGURE 3.2: A photomontage of the optical table in the ALICE Diagnostics Room during assembly

Two existing Matlab programs were used: the first to control the translation stage and record the images from the camera; the second to control the translation stage and record the signal from the lock-in amplifier.

Following any re-alignment of the optics of the pump or probe beams (this includes before the beamsplitter too as this will affect the paths followed after the beamsplitter) it was necessary to find the position of the optical delay line translation stage that corresponded to temporal overlap of the probe beam with the terahertz pulse at the ZnTe crystal. This usually required the collection of data over a particularly large range of translation stage positions.

### 3.3 Laser operation

In general, little day-to-day adjustment of the laser was required in order for it to maintain a reasonable operating standard; small adjustments to the timings of the amplifier's Pockels cells were usually sufficient to produce an output power of a few watts at a repetition rate of 1 kHz; occasionally the temporal compression of the pulses would need to be optimized by adjusting the motor-driven mirrors of the compressor. By placing a focussing lens in the beam path ionization of the air at the focus can be used to indicate the degree of compression. If the pulse is well-compressed there is sufficient electric field strength at the focus to ionize the air, which can be seen and heard.

Occasionally, the seed component of the laser system would lose or fail to find mode-lock. In this case a significant cleaning exercise of the optics of this stage was usually required.

### 3.4 Analysis of the experimental measurements (DL)

Although the goal of this experiment was to produce terahertz radiation pulses with significant on-axis *longitudinal* electric field at their focus, the measurement of a *transverse* field implies the existence of a longitudinal electric field. This is a consequence of Maxwell's equations. A very brief attempt was made to record some data using a ZnTe crystal cut to be sensitive to longitudinal electric field; this was not pursued further as it then became necessary to concentrate on establishing the second measurement in the accelerator. Thus all the measurements recorded here are of the transverse field and were made after the longer focal length arrangement was adopted, more accurately duplicating the layout that was being built in the accelerator.

#### 3.4.1 Calibration of the terahertz electric field as a function of the quarter-waveplate angle at minimum intensity

As explained in section 1.5.1, the intensity of the probe beam recorded at any  $(x, y)$  position after it has passed through the ZnTe crystal, quarter-waveplate and crossed polarizer, can be used to calculate the electric field of any terahertz radiation present simultaneously, via polarization-plane rotation due to the EO effect in the crystal. If the intensity is measured at a number of different rotational positions of the quarter-waveplate, a curve can be fitted to the data points which has a minimum, the value of which is a function of the polarization-plane rotation due to the EO effect and therefore the electric field strength of the terahertz radiation. Figure 3.3 shows an example of this curve fitting to the data, which in this case exhibits minimum signal at a quarter-waveplate angle of  $1.5^\circ$ .

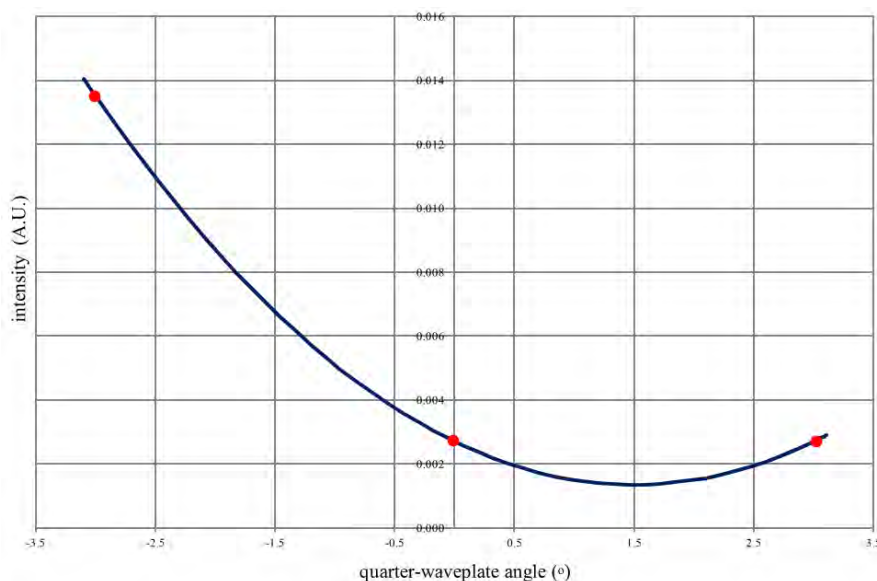


FIGURE 3.3: Probe beam intensity at three different quarter-waveplate angles and curve fitted to measured data points, showing a minimum at an angle of  $1.5^\circ$

The value of this minimum can be calculated as a function of the electric field strength of the terahertz radiation and the physical properties of the optical components; Figure 3.4 shows the results of two calculations, one with a 1.0 mm ZnTe crystal; the other with a 0.5 mm ZnTe crystal. This figure thus serves as the calibration with which the data recorded in the form of figure 3.3 can be used to determine the terahertz electric field strength.

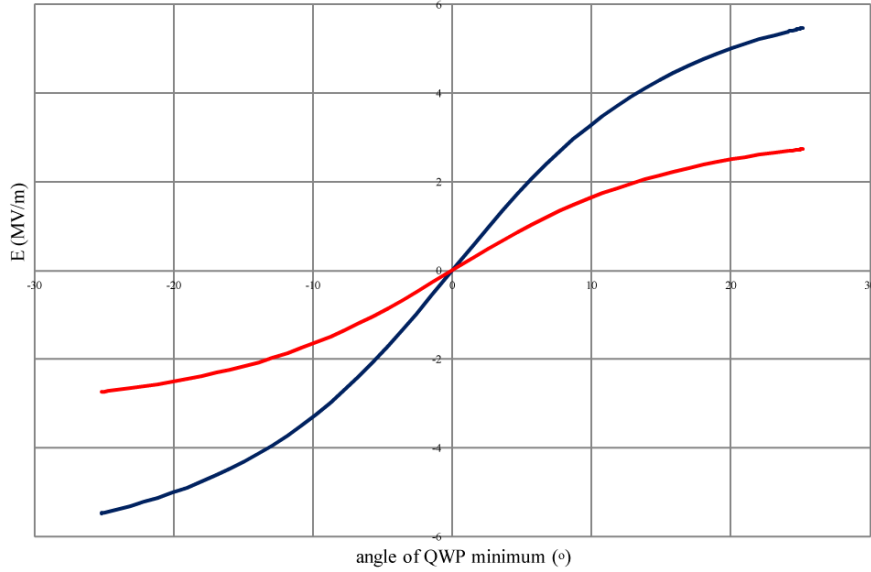


FIGURE 3.4: Terahertz electric field strength as a function of quarter-wave plate angle for the minimum transmission to the detection camera; for a 0.5 mm ZnTe crystal (blue) and for a 1.0 mm ZnTe crystal (red)

### 3.4.2 Measurement of the terahertz electric field across the ZnTe crystal

Figure 3.5 shows a series of images of a 1.0 mm ZnTe crystal recorded by the Pixelfly camera as the relative timing between the two pulses is changed in time steps of 0.067 ps. The antenna is operating at 130 kV. As the relative timing of the terahertz pulses and the probe beam is changed first one lobe and then the second appear and disappear. This demonstrates that the alignment of the two beams is not perfect, introducing a timing difference in the horizontal plane, which will lead to the maxima seen each side of the centre not occurring at precisely the same time.

Extracted from the images in figure 3.5, after the subtraction of a background (recorded with no voltage on the antenna and therefore no terahertz present), figure 3.6 shows the calculated terahertz electric field strength, at twenty points in a horizontal line across the centre of the crystal, as a function of the relative timing of the pulses. This uses the calibration recorded at the start of this section.

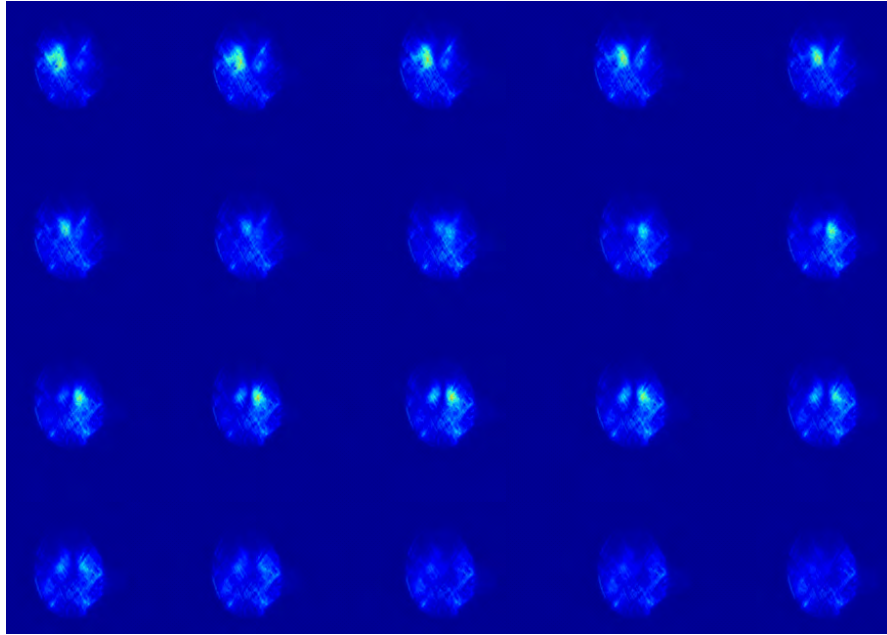


FIGURE 3.5: Images of the ZnTe crystal as the relative time of arrival of the terahertz pulse and the probe laser pulse is changed in steps of 0.067 ps, with the antenna operating at 130 kV. Careful examination of this figure reveals the timing error induced by imperfect alignment in the horizontal plane, as the maximum intensity of the left and right lobes does not occur on the same image.

### 3.4.3 Terahertz electric field as a function of the antenna alignment

Using a 1.0 mm ZnTe crystal with the antenna operating at 120 kV, the terahertz electric field is measured with the complete antenna housing rotated  $\pm 5^\circ$  around the  $y$ -axis. Figure 3.7 shows the terahertz electric field calculated at ten points in a horizontal

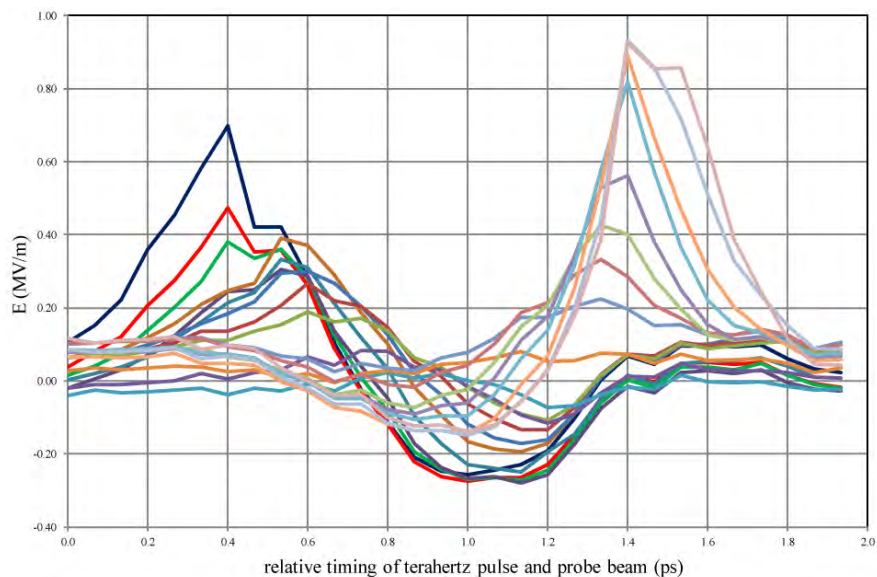


FIGURE 3.6: Calculated terahertz electric field strength, at twenty points in a horizontal line across the centre of the crystal, as a function of the relative timing of the pulses, extracted from the images in figure 3.5

line across the centre of the crystal, as a function of the relative timing of the pulses. The red trace is with the antenna assembly nominally at  $0^\circ$ , the blue and green traces corresponding to  $+5$  and  $-5^\circ$  respectively.

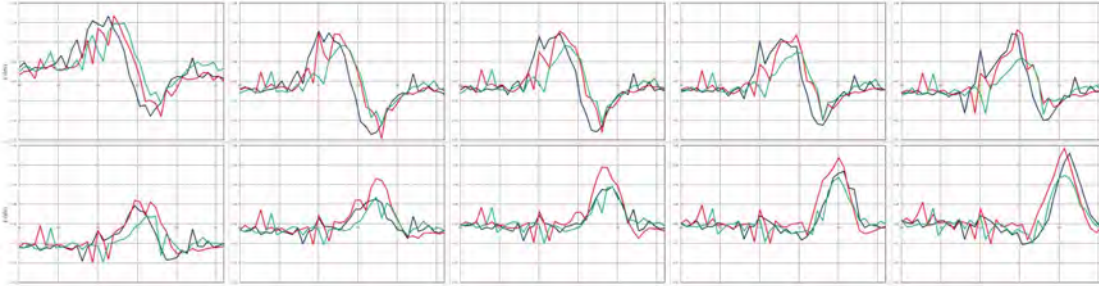


FIGURE 3.7: Terahertz electric field strength, at ten points in a horizontal line across the centre of the crystal, as a function of the relative timing of the pulses, as the complete antenna housing rotated around the  $y$ -axis, nominally at  $0^\circ$  (red),  $-5^\circ$  (blue) and  $+5^\circ$  (green)

There is no strong dependency seen in either the amplitude or timing of the signal. As it would have been difficult to precisely align the antenna (as it is enclosed in a box for safety and shielding reasons) this is an important result.

#### 3.4.4 Terahertz electric field as a function of the antenna voltage

This time using a 1.0 mm ZnTe crystal, the antenna voltage was varied in 20 kV steps, from 140 to 60 kV, with a final data point also taken at 44 kV. Figure 3.8 is a plot of the intensity of the terahertz pulse (i.e. the square of the electric field amplitude recorded at one point on the crystal) as a function of the relative timing of the terahertz and probe beam pulses. Figure 3.9 is a plot of each of the traces in figure 3.8 integrated with respect to time, as a function of antenna voltage. From 80 to 140 kV there is a clear linear relationship, as would be expected. The data points at 44 and 60 kV deviate from this linear relationship, apparently recording a larger intensity than would be expected. This could be due, for example, to the measurement noise in the data becoming larger compared to the real signal.

#### 3.4.5 Terahertz electric field as a function of pump laser intensity

Using neutral density filters to reduce the intensity of the pump beam, the terahertz electric field strength was measured at ten points in a horizontal line across the centre of a 1.0 mm ZnTe crystal, and with the antenna operating at 120 kV. The difference between the maximum and minimum electric field recorded as a function of the relative timing was calculated for each point. Figure 3.10 is a plot of this value, for each of the ten points on the crystal, as a function of the transmission of the filter. There is no indication that the terahertz field is saturating, and therefore it would be possible in the future to increase the terahertz electric field strength by increasing the laser power; for

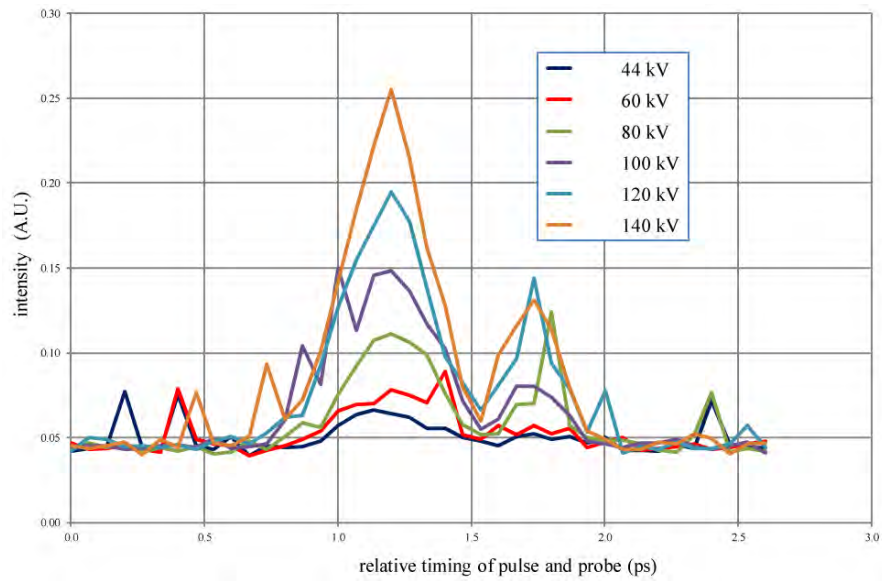


FIGURE 3.8: Terahertz pulse intensity as a function of the relative timing of the terahertz and probe beam pulses

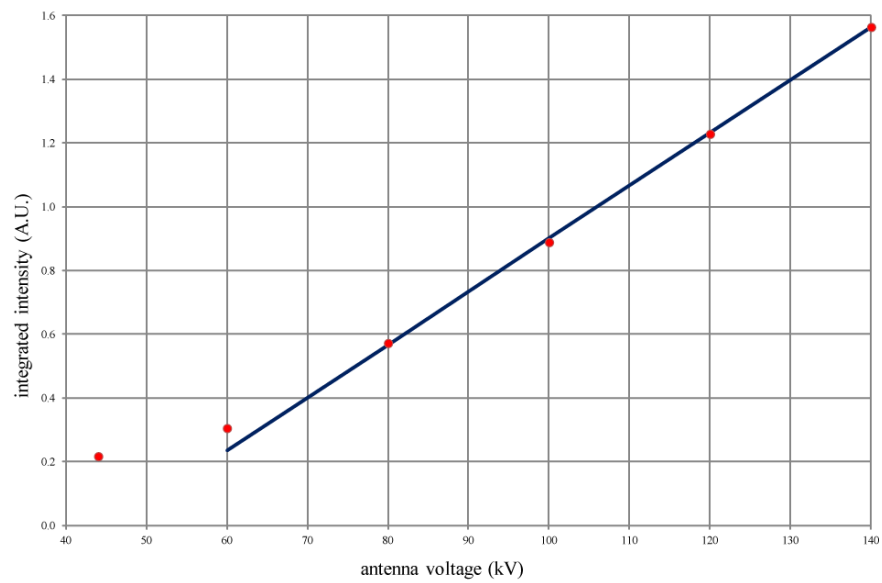


FIGURE 3.9: Integrated terahertz pulse intensity as a function of antenna voltage

example by using some of the further amplification stages available on the existing Ti:S laser.

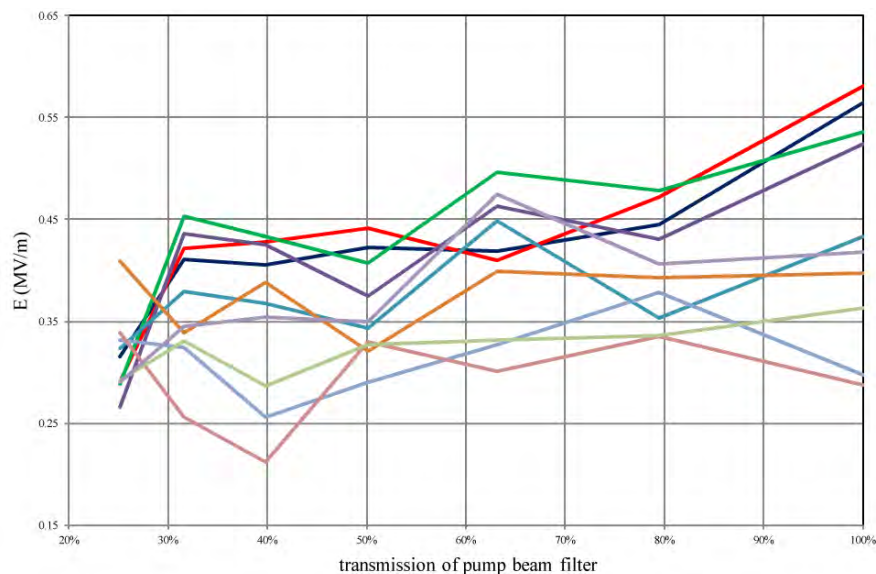


FIGURE 3.10: Terahertz electric field strength as a function of the transmission of filters in the pump beam, at ten points in a horizontal line across the centre of a 1.0 mm ZnTe crystal and with the antenna operating at 120 kV. There is no indication that the terahertz electric field strength is saturating at higher laser powers, so it would be possible to increase the terahertz electric field by increasing the laser power.

### 3.5 Chapter summary

This chapter recorded the measurements of the terahertz electric strength made using the techniques described in chapter 1, obtained using the improved terahertz-generating antenna developed in chapter 2. It can be concluded that:

- We developed a robust and repeatable method to measure the electric field of a radially-polarized terahertz pulse produced by the electrical breakdown of a radially-symmetric photoconductive antenna;
- The new antenna design and pulsed power supply increased (by more than an order of magnitude) the voltage that could be applied to the wafer before it broke down;
- Terahertz electric fields of more than 0.5 MV were measured; although these are transverse fields there must be a longitudinal field of very similar magnitude present for Maxwell's equations to be satisfied;
- At the much-higher antenna voltages that are now possible, the pump laser beam energy is now the limiting factor on the terahertz electric field;
- The terahertz electric field is not very sensitive to the antenna alignment.

## Chapter 4

# Set Up and Assembly of the Equipment in the ALICE Accelerator Hall

### 4.1 Introduction

This chapter records the work done to the ALICE accelerator, both in terms of hardware changes and the establishment of new operating regimes, required for the experiment to be a measurable success. Subsequent chapters will:

- Record the experimental work done with the ALICE accelerator, for both establishing in-situ terahertz generation and measurement, and searches for interaction between the terahertz radiation and the electron beam;
- Analyse what was achieved and what might be possible in the future.

Preparation for the experimental verification of the interaction of the terahertz radiation pulse with the electron beam in ALICE consisted of two major activities; the construction of a duplicate terahertz source and means of measuring the terahertz field intensity within the accelerator hall, and secondly modifications to the ALICE accelerator hardware and typical beam parameters to enable an interaction to be detected. Figure 4.1 shows the layout of ALICE within the two accelerator halls, known as Area 1 and Area 2. The majority of the AEMITR experiment is located in Area 2 (where the EMMA accelerator is also located), except the additional electron beam diagnostics installed in the bunch compression chicane in Area 1. This drawing shows ALICE before the installation of the AEMITR hardware.

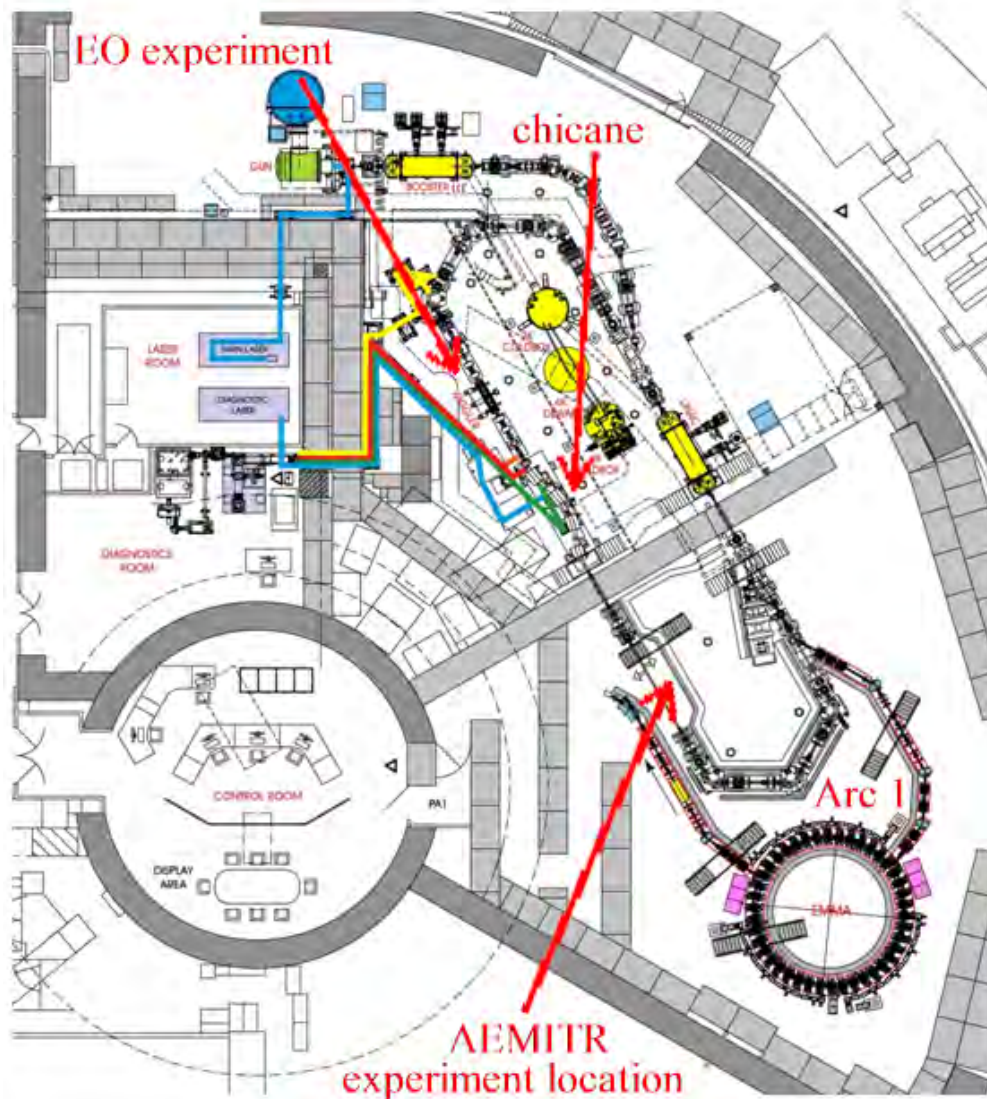


FIGURE 4.1: Layout of the ALICE complex, including the Laser, Diagnostics and Control Rooms, the ALICE accelerator (spanning the two accelerator halls, Area 1 and Area 2), the EMMA accelerator in Area 2, the location of most of the AEMITR experiment, the bunch compression chicane, Arc 1 and the EO experiment in Area 1

## 4.2 Terahertz generation

The intention was that the terahertz generation system developed in the Diagnostics Room would be functionally identical to that which would eventually be built in the accelerator hall, the only differences in the latter being in the spacing of elements of the system and the need to make all adjustments (at least in theory) remotely controlled so that optimization is possible when the accelerator is operating and there is no personnel access.

### 4.2.1 Laser beam transport

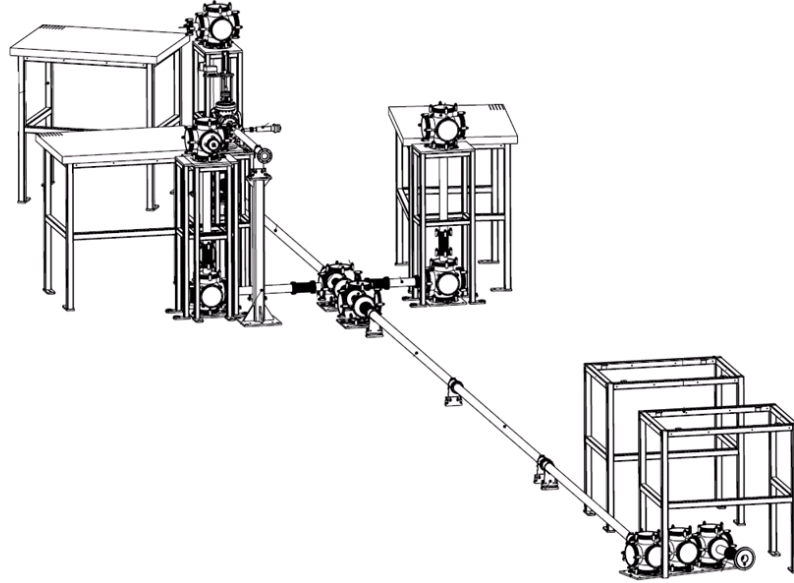


FIGURE 4.2: AEMITR laser beam transport, extending from the existing EO diagnostic in Area 1 to Arc 1 in Area 2

The first requirement was to transport the Ti:S laser beam from the Diagnostics Room to the AEMITR experiment in Area 2. Fortunately this laser was already used for an electro-optical diagnostic experiment in Area 1, so the only additional beam transport needed was in order to carry the laser beam from Area 1 to Area 2. A series of vessels was designed to enclose the laser beam and for mounting various optical elements within. This was attached to the existing laser beam transport underneath the electro-optical diagnostic experiment table in Area 1. The purpose of these enclosures was three-fold:

- To provide an evacuated transport line so that the laser beam is not attenuated or disrupted by air currents;
- To provide a clean and reasonably dust-free environment for mirrors and lenses etc.;
- To provide a personnel safety barrier to stop accidental exposure to the laser.

The design of the laser beam transport system is shown in figure 4.2. The laser beam transport system as built extends beyond the AEMITR optical tables as far as the end of the Arc 1 of the accelerator. This is for future experimental use.

In order to position all the vessels concentrically on a reference line, a HeNe laser was set up at the extreme end of the layout, at the end of the first arc of the accelerator, which was then directed to a target set up underneath the electro-optical diagnostic experiment table. The target position was adjusted to give the best compromise within the constraints of various fixed obstacles that lay on the desired path (such as the hole

in the concrete wall dividing Area 1 and Area 2, the legs of various tables) whilst still being compatible with attaching the last new vessel to the existing laser beam transport. Starting at the HeNe laser end, each of the vessels was attached to the floor and adjusted so that the entry and exit faces were centred on the HeNe laser reference line. When this was completed, the existing beam transport to the electro-optical diagnostic was carefully vented, the final connection bellows to the AEMITR section added, and the two vacuum pumps (an existing one on the original section, and a new one located near the AEMITR experiment) turned on. Unfortunately this revealed a large leak in the new system, which required some further dis-assembly and rebuilding before a reasonably vacuum-tight system was achieved. Finally, the pressure recorded at the two vacuum pumps ranged between  $4.0 \times 10^{-3}$  and  $1.4 \times 10^{-4}$  mbar.

Having demonstrated leak-tightness, the system was subsequently vented and all the optical elements required to transport the Ti:S laser beam from underneath the electro-optical diagnostic experiment table to the AEMITR experiment tables were installed. These were aligned using the Ti:S laser beam. Two windowed-flanges are fitted to allow the laser beam to exit the transport line on to the AEMITR table or by the end of the first arc of the accelerator. Figure 4.3 shows part of the completed laser beam transport system, at the point where the incoming laser beam is brought up on to the optical tables in Area 2.

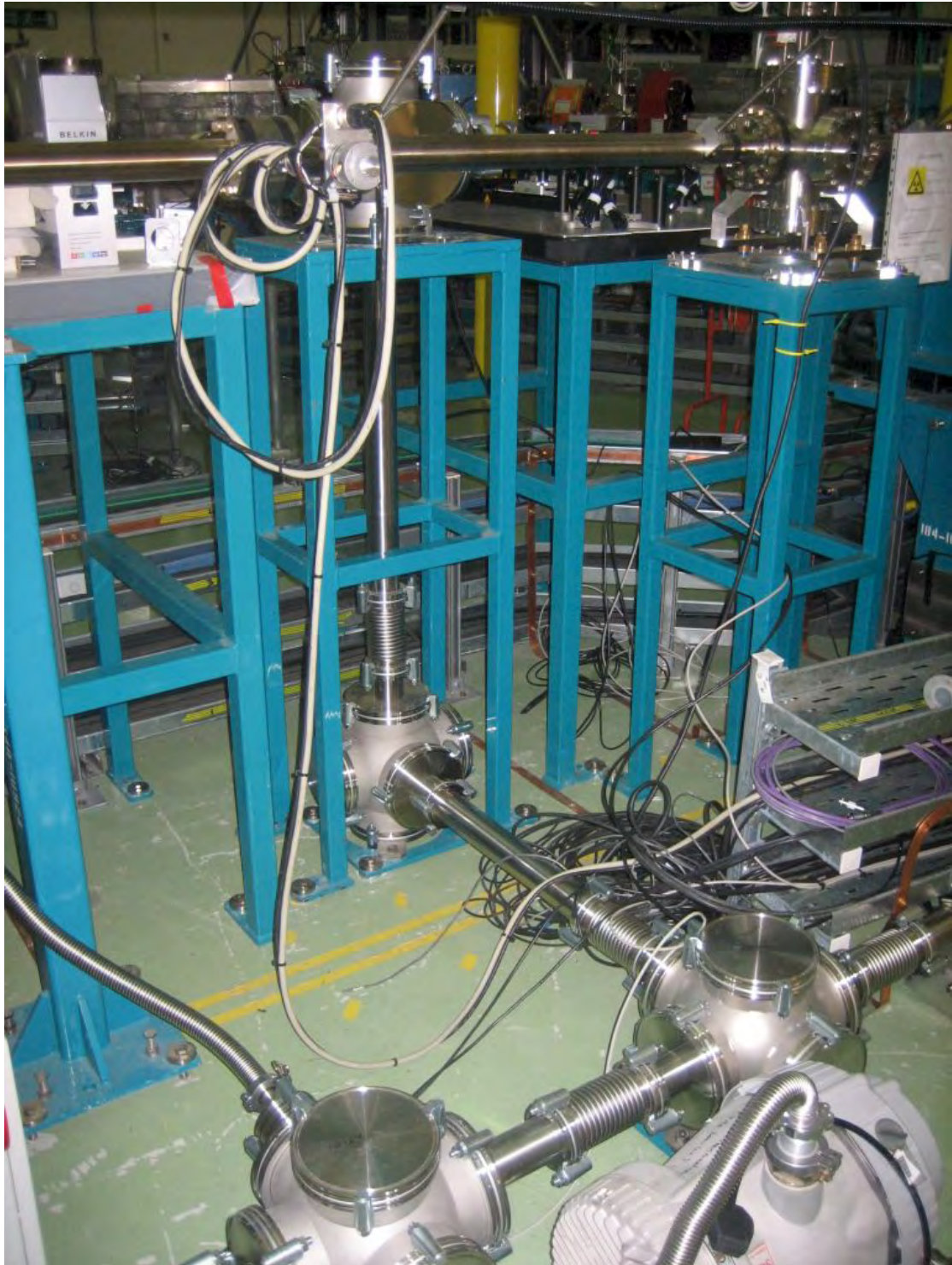


FIGURE 4.3: A section of the completed laser beam transport system, showing part of the vacuum system in the foreground (a roughing pump) and the periscope that transports the laser beam from ground level up to optical table (and therefore electron beam) height



is a composite photograph of the terahertz-generation table during assembly, with some components labelled using the same key as figure 3.1.

After fitting all the optical elements, a Matlab-based control program was developed with the assistance of TT. This was later incorporated in a comprehensive control and data acquisition program by AW.

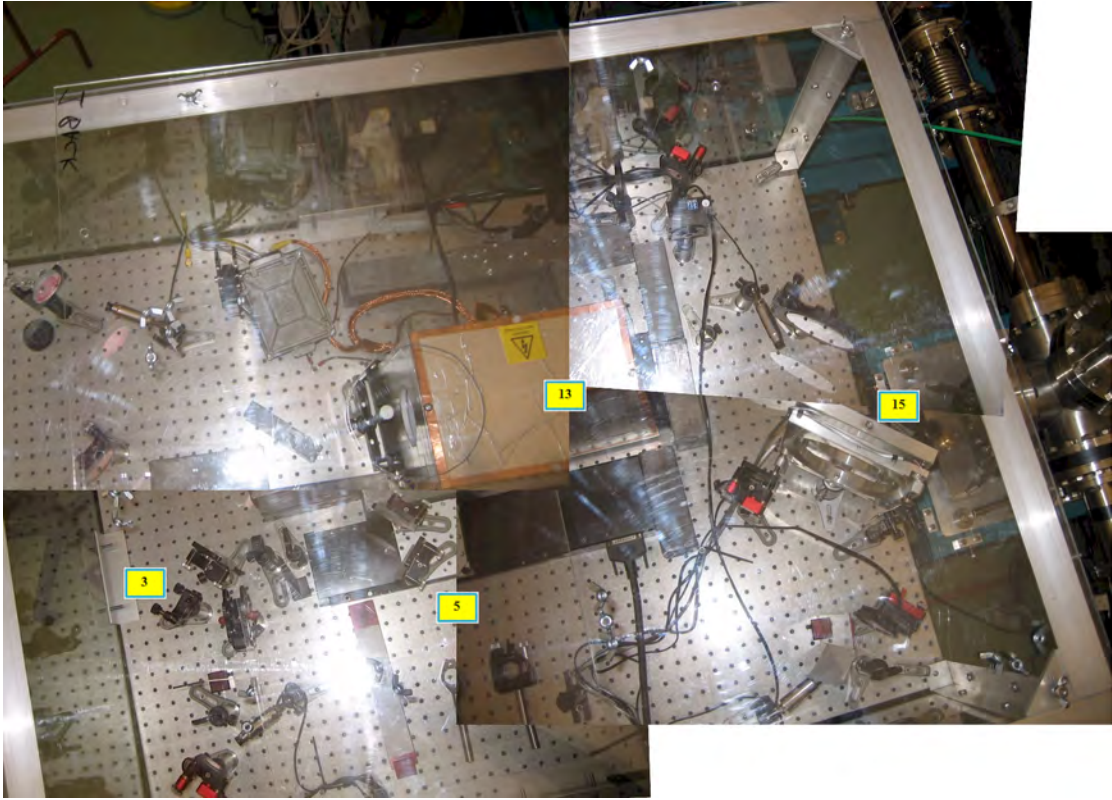


FIGURE 4.5: Composite photograph of optical table 1 (for terahertz generation) inside ALICE Area 2. This should be compared to the left-hand side of figure 4.4

### 4.3 Accelerator modifications for AEMITR

The modifications made to ALICE fall into three categories: hardware required to enable the interaction of the terahertz with the electron beam; components to measure the terahertz electric field intensity at the nominal interaction point, and electron beam diagnostics to help with the set up of the electron beam in the vicinity of the interaction point and detect the effect of any interaction. Figure 4.6 shows the new components for AEMITR (labelled in red) amongst the existing components (labelled in grey) in Straight 2 of ALICE. These are:

- ST2-DIA-OTR-01 is an Optical Transition Radiation (OTR) screen upstream of the AEMITR experiment;
- ST2-LM-MIR-01 is a  $45^\circ$  mirror with a hole in its centre;

- ST2-LM-XTAL-01 is an ZnTe crystal and mirror used to measure the terahertz field strength at the interaction point;
- ST2-LM-YAG-01 is a new Yttrium Aluminium Garnet (YAG) screen and a terahertz-blocking aperture near the interaction point;
- ST2-DIA-OTR-02 is an OTR screen downstream of the AEMITR experiment;
- ST2-DIA-YAG-01 is a new YAG screen in the centre of the bunch compression chicane.

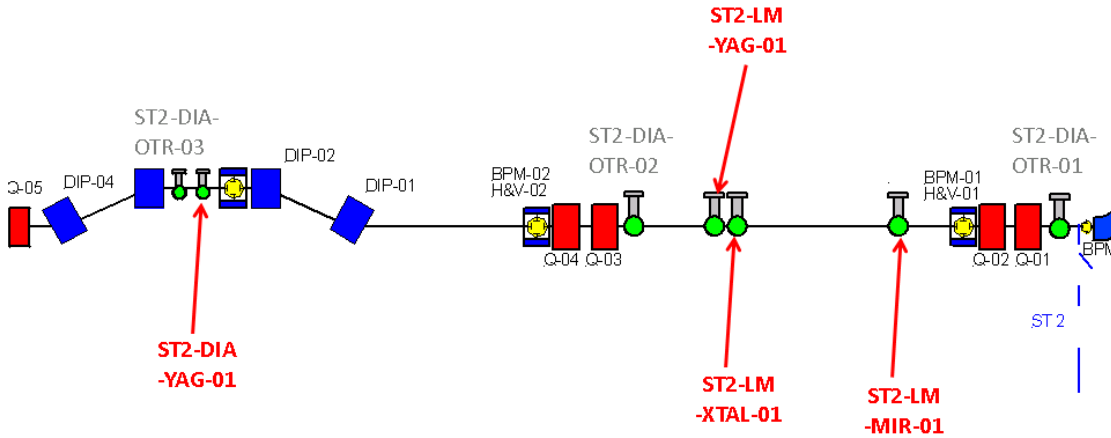


FIGURE 4.6: New accelerator components installed as part of the AEMITR project (labelled in red) amongst the existing components (labelled in grey) in Straight 2 of ALICE

### 4.3.1 Interaction hardware

The requirement was to get the terahertz radiation into the accelerator and co-propagating with the electron beam as far as the interaction point and no further. This was achieved via two new vessels added to the ALICE electron beam transport system; the first has a fused-silica window which is the entry point for both the terahertz and probe laser beams. As this window is perpendicular to the electron beam axis, a mirror aligned at  $45^\circ$  to the electron beam axis can then be pneumatically-driven into the vessel to reflect the terahertz and probe laser beams along the electron beam axis. A 5 mm diameter hole in the centre of the mirror allows the electron beam to continue to propagate unimpeded. When the mirror is withdrawn a cylindrical cage slots into the vessel, to give the appearance of a smooth and uninterrupted vacuum vessel from the perspective of the electrons.

A second new vessel was added at the interaction point which includes a YAG screen to measure the electron position (via a video camera and Matlab image capture software, integrated into ALICE's existing diagnostics system) and a plate perpendicular to the electron beam with a 10 mm diameter hole which is designed to block the terahertz

beam (by diffraction) while the electron beam passes through the hole. The assembly is completed by another cylindrical cage that is in place when ALICE is being run normally. The assembly (called ST2-LM-YAG-01) is shown in figure 4.7, and is driven in and out by a stepper motor (under the control of ALICE’s control system) so that the aperture position can be fine-controlled.

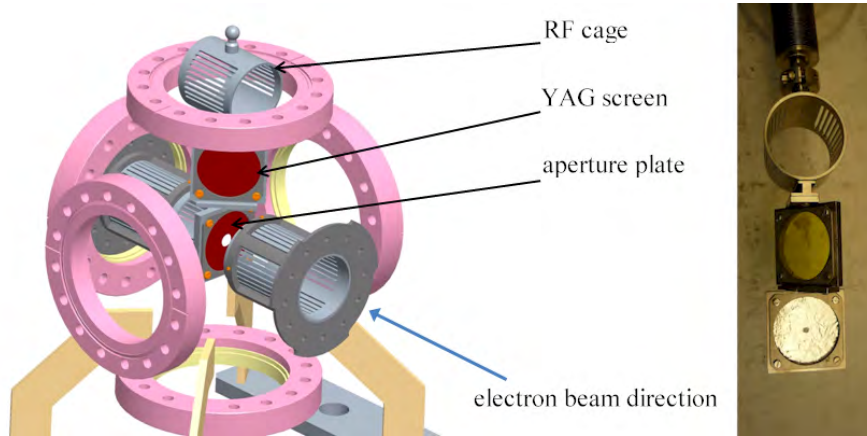


FIGURE 4.7: ST2-LM-YAG-01 assembly, showing the aperture plate, YAG screen and RF cage which, during normal operation of ALICE, is positioned to give the appearance of a smooth and uninterrupted vacuum vessel from the perspective of the electrons

### 4.3.2 Terahertz electric field strength measurement

A ZnTe crystal ( $10 \times 15 \times 0.2$  mm) in  $\langle 110 \rangle$  orientation (so that it is sensitive to transverse electric field) and a mirror are both mounted inside the accelerator on the same stage, close to the nominal interaction point. There is also a small window and camera to allow the alignment of the probe laser on the ZnTe crystal to be seen. This assembly is identical to that previously incorporated in ALICE immediately prior to the FEL, which is used in the electro-optic bunch length diagnostic. In our case we used it to measure the intensity of the electric field of the terahertz pulse at the interaction point. The movement stage has sufficient travel to place the ZnTe crystal into the centre of the vacuum pipe of the accelerator (but only when there is no electron beam) where the terahertz pulse will be coming to a focus. A probe laser beam then passes through the ZnTe crystal, after which it falls on the mirror which is at  $45^\circ$  to the beam axis, and then leaves the accelerator through another small window onto the detector table. Figure 4.8 shows this arrangement.

### 4.3.3 Additional electron beam diagnostics

In order to detect the predicted energy modulation it was necessary to look at the transverse beam size at a point in the accelerator where the value of dispersion is sufficiently large for its contribution to beam size to dominate over that from the emittance. All the existing screens in ALICE after the linac are OTR foil screens, which require long trains (of the order of microseconds) in order to generate sufficient light for the camera

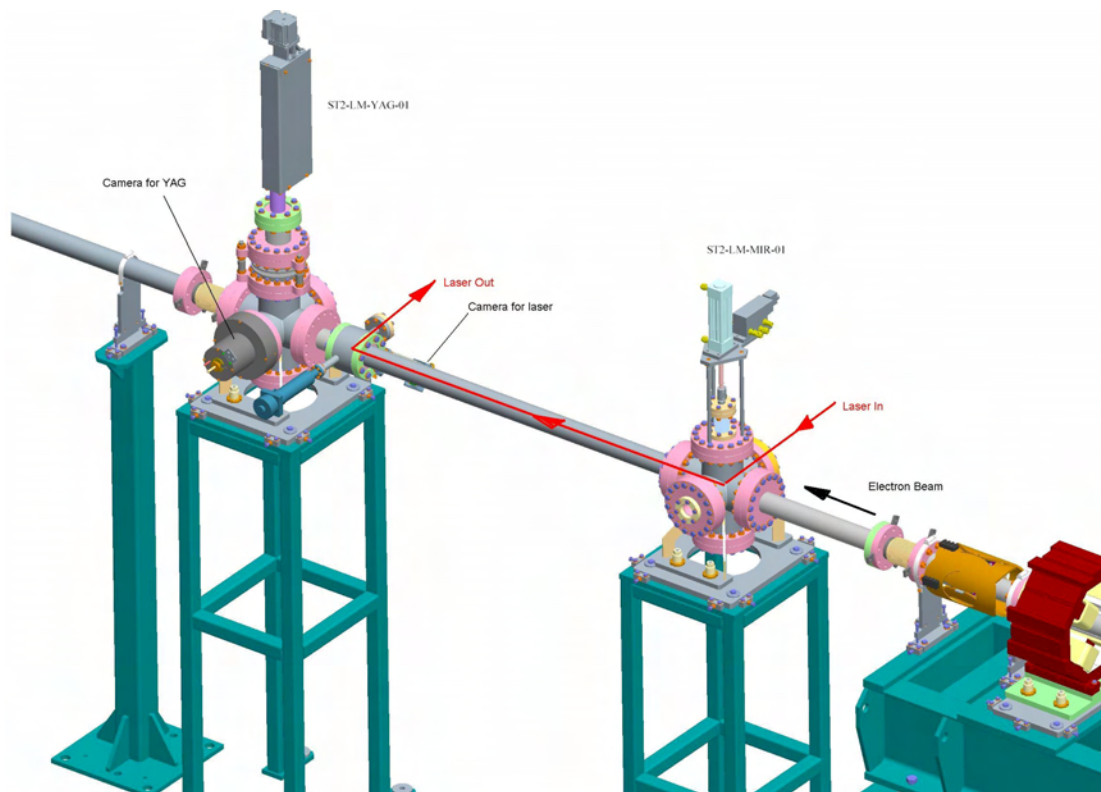


FIGURE 4.8: New AEMITR accelerator components being used for measurement of terahertz field strength in Straight 2 of ALICE

to record anything. As the AEMITR experiment operates at 10 Hz with single bunches of electrons, it was necessary to use a YAG screen which is sensitive enough to give a signal with a single, low-charge bunch. Thus a new screen was required and the centre of the bunch compression chicane was selected as there is both significant dispersion here and a suitable flange on which to mount the pneumatically-driven screen.

The new chicane YAG is upstream of the existing chicane OTR screen and is called ST2-DIA-YAG-01. The standard ALICE camera that records the radiation from the OTR has neither the depth of field to focus on the YAG, nor sufficient resolution to record the change in size of the small beam spot we required. Therefore for each AEMITR experimental run, the standard camera had to be removed and replaced with another Pixelfly camera. As this sensitive and expensive camera needed to be protected from the high radiation levels at beam height (a combination of bremsstrahlung from beam loss colliding with accelerator components and radiation originating from multipactor in the linac cavity) this camera was mounted approximately 40 cm below beam height behind a lead brick wall. It was then necessary to mount a mirror and an additional lens (focal length 300 mm) between the camera and the viewport through which the YAG screen could be viewed. Careful alignment of these three components, plus adjustment of the zoom and focus controls on the lens mounted on the camera allowed a focussed image of the whole screen to fill the camera's field of view. It was necessary to illuminate the YAG screen with some light to do this; either via the terahertz beamline or the vacuum

vessel of the third dipole in the first arc. The size of the YAG screen is known, so that when it fills the camera's FOV the image size could be calibrated. Figure 4.9 is an image of this YAG screen, whilst it is illuminated by light scattered down Straight 2, prior to zooming in fully.

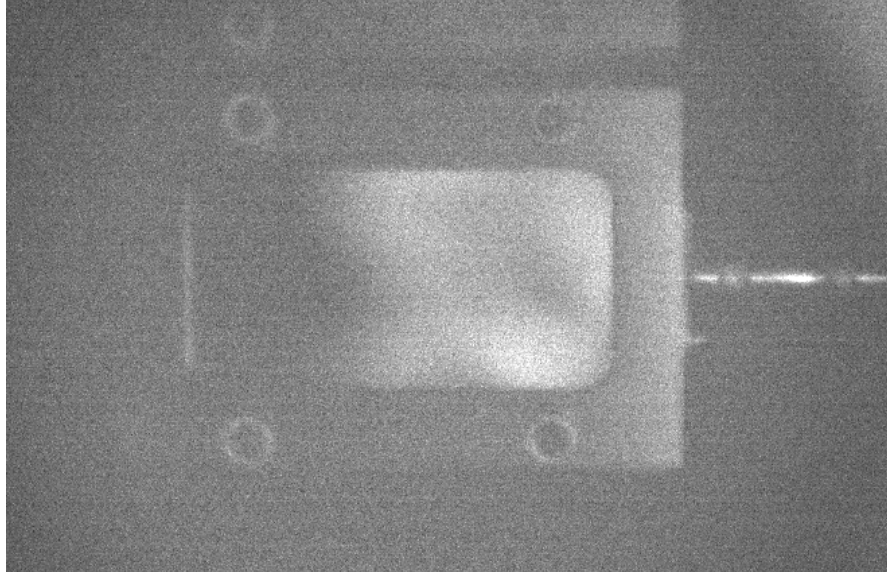


FIGURE 4.9: ST2-DIA-YAG-01, illuminated by light scattered down Straight 2 of ALICE

#### 4.3.4 Electron beam - laser synchronization

It was of course necessary that the electron beam and the terahertz pulse passed through the interaction region simultaneously. The laser oscillator is locked to the RF master oscillator signal in the Laser Room; this ensures that there should be no drift of the relative timing of the accelerator and the laser system. The laser pump beam, which was used to generate the terahertz at the antenna, passes back and forth along an optical delay line which has a total travel of 200 mm. This means the light path can be adjusted by 400 mm, in steps of 0.02 mm. This is a total time of 1.3 ns, adjustable in steps of 0.07 ps. Although ALICE's RF system operates at 1.3 GHz, the photoinjector laser operates at 1/16 of this frequency, 81.25 MHz, so in a multibunch train the electron bunches are separated by 12.3 ns. Prior to compression in the bunch compressor, if the bunchlength is about 2 mm (FWHM) (this is dependent on machine tuning and bunch charge) then this is equivalent to 6.7 ps (FWHM). Thus the laser pump beam optical delay stage has enough travel and resolution to scan the relative timing of the terahertz pulse and the electron bunch to go through from no overlap, to perfect coincidence, to no overlap again. However, it was still necessary to be able to measure and then adjust the relative arrival time of the electron and terahertz bunches at the interaction point. The adjustment of the timing was done with a Coherent Synchrolock-AP system, which shifts the laser oscillator phase relative to the RF master oscillator signal. The measurement was undertaken in Straight 2, at ST2-DIA-OTR-02, which is the OTR

screen downstream of the AEMITR interaction point. The camera that looks at this screen was removed and replaced with a fast photodiode connected to an oscilloscope. One button of a Beam Position Monitor (BPM) located a short distance after this screen (ST2-DIA-BPM-02) was also connected to the oscilloscope. Figure 4.10 shows the experimental arrangement. With the mirror that turns the terahertz beam through  $90^\circ$  (ST2-LM-MIR-01) inserted into the beam pipe, the probe laser beam will travel along the same path as the terahertz pulse and then strike the OTR screen, which will reflect it out of the accelerator onto the photodiode. Simultaneously, the electron beam can pass through the hole in the centre of the mirror, pass through the OTR screen (with some losses) and past the BPM, producing a signal on the 'scope. From measurement of the length of the two different paths taken by the electrons and the light, plus the lengths of the cables connecting the photodiode and BPM button to the 'scope, it was possible to estimate the difference in the time of arrival of the terahertz pulse and the electron bunch in Straight 2.

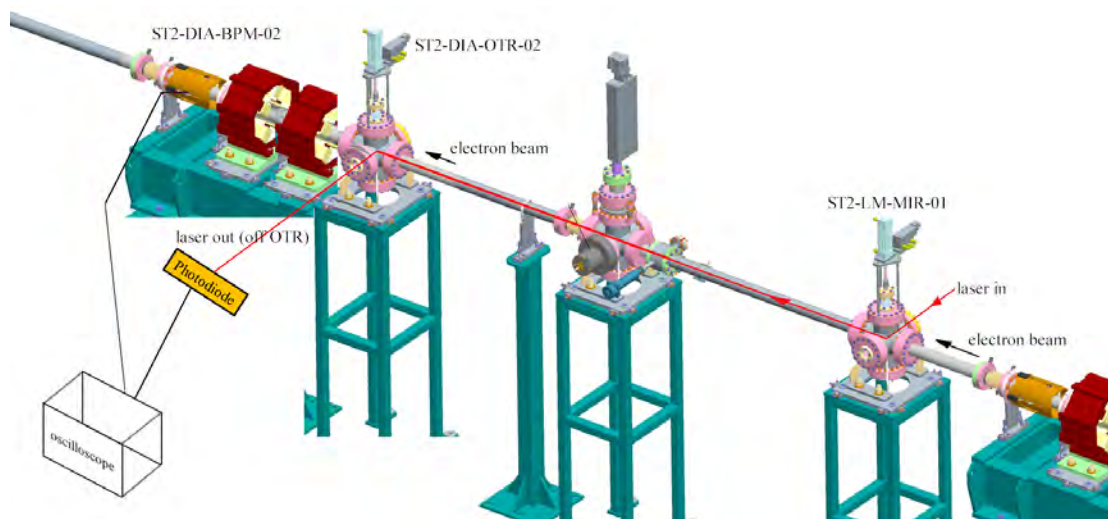


FIGURE 4.10: Laser-electron timing synchronization in Straight 2 of ALICE, using the photodiode signal produced by the probe laser being scattered off an OTR foil and the signal from a single BPM button produced by the electrons

#### 4.4 Alignment of new components and establishment of the experimental axis

In order to ensure the maximum interaction between the electron beam and the terahertz they must co-propagate along the same axis inside the accelerator; in addition there are two apertures through which the electron beam must pass. It is clear therefore that a reasonably precise physical alignment of the various devices involved is necessary in order to establish a reliable experimental axis. As the maximum electron beam diameter is of the order of a few millimetres (rms) in this straight and the terahertz radiation

beam will also be of the same scale, alignment to under a millimetre error should be adequate.

<i>ST2-LM-MIR-01</i>				
BEGIN	Y	-0.3347	Z	0.6275
CENTER	Y	0.2222	Z	0.5934
END	Y	0.7792	Z	0.5593
<i>ST2-LM-YAG-01</i>				
BEGIN	Y	1.5968	Z	-4.1577
CENTER	Y	0.9917	Z	-4.2121
END	Y	0.3866	Z	-4.2665

TABLE 4.1: Initial vessel survey positions before re-alignment

When the two new vessels including ST2-LM-MIR-01 and ST2-LM-YAG-01 were installed they were apparently not surveyed in position. Table 4.1 records the positions of the upstream (BEGIN), centre (CENTER) and downstream (END) faces of two of the vessels (in mm), before the alignment procedure described here, as measured by a Faro laser-tracker system; where Y is the horizontal and Z is the vertical axis of the beamline. It can clearly be seen that there was significant misalignment present before this exercise was undertaken. In any case it is the alignment of the apertures of their internal components that was most critical to the success of this experiment and because of potential differences between the internal mechanism centre and external structure centre, there was no guarantee that we could have achieved the alignment we needed by traditional means. Therefore it was decided that we would define an experimental axis between the centres of ST2-DIA-OTR-01 and ST2-DIA-OTR-02. The OTR screens in ALICE feature a cross-pattern of small apertures which mark the centre of the screen (figure 4.11 (a)). A HeNe laser was directed down the accelerator from a viewport in the vacuum vessel of the third dipole in the first arc and aligned on the centres of both ST2-DIA-OTR-01 and ST2-DIA-OTR-02 (figure 4.11 (b,c)). The position of ST2-LM-MIR-01 vessel was then moved so that the laser passed through the centre of the hole in the mirror (figure 4.11 (d)). It was not possible to move the ST2-LM-YAG-01 vessel far enough to achieve this with the aperture plate driven to its nominal position by the ALICE control system (125 mm); however if the drive mechanism was forced to drive until it hit its end-stop at about 129.5 mm (for example entering a required position of 130 mm) then sufficient movement of the vessel was available to centre this aperture on the HeNe laser (figure 4.11 (e)). Finally, figure 4.11 (f) shows the the HeNe laser spot on ST2-OTR-02 with both the mirror and aperture plate in; it can be seen that the best compromise that could be achieved required the HeNe alignment beam to be slightly down and to the left. There was no further adjustment available on the vacuum vessels to improve on this further. No survey was done after this exercise.

All that remained was to calibrate the position of ST2-LM-XTAL-01 relative to this experimental axis; it was found that with the drive set at -13 mm the combination of ZnTe crystal and mirror blocked exactly half the HeNe laser beam; i.e. the central edge

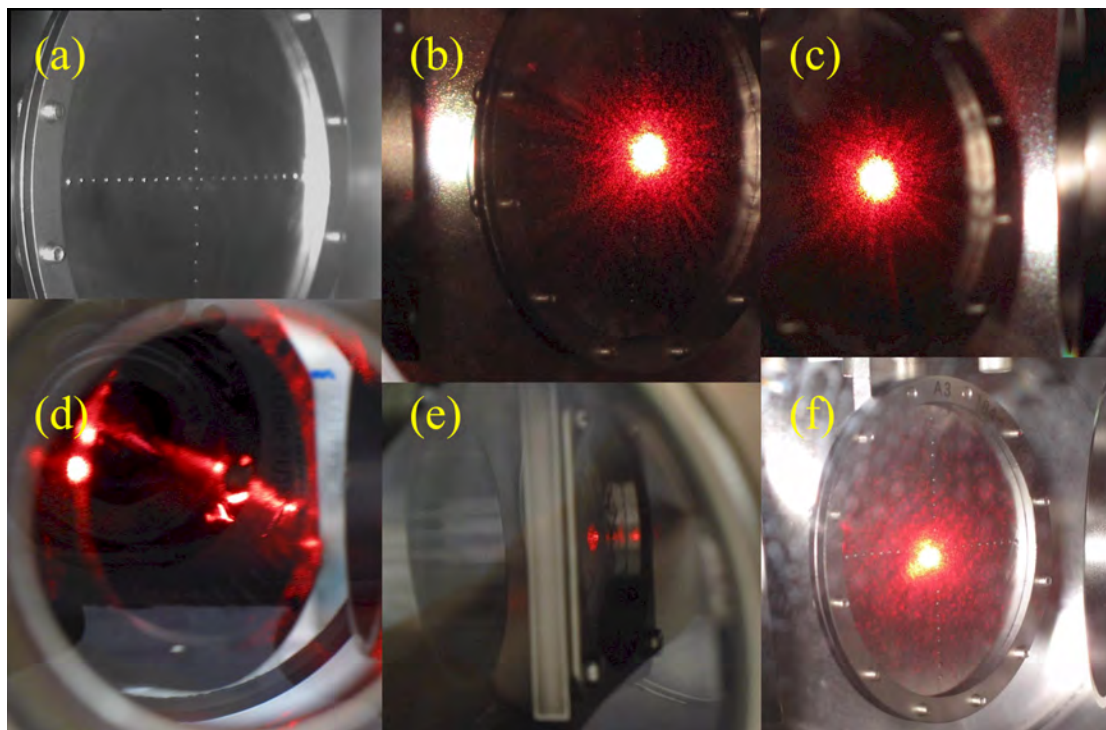


FIGURE 4.11: Alignment of the mirror and aperture plate apertures in Straight 2 of ALICE, using a HeNe laser to establish an axis between the two OTR screens at each end

of the mirror is aligned on the axis transversely. In the vertical direction the crystal and mirror appeared to be slightly low.

## 4.5 Selection of ALICE beam parameters

One of the most important decisions to be made was to choose the optimum ALICE beam parameters such that the signal from any interaction with the terahertz could be most clearly seen. The combination of a photocathode gun with superconducting accelerator cavities enable ALICE to operate over a wide range of beam parameter space; although there is a significant effort required to set up the accelerator properly in each configuration. Thus with the limited amount of machine time allocated to AEMITR experiments and the pattern of each project on ALICE taking turns of a few days at a time, it was important to find a parameter set for ALICE that was not too dissimilar to other operating modes.

### 4.5.1 Beam energy and energy spread

As the effect of the interaction of the terahertz with the electron bunch is an induced energy modulation in the electron bunch; it is clear that energy spread is one of the most important beam parameters. Assuming the normalized emittance and absolute energy spread are independent of the beam energy, then for a particular induced energy

modulation lower beam energy would produce a greater effect that might be easier to detect. Also at our observation point higher beam energy reduces the change in transverse position of a particle in the bunch, which would make observation of the effects of an energy change more difficult. Conversely, higher beam energy produces a lower geometric emittance and relative energy spread, which reduces the rms transverse beam size, which would help with the observation of the effects of energy modulation.

For beam energy  $E_0$  and dispersion  $\eta_x$ , the change in transverse position of a particle resulting from an energy change  $\Delta E$  is:

$$\Delta x = \frac{\Delta E}{E_0} \eta_x. \quad (4.1)$$

With a beta function of  $\beta_x$ , a normalized emittance of  $\gamma\varepsilon_x$ , and an rms (absolute) energy spread  $\sigma_E$ , the rms horizontal beam size is:

$$\sigma_x = \sqrt{\frac{mc^2}{E_0} \beta_x \gamma \varepsilon_x + \frac{\sigma_E^2 \eta_x^2}{E_0^2}}. \quad (4.2)$$

The effects of the energy modulation will be made most clearly visible by maximizing the ratio  $\Delta x/\sigma_x$ . Figure 4.12 (AW) shows this ratio as a function of beam energy  $E_0$ , for a number of different values of normalized emittance (from 10  $\mu\text{m}$  to 30  $\mu\text{m}$  in 5  $\mu\text{m}$  intervals) and with the fixed values of other relevant parameters shown in table 4.2. The effect of an energy modulation should be more clearly visible at lower beam energies; however it can be seen that the scaling with energy is not very strong.

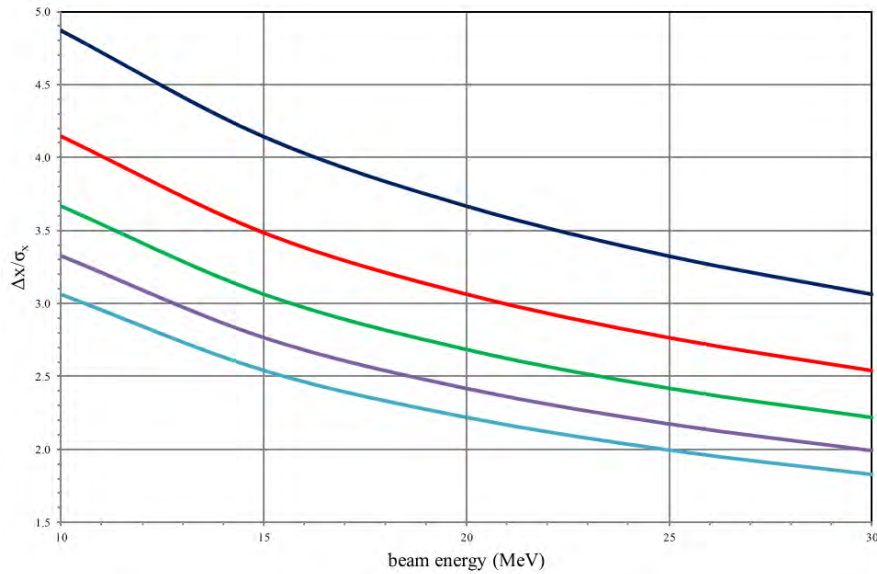


FIGURE 4.12: Transverse particle displacement resulting from a 100 keV change in absolute energy, relative to rms beam size, for a range of beam energies and for normalized emittance from 10  $\mu\text{m}$  (dark blue) to 30  $\mu\text{m}$  (light blue) in 5  $\mu\text{m}$  intervals

Achieving a low energy spread is also an important consideration in the choice of beam energy. Typical full energy operation of ALICE during the period of the AEMITR

$\sigma_E$	10	keV	rms
$\beta_x$	1.11†	m	at centre of chicane
$\eta_x$	0.42†	m	at centre of chicane
$\Delta E$	100-200	keV	estimate from modelling

TABLE 4.2: Fixed machine and beam parameters used for beam size and transverse displacement calculation (†using machine optics calculated in section 4.6)

experiments was between 26 and 27 MeV. Operating the linac cavities with significantly reduced gradient to give lower beam energies would require retuning the cavities (due to geometric changes to the cavities as the Lorentz force changes). Therefore lower energies are generally achieved by running the linac RF off-crest; one side-effect of this is that it then becomes difficult to eliminate the induced correlated energy spread (i.e. average energy deviation as a function of longitudinal position within the bunch).

Another side-effect of reducing the energy is to reduce the RF focusing provided by the linac, leading to higher peak beta functions. However, in simulations by AW (see section 4.6) it appeared that reasonable optics could be achieved over a range of beam energies (from below 15 MeV to 30 MeV) and thus this was not a significant factor in the choice of energy.

Considering all these factors, it was decided to perform the AEMITR experiments at a beam energy of 22.5 MeV. This decision was predicated on the assumption that low emittance (closer to 10  $\mu\text{m}$  than 30  $\mu\text{m}$ ) and energy spread would be easier to achieve at this energy than at lower energy. Furthermore, this was sufficiently close to the typical full energy that no retuning of the linac cavities would be required.

Subsequently, a new method of operating ALICE at low energy (12 MeV) was developed for the purpose of injection into EMMA. This is based on using one linac cavity near crest in the usual accelerating mode while the other cavity is operated at trough (i.e. at  $180^\circ$  from crest). Energy spread is minimized by adjusting the phase of the accelerating cavity (typically  $+3^\circ$ ) while the energy is set by adjusting the gradient of the decelerating cavity. Both cavities will still be operating at near enough to their nominal gradient that no retuning is necessary. Future AEMITR periods are likely to experiment with lower beam energy achieved this way.

#### 4.5.2 Bunch charge and bunch length

Better beam quality (particularly emittance and bunch length) can be achieved with smaller bunch charge. Based on existing measurements and simulations of ALICE beam parameters, 2 mm FWHM bunch length should have been achievable with 20 pC bunch charge; to get down to a bunch length of 1 mm FWHM and normalized emittance of 5  $\mu\text{m}$ , it was thought that 1 pC would be necessary. With bunch charges of a few picocoulombs, the beam loading in the linac should be negligible, in which case long trains of bunches can be used after the linac for machine tuning with the OTR screens. Alternatively, with bunch charges of the order of 20 pC, there should be sufficient charge

to operate the OTR screens with shorter bunch trains and without beam-loading effects making meaningful beam size measurements difficult.

If the electron bunch length is longer than the length of the terahertz pulse, then reducing the bunch length would lead to a stronger signal from the interaction, assuming that the interaction can be synchronized so that the terahertz pulse modulates the energy at the centre of the bunch, where the charge density is highest. If the bunch length could be made small compared to the length of the terahertz pulse, then the energy of the entire bunch could be changed, leading to a displacement of the bunch in the dispersive section, rather than just an increase in bunch size.

The best compromise between a desirable short bunch and sufficient charge for the beam diagnostics to work without beam loading problems in the linac was chosen to be 20 pC for the AEMITR experiments.

### 4.5.3 Emittance

In order to detect the energy modulation from the interaction it was necessary to look at the transverse beam size at a point in the accelerator where the value of dispersion is sufficiently large for its contribution to beam size to dominate over that from the emittance. Thus the smaller the emittance the better. The emittance is predominantly a function of how well the ALICE injector (i.e. everything before the linac) is set up. Based on existing measurements and simulations, in the parameter regime chosen here for AEMITR operation, a normalized emittance of less than 10  $\mu\text{m}$  could be expected.

### 4.5.4 Train repetition rate and the number of bunches per train

Although the Ti:S laser that was used to generate the terahertz radiation can operate at 1 kHz, ALICE is typically operated at either 3 Hz (for EMMA injection) or 10 Hz (for all other projects), although 1, 5 and 20 Hz are also possible. To minimize the amount of work required when setting up for AEMITR shifts, it was decided to operate at 10 Hz.

The laser produces only one pulse per cycle, so ALICE was operated in single bunch mode.

### 4.5.5 Beam stability

Train-to-train or even bunch-to-bunch variation of the accelerator parameters determining the beam size was expected to have a significant impact on the ability to discern a clear interaction signal from the background. Informed speculation suggested that within a multibunch train the jitter in the energy spread should be small. However, train-to-train variation (with a single bunch per train) was expected to be significant with no means available to mitigate this except by improving the measuring system. One possible improvement in the measurement system could be the use of gated cameras to

observe two bunches in one train, with only one having interacted with the terahertz pulse; this possibility will be explored in future experiments.

#### 4.5.6 Summary of ALICE electron beam parameters

Table 4.3 shows the ALICE beam parameters chosen for the AEMITR experiment - some of which can be directly set, others that are a function of the set up of the accelerator.

Beam energy	$E$	22.5	MeV	settable value
Energy spread	$\sigma_E$	10	keV	estimate
Bunch charge		20	pC	settable value
Bunch length		2	mm (FWHM)	estimate
Normalized emittance	$\gamma\varepsilon_x$	<10	$\mu\text{m}$	estimate
Geometric emittance	$\varepsilon_x$	<0.2	$\mu\text{m}$	
Train repetition rate		10	Hz	settable value
Bunches per train		1		settable value

TABLE 4.3: ALICE machine settings for AEMITR experiments

## 4.6 ALICE electron optics for AEMITR (AW)

In order to maximize the chance of detecting the interaction of the terahertz pulse with the electron beam, it was desirable to generate a new set of lattice optics for ALICE, which had certain features that would be optimized for the AEMITR experiment. The primary requirement was for a small beam waist at the interaction point, to maximize the spatial overlap of the electron and terahertz beams. In addition, the beta functions were constrained to reasonable values at all points in the lattice (at least before the chicane; after that we were not particularly interested what happened) as is usual in a well behaved lattice optic. When we were looking for interaction of the terahertz pulse with the electron bunch we used a single electron bunch at 10 Hz repetition rate; if the beam was lost after our detection screen this would be an insignificant source of radiation. However, during the setting up of the electron optics, particularly whilst using the OTR screens, long trains (of the order of 10  $\mu\text{s}$ ) were usually required to see a clear beam image. Rather than these longer trains being lost in an uncontrolled way after the chicane, the electron optics model was continued around the second arc and to the beam dump, so that the electrons were lost in a controlled way.

There should also be zero dispersion at the interaction point and maximum dispersion at the detection location in the chicane, in order for the additional energy modulation to be as visible as possible. As there are no quadrupoles in the chicane, it was not possible to change the calculated dispersion at the detection location (as long as the dispersion in Straight 2, upstream of the chicane, is zero, which it should be). However, if the electron optics are poorly tuned, the dispersion at the interaction point (for example) could be non-zero, and the measured dispersion in the chicane will be higher than the theoretical value. Although a larger dispersion appears beneficial in our case as that

the energy spread will make a larger contribution to the beam size, what really matters is the matrix element  $R_{16}$  between the terahertz interaction point and the observation point in the chicane, which is determined solely by the dipole magnets in the chicane. If the dispersion at the interaction point had been zero, the dispersion in the chicane would have dependant on only the  $R_{16}$  between the interaction point and the chicane measurement point.

The starting point for this exercise was the reference ALICE electron optics (ERLP lattice 5.1) and MAD [52] was used to rematch the optics with these constraints in mind. Figure 4.13 (AW) shows a plot of the beta functions  $\beta_x$  and  $\beta_y$  and the dispersion  $\eta_x$  for an example solution for electron optics for the ALICE experiment. The dispersion at the chicane screen was predicted from the model to be about 0.42 metres. As an aid to interpreting this and subsequent Twiss parameter plots, figure 4.14 shows the pertinent components of the ALICE beam transport system as far as just beyond the four-dipole chicane, plotted against position along the electron trajectory. The interaction point, where the terahertz pulse is brought to a focus co-incident with the electron beam, and the position of the new YAG screen, where the effect of this interaction on the electron beam size would be observed, are both labelled.

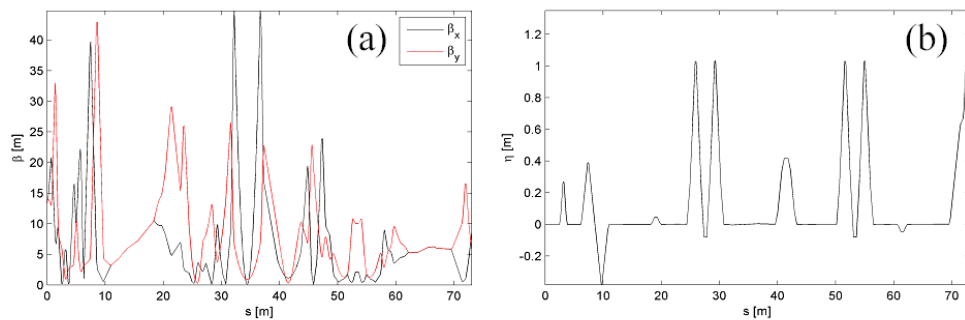


FIGURE 4.13: (a) Beta functions (horizontal - black and vertical - red) and (b) dispersion, for an example electron optics solution for the AEMITR experiment on ALICE

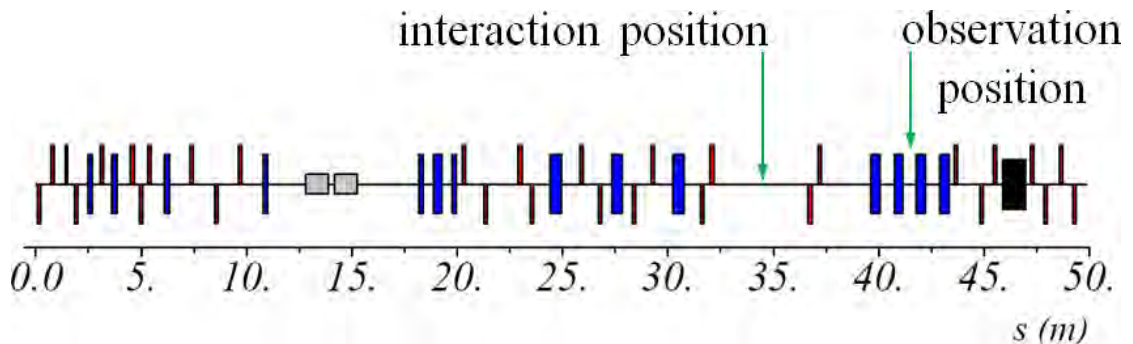


FIGURE 4.14: ALICE beam transport components from the exit of the linac to just beyond the wiggler magnet (black), plotted against position along the electron trajectory. Dipoles are coloured blue, quadrupoles red, and the two linac cavities grey. The interaction point and the position of the new YAG screen, where the effect of this interaction would be observed, are both labelled.

### 4.6.1 Reconciliation of the MAD model with beam measurements

Previous attempts to correlate the actual measured beam sizes (and the inferred Twiss parameters) in ALICE with the MAD model had not proved satisfactory. One of the reasons for this was thought to be poor knowledge of the Twiss parameters of the beam at the exit of the linac. Although detailed models of the injector exist, up to the entrance of the linac, the degree of RF focussing in the linac is not well understood and not well modelled in MAD. As precise control of the electron beam in Straight 2 was particularly important for the success of the AEMITR experiment, an important part of the work was to find a reliable method to set up ALICE repeatably, which meant overcoming the existing limits of understanding of the machine model. This was also particularly important because the AEMITR experimental runs were typically of one or two days duration, interspersed between other projects, so that the initial state in which ALICE was inherited was not exactly the same each time.

It was found that the most reliable way to set up ALICE for AEMITR experiments was first of all to measure the Twiss parameters in Straight 2, using the quadrupole scan method. As explained in the next section, these results could then be used to calculate the Twiss parameters at the exit of the linac, which then become the input parameters to the electron optics model for AEMITR. With this it was then possible to calculate the revised magnet gradients required to get the desired beam parameters at the interaction and detection points. Using the measured properties of each magnet, it is possible to translate magnet currents to magnetic field gradients, and vice-versa.

### 4.6.2 Quadrupole scans in Straight 2

To determine the Twiss parameters at the exit of the linac, the most reliable method was to perform quadrupole scans in Straight 2. A series of beam images are taken at an OTR screen downstream of a quadrupole magnet whose gradient is changed between images. In our case any other quadrupole magnets between the screen and the one being varied were not powered (although there are quadrupole scan methods that could accommodate the more complex scenario but this introduces undesirable complexity and uncertainties). It was often necessary to change the train length during the measurements (so as not to saturate the camera when the spot was tightly focussed and conversely so that there was sufficient intensity when the spot is diffuse) and adjust the steering so the beam spot remained centred at a fixed position on the screen. The images were then analyzed (by fitting Gaussians to the integrated horizontal and vertical intensity) in order to extract the horizontal and vertical beam size ( $\sigma_x$  and  $\sigma_y$ ). By fitting a quadratic to a plot of  $\sigma^2$  vs  $(1 - k_1 L)$  (where  $k_1$  is the quadrupole field gradient and  $L$  is the distance from the quadrupole to the screen) it is possible to extract the emittance and Twiss parameters at the exit of the quadrupole. Figure 4.15 shows a schematic of a Straight 2 with the parameters needed to analyze the quadrupole scan results, while figure 4.16 shows an example of fitting a Gaussian curve to the integrated intensity of a screen image, in both planes.

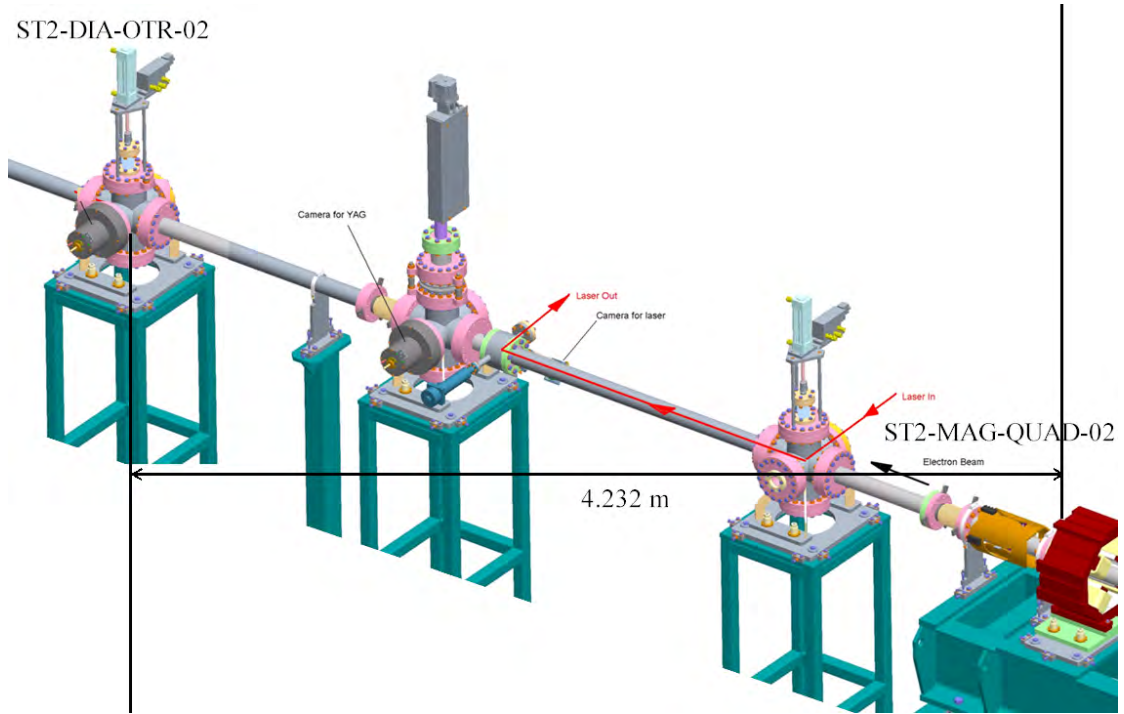


FIGURE 4.15: Layout of Straight 2 of ALICE, with the pertinent devices and dimensions used for quadrupole scans labelled

If in either transverse plane,  $\alpha_Q$ ,  $\beta_Q$  and  $\gamma_Q$  are the Twiss parameters at the exit of the quadrupole magnet being used for the measurements,  $\sigma$  is the rms beamsize (in the corresponding plane) measured at the screen,  $\beta_S$  is the beta function at the screen and  $\varepsilon$  the beam emittance, then:

$$\sigma^2 = \varepsilon\beta_S = \varepsilon[(1 - k_1L)^2\beta_Q - 2(1 - k_1L)L\alpha_Q + L^2\gamma_Q]. \quad (4.3)$$

Thus a quadratic fit to a plot of  $\sigma^2$  against  $(1 - k_1L)$ , in the form:

$$\sigma^2 = A(1 - k_1L)^2 + B(1 - k_1L) + C, \quad (4.4)$$

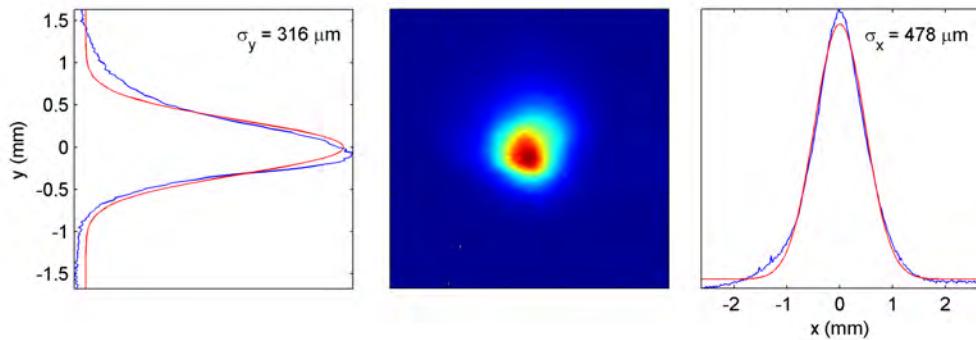


FIGURE 4.16: An example of fitting a Gaussian curve, in both planes, to the integrated intensity of a screen image

has:

$$A = \varepsilon\beta_Q, \quad (4.5)$$

$$B = -2\varepsilon L\alpha_Q, \quad (4.6)$$

$$C = \varepsilon L^2\gamma_Q, \quad (4.7)$$

and because  $\gamma_Q = (1 + \alpha_Q^2)/\beta_Q$ ,

$$\varepsilon = \frac{\sqrt{(4AC - B^2)}}{2L}. \quad (4.8)$$

Figure 4.17 shows an example of fitting a quadratic curve to the data in the horizontal plane, and figure 4.18 shows the equivalent in the vertical plane. Table 4.4 shows the values for the Twiss parameters and emittance derived from this curve fitting example using the method above.

$\alpha_x$	-4.3
$\beta_x$	2.8 m
$\gamma\varepsilon_x$	3.7 $\mu\text{m}$
$\alpha_y$	-1.3
$\beta_y$	0.9 m
$\gamma\varepsilon_y$	3.2 $\mu\text{m}$

TABLE 4.4: An example of the results of the analysis of quadrupole scan data

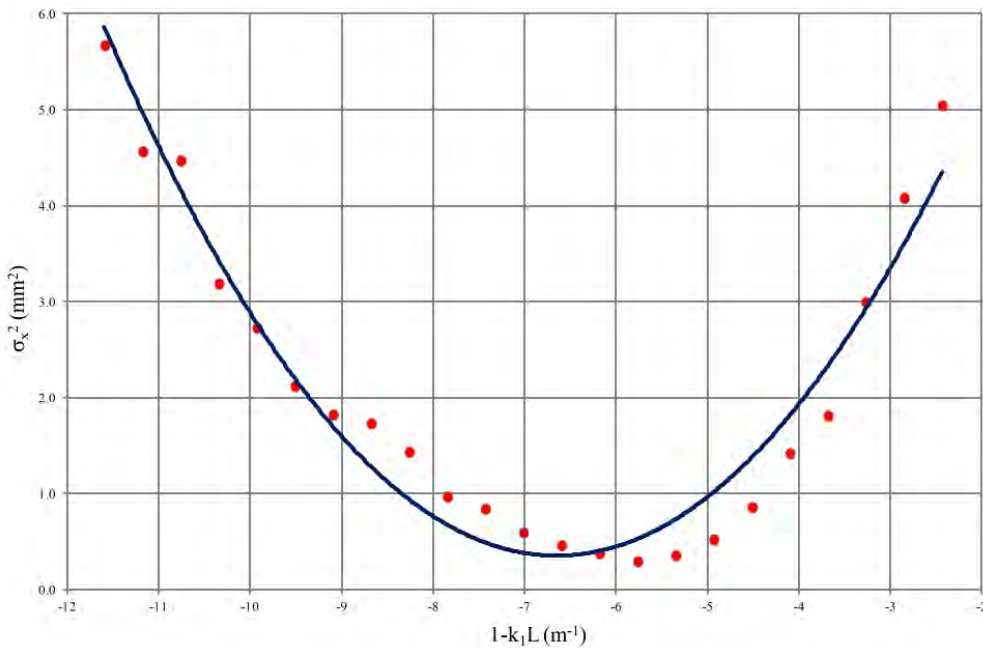


FIGURE 4.17: An example of fitting a quadratic curve to quadrupole scan data in the horizontal plane

The Twiss parameters can then be calculated at the linac exit by treating the section of ALICE between the quadrupole and the linac exit as a beamline and propagating the

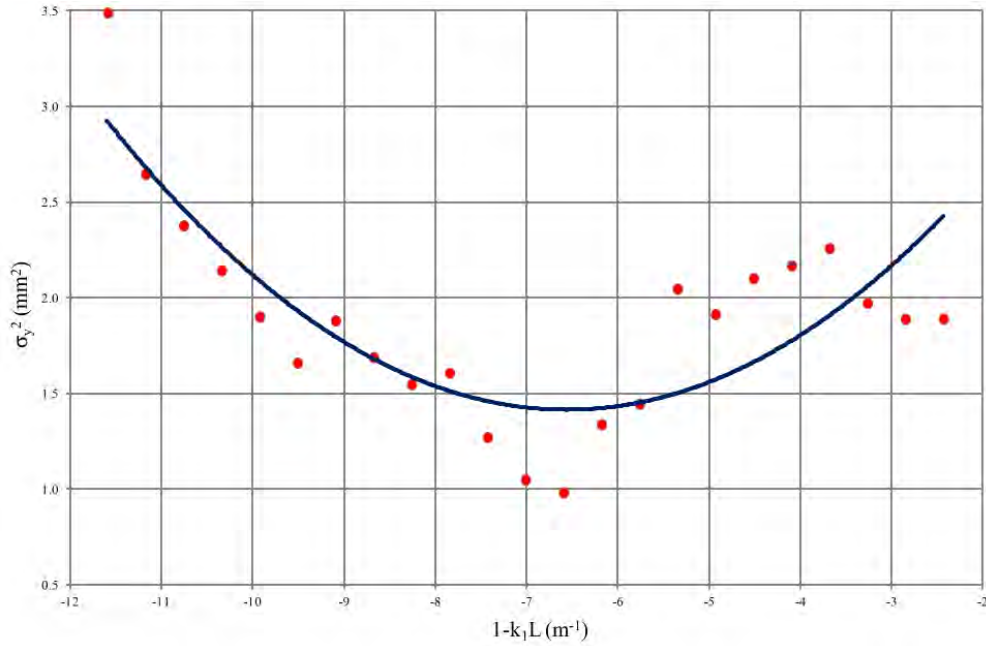


FIGURE 4.18: An example of fitting a quadratic curve to quadrupole scan data in the vertical plane

Twiss parameters in the reverse direction, using a standard accelerator optics code, such as MAD. The Twiss parameters at the exit of the linac then provide the input beam parameters to the matching exercise in MAD that calculates revised gradients for the quadrupoles in order to get the electron optics required for AEMITR in Straight 2. As a cross-check, it is then possible to calculate the beam sizes at every screen in ALICE, and these predictions can be compared to measured results.

Once the revised magnetic field gradients had been calculated and applied to ALICE, measurement of the Twiss parameters via quadrupole scans could be undertaken a second time, in order to check the agreement between the MAD model and the beam size. Taking the beta and alpha functions from the entrance to ST2-MAG-QUAD-02, and propagating forwards through the chicane and backwards to the linac, the images of the beam on the screens in ALICE could be used along with the emittance to check the agreement at specific points around the machine. Figure 4.19 shows an example of this. The horizontal (black) and vertical (red) beta functions (a) and alpha functions (b), along with the dispersion (c) are plotted along with circles representing the values derived from measurements at these points. This shows excellent agreement in Straight 2. Propagating backwards through the arc, we again see good agreement, but then things go wrong after the arc, due to the fringe fields of the arc dipoles not being known with sufficient accuracy. Further investigation revealed that a good agreement could usually be achieved if the fringe field parameters (*fint* and *hgap* in MAD8) of the Arc 1 dipole magnets were used as variables to match the Twiss parameters calculated in MAD to those measured in the accelerator. However, for the purposes of this experiment all that was important was to get the desired Twiss parameters in Straight 2 and it was

found that the additional complication of using the fringe field parameters as a fitting parameter was not necessary.

Furthermore, unless the plot of  $\sigma^2$  vs  $(1 - k_1L)$ , for both horizontal and vertical directions, passes through a clear minimum within the range of quadrupole gradients used, quite large errors can be introduced into the process. This was the case with AEMITR optics and it was found that doing further Straight 2 quadrupole scans after establishment of AEMITR optics was not useful. In any case, once the revised magnet gradients had been applied, small manual adjustments to focussing could be made to finalize the set up.

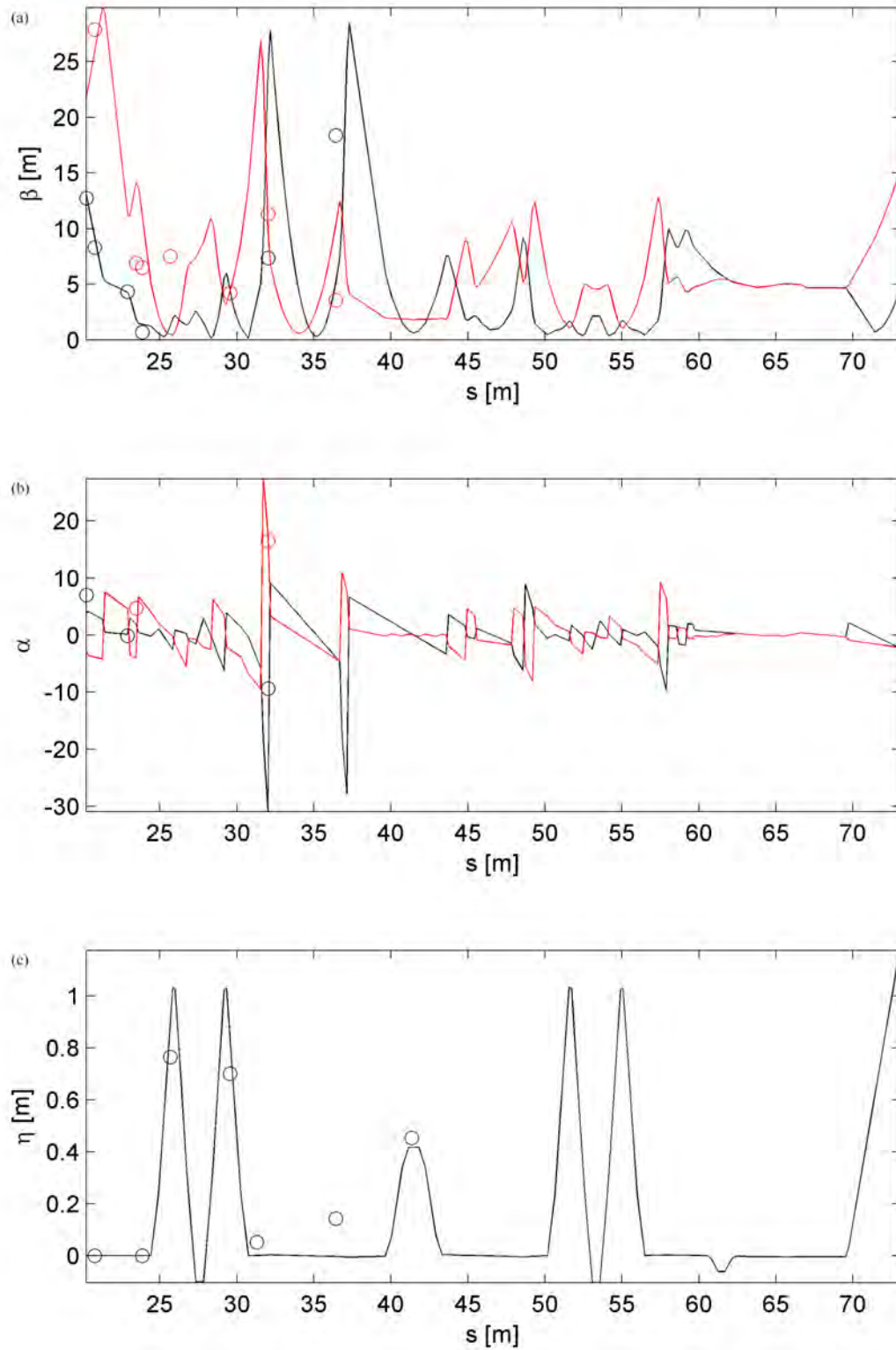


FIGURE 4.19: A comparison of Twiss parameters derived from screen measurements (circles) with the calculated values from the electron optics model. (a) and (b) are the beta and alpha functions respectively (horizontal is black and vertical is red), while (c) is the dispersion

### 4.6.3 Dispersion measurements

The other beam parameter that can be measured relatively easily to compare the virtual model with reality is the dispersion. Furthermore, in order to detect the energy modulation induced in the electron bunch, we were looking for an increase in the beam size at the detection screen. In order to quantify the increase in beam size that is due to energy modulation, we need to know the dispersion value at this point. This was measured by recording a series of images of the beam spot on the YAG screen at the detection location as the energy of the beam was changed by changing the linac gradient. From our calibration of the camera image of the screen it was possible to record the position of the centroid of the spot as a function of linac gradient. The beam energy must also be calibrated as a function of linac gradient.

If a particle (this example refers to the horizontal plane, but it could be either transverse plane) moves a distance  $\Delta x$  as result of a fractional change in its energy of  $\Delta E/E$ , then the dispersion  $\eta_x$  is defined as:

$$\eta_x = \frac{\Delta x}{\Delta E/E}. \quad (4.9)$$

To measure the position of the beam spot on the chicane YAG as a function of energy, a series of images (although a bare minimum of two is sufficient) was recorded at different linac gradients. The images were then analyzed (by fitting Gaussians to the integrated horizontal and vertical intensity) in order to extract the horizontal and vertical beam centroid positions. The chicane YAG screen images were calibrated with knowledge of the dimensions of the screen holder from the engineering drawing. The beam energy as a function of linac gradient was measured at the first dipole magnet of Arc 1, where the change in magnet current required to keep the beam spot at the same place on a downstream screen (AR1-OTR-01) was recorded as the linac gradient was changed. These data could then be used in conjunction with the known magnet characteristics to calculate the beam energy change as a function of linac gradient. The nominal dispersion at the entrance to this magnet should be zero (this can be checked by observing the screens in Straight 1 before this dipole as the beam energy is changed) and all magnets between the dipole and the screen (in this case there is only a sextupole which was not energized in the AEMITR set up) should be off.

### 4.6.4 Tomography measurements in the ALICE-to-EMMA injection line

The third possible test of our calculation of the Twiss parameters at the linac exit was to use the ALICE-to-EMMA injection line. This includes a phase space tomography diagnostic section that can be used to measure the phase space distribution of the beam [53]. Although only designed to operate at the maximum injection energy of EMMA of 20 MeV, its design was modified by the author to operate up to the maximum design

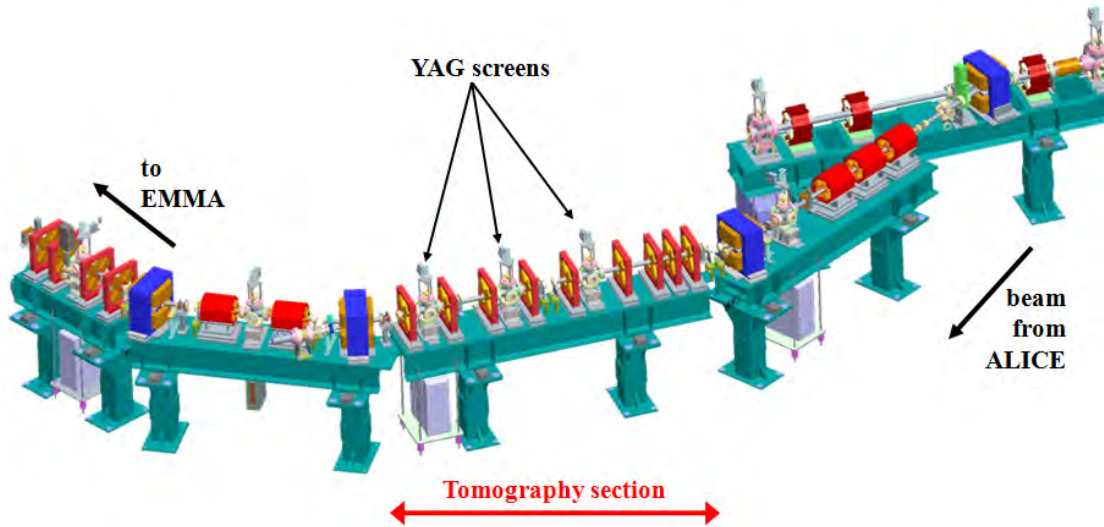


FIGURE 4.20: The layout of the ALICE-to-EMMA injection line, including the tomography diagnostic section

energy of ALICE, 35 MeV [54]. Figure 4.20 shows the layout of the ALICE-to-EMMA injection line and identifies the tomography diagnostic section.

As part of the process of setting up for phase space tomography it is necessary to match the Twiss parameters at the linac exit very precisely to specific values at the start of the tomography diagnostic section. Thus it is also a useful tool to confirm that the Twiss parameters at the linac exit determined by quadrupole scans are correct. MAD can be used to calculate the quadrupole strengths required to transport the beam from the linac to the tomography diagnostic section. Once these magnet settings are implemented, three identical well-focussed circular beam images should be visible on the three screens in the tomography diagnostic. If not, then the initial Twiss parameters (i.e. those at the exit of the linac) are incorrect. The requirement to get three identical well-focussed circular beam images makes this a very sensitive check as to whether we have correctly calculated the Twiss parameters at the linac exit.

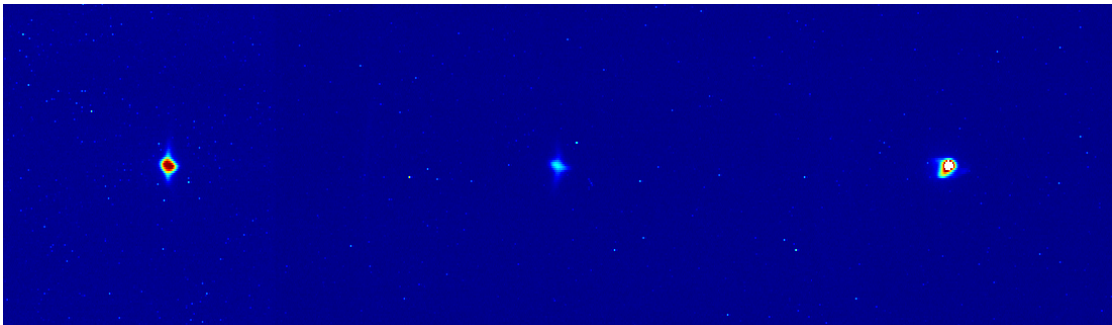


FIGURE 4.21: Beam images from the three consecutive screens of the tomography section of the ALICE-to-EMMA injection line, with ALICE set up for AEMITR (the camera observing the middle screen of these three has been fitted with a filter to eliminate saturation)

Figure 4.21 shows an example of the images from the three consecutive screens of the tomography section of the ALICE-to-EMMA injection line, after using MAD to match the Twiss parameters calculated at the exit of the linac to the start of the tomography section. An additional small adjustment to the current in the final two quadrupoles in ALICE was also made. Each of these images were recorded with a single bunch of electrons and the AEMITR set-up of ALICE. Note that the camera observing the middle screen of these three has been fitted with a filter to eliminate saturation.

## 4.7 Chapter summary

This chapter has listed the work done to the ALICE accelerator, both in terms of hardware changes and the establishment of new operating regimes, required for the experiment to be a measurable success. In addition to the construction of a duplicate terahertz-generation assembly, part of which was within the ALICE vacuum envelope, various additional pieces of hardware were added to ALICE to allow the terahertz to enter the accelerator and co-propagate with the electron beam, and to make any interaction detectable. An reduced-energy operating regime was also identified for ALICE, to give the best chance of an interaction being measured.

## Chapter 5

# Measurements in the ALICE Accelerator Hall

### 5.1 Introduction

This chapter records the experimental work done with the ALICE accelerator. The final chapter will analyse what was achieved and what might be possible in the future.

The work recorded in this chapter was in three major areas:

1. Measurement of the strength of the electric field of the terahertz pulses generated in the accelerator hall (as opposed to the Diagnostics Room where the initial measurements were made);
2. Setting up and measurement of the ALICE beam parameters which had been optimized for this experiment;
3. Experiments aimed at detecting an interaction between the terahertz pulses and the electron bunches.

### 5.2 Terahertz field strengths using the ZnTe crystal integrated into ALICE

Just as the electro-optic effect was used in the Diagnostics Room to measure the strength of the electric field in the pulses of terahertz that were produced there, an identical experimental set-up was built in Area 2, as described in Chapter 4. The ZnTe crystal is located within the ALICE accelerator vacuum envelope, and located very near the point of intended interaction between the electron beam and the terahertz pulses. Otherwise the experiment was operated in the same way, with the goal of measuring the terahertz electric field very near the point of eventual interaction with the electron beam.

### 5.2.1 Initial measurements

The average power of the Ti:S laser in the Diagnostics Room was measured at about 0.45 W; by the time this had been transported as far as the electro-optic diagnostic experiment in Area 1 it had reduced to 0.16 W on the optical table and at the AEMITR experiment in Area 2 it was measured to be 0.14 W.

Following any re-alignment of the optics of the pump or probe beams (this includes re-alignment before the beamsplitter as this will also affect the paths followed after the beamsplitter) it was necessary to find the position of the optical delay line translation stage that corresponded to temporal overlap of the probe beam with the terahertz pulse at the ZnTe crystal in the accelerator. Thus the layout of the optics on the table had to be such that this was within the range of movement of the translation stage that moves the two mirrors of the optical delay line. Before generation of the terahertz was set up, it was possible to confirm this was the case by combining the probe and pump beams (with no antenna present) at the phase-matching angle in a non-linear crystal (beta barium borate) before they entered the accelerator. This produced an on-axis second harmonic signal when the pulses overlapped in time and thus the translation stage position for equal pathlengths for the probe and pump beams could be measured. The result was that maximum temporal overlap occurred at translation stage position of 11.8 mm.

In order to maximize the peak terahertz field strength it is necessary to maximize the temporal compression of the laser beam. This is done in the Laser Room by adjusting the motor-driven mirrors of the compressor. Breaking into the optical path between the Laser Room and the AEMITR optical table in Area 2 would have risked disturbing the alignment of the beam. Therefore this was done remotely by using the trigger signal cable (that goes between the Diagnostics Room and the AEMITR experiment) to connect the motor controller in Area 2 to the compressor in the Laser Room. At a laser repetition rate of 10 Hz, the laser compression was optimized by placing a focussing lens in the beam path and then maximizing the sound generated at the focus. At higher laser repetition rates ionization of the air at the focus could be used.

First images of the probe beam illuminating the ZnTe crystal without the crossed-polarizer in front of the camera (after adding several orders of magnitude filtering to attenuate the beam power) had significant structure that we could not eliminate by optical adjustment. This can be seen in figure 5.1 and was not expected - the probe laser beam should provide uniform illumination of the ZnTe crystal, and the crystal itself should not exhibit any significant structure.

Despite this, an initial attempt was made to generate and detect terahertz around the optical delay line translation stage position previously determined to correspond to temporal overlap. As it proved difficult to find a combination of quarter-wave plate and crossed-polarizer position that almost entirely extinguishes the probe laser at the camera, it was not surprising that no clear terahertz signal could be extracted from the images. Figure 5.2 is an example of one of the images recorded at this point. It was also

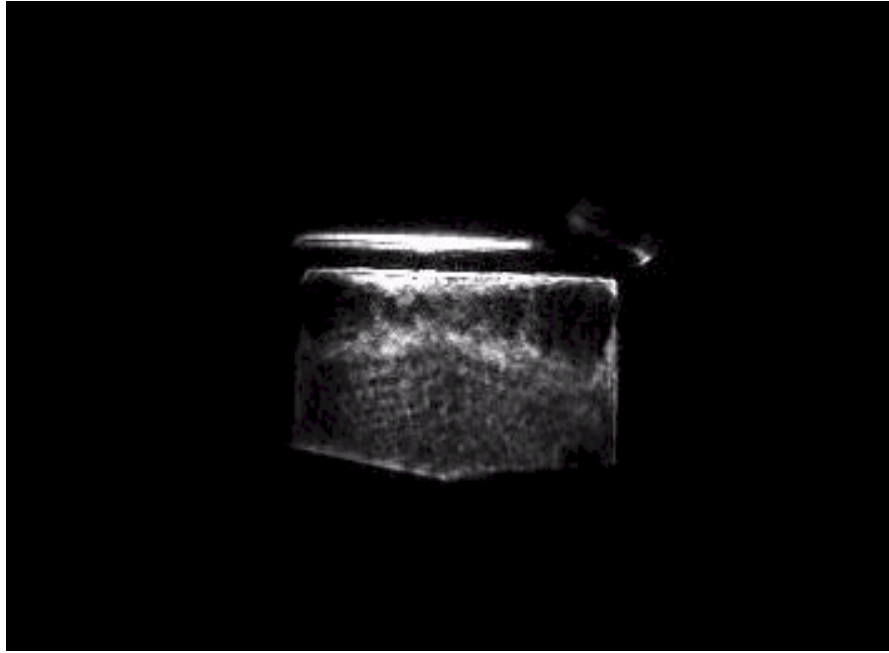


FIGURE 5.1: First image of the probe beam illuminating the ZnTe crystal inside ALICE

noted that the laser position on the optical table appeared to have drifted during the experiment, thus re-alignment would be required before the next measurements.

The measurement of terahertz electric field strength using the ZnTe crystal and camera technique relies on being able to find a combination of quarter-wave plate and crossed-polarizer position that almost entirely extinguishes the probe laser at the camera. This was relatively straightforward to achieve in the Diagnostics Room, but proved

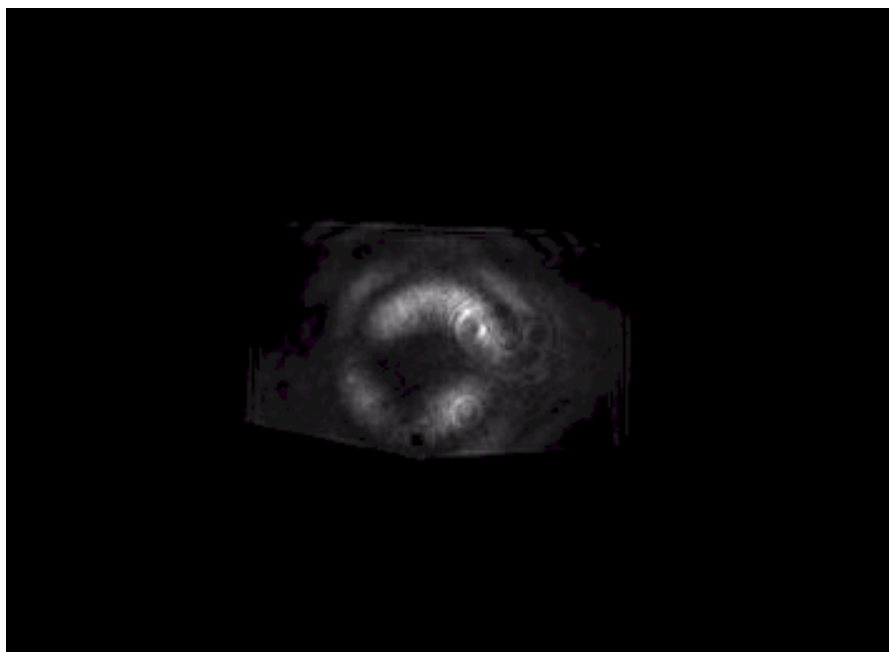


FIGURE 5.2: Image of the ZnTe crystal during the first attempt to generate and detect terahertz inside the accelerator

impossible with the optical arrangement in the accelerator hall. This implied that the level of polarization of the probe beam was not as good as it should have been. Therefore it was decided to determine where in the system the loss of polarization was occurring.

### 5.2.2 Investigation into the degree of polarization

The previous attempt to detect temporal and spatial overlap of the terahertz and probe laser was very inconclusive because it was very difficult to find a combination of quarter-wave plate and crossed-polarizer angle that almost entirely extinguished the probe laser at the camera. It was postulated that this was due to scattering of the laser light which could also be responsible for the structure visible when the ZnTe crystal was viewed when illuminated by an attenuated probe laser. In order to investigate this, a Glan–Thompson prism was used to ensure the probe beam had a very high degree of polarization after the beamsplitter. A second Glan–Thompson prism was then used as an analyser and the polarization was measured in two places. The positions of the two prisms and the polarization measurements are shown in figure 5.3 and the results from the polarization measurements are shown in figure 5.4.

It was clear from these results that the degree of polarization was degraded following passage through the accelerator. There was much more visible signal when the analyzing polarizer was aligned with the nominal polarization direction, in the measurements before the light entered the accelerator, than in those after. It is possible that scattering

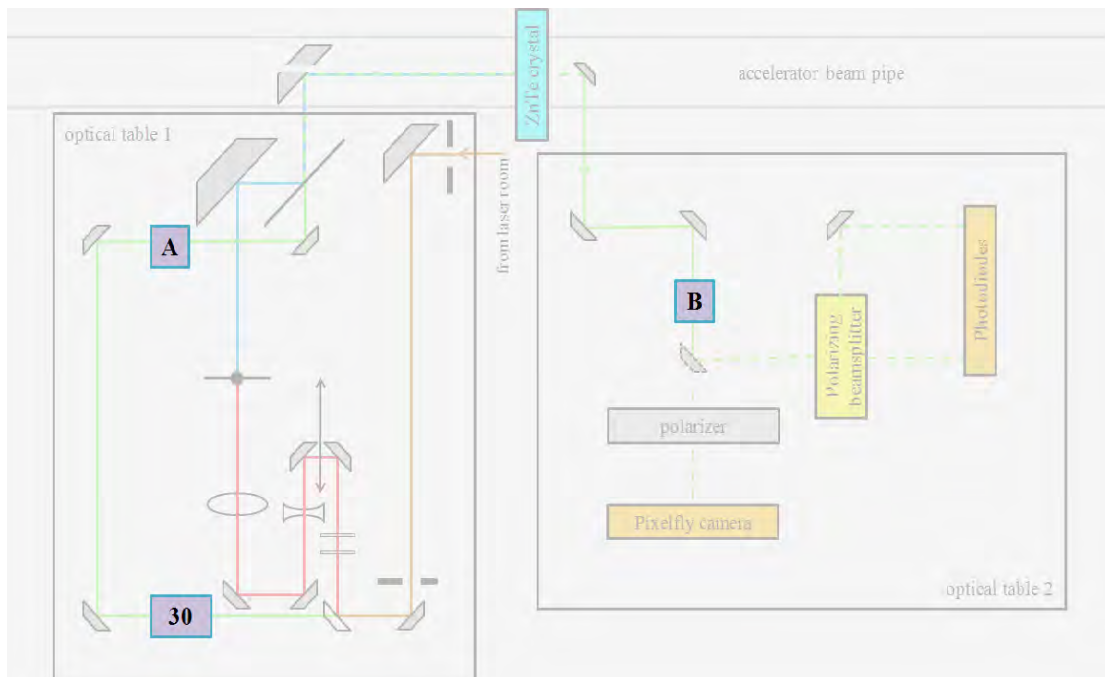


FIGURE 5.3: Positions of the first Glan–Thompson prism (30) used to impose a high degree of polarization and the positions of the two subsequent polarization measurements (A, B)

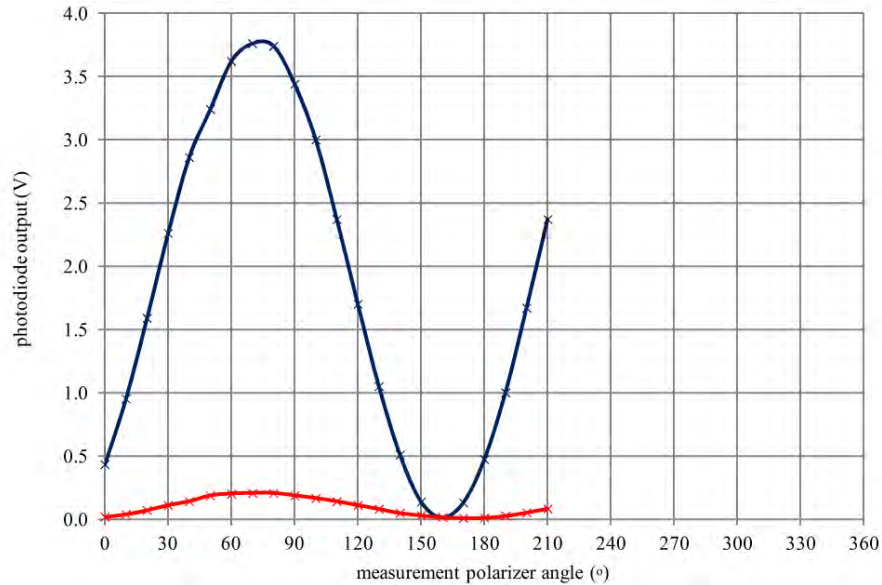


FIGURE 5.4: Results from the polarization measurements made in location A - before entering the accelerator (blue) and B - after the accelerator (red) (see figure 5.3)

of the probe beam (for example from the hole in the centre of the mirror in the accelerator and then on the inside of the vacuum vessel) was responsible for the increase in the depolarized components.

### 5.2.3 Initial terahertz electric field strength measurements

Despite the disappointing results recorded up to this point (or perhaps because of them), the detection system was changed to the photodiode/lock-in amplifier and there was some sign of a weak signal at a relative terahertz-probe laser timing of between 5 and 20 ps; see figure 5.5. This and all subsequent figures showing raw photodiode/lock-in amplifier data have two traces; one red and one black. These correspond to channels A and B from the lock-in amplifier which are data sampled  $90^\circ$  apart in phase. If the lock-in amplifier was set up perfectly and the measured signal had only one in-phase component, one channel would display a signal and the other would be zero.

This and all subsequent figures showing the photodiode/lock-in amplifier signal, plotted against relative timing of the terahertz and probe pulses, should be compared to figure 1.14, which shows a typical result from such a measurement. The  $x$ -axis is the relative timing of the probe laser beam and the terahertz pulse while the  $y$ -axis is the lock-in amplifier sum voltage. The large positive peak corresponds to the probe beam and the peak of the terahertz pulse arriving at the detection crystal at the same time.

### 5.2.4 Investigation into the effect of transverse alignment of the terahertz and probe beams

With the imaging detection system in place and the antenna assembly removed, figure 5.6 shows the two beams (probe beam and the pump beam) overlapping on the ZnTe crystal.

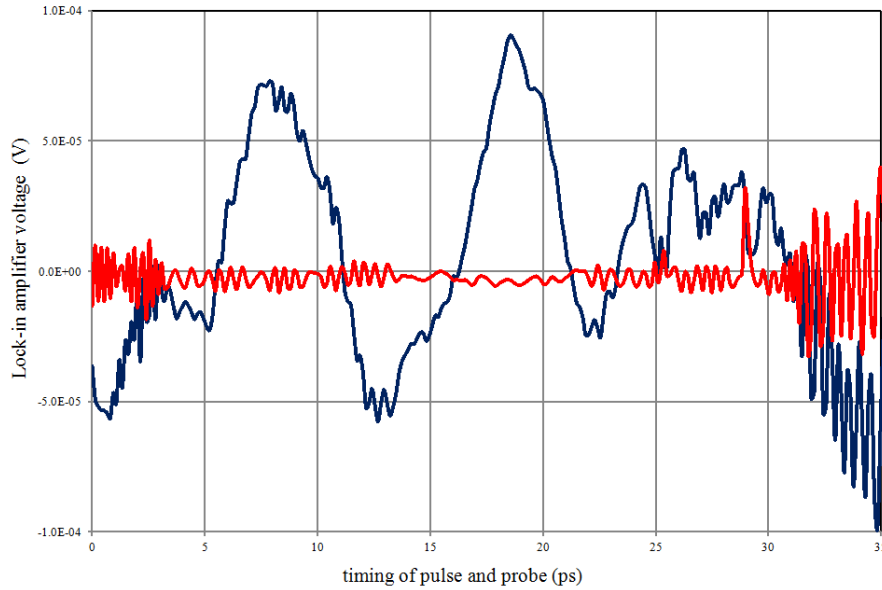


FIGURE 5.5: Photodiode/lock-in amplifier output (plotted against relative timing of the terahertz and probe pulses) showing a possible weak signal on one of the output channels (dark blue) due to terahertz and probe beam overlap. The  $x$ -axis scale corresponds to a translation stage position range of -9.0 to -3.7 mm. The second lock-in amplifier output channel is shown in red.

The crystal can be driven in the horizontal plane from being fully retracted (control system position 0 mm) to being in the path of the electron beam. The initial experiments with terahertz generation and detection were carried out with the crystal at -20 mm. The pump beam required a large amount of attenuation to record such an image whilst avoiding damage to the camera.

After fitting a flipping mirror to enable easier change-over between the Pixelfly camera and the photodiode/lock-in amplifier detection system, the camera was used to calibrate the pump beam movement (and therefore the terahertz once the antenna is back in place) on the ZnTe crystal with respect to the ITO angle (the function of the ITO is described in Section 3.2). Motorized actuators on diagonally opposite corners of the mirror allow it to be tilted an arbitrary number of steps in either the horizontal (X) or vertical (Y) direction; figure 5.7 shows the direction and magnitude of the movement of the centre of the pump beam relative to the centre of the ZnTe crystal. Note this image is rotated  $90^\circ$  around the  $z$ -axis.

Now with photodiode/lock-in amplifier detection and the terahertz antenna back in place, a series of time scans were recorded with the antenna at 100 kV as the ITO was moved again. The maximum terahertz peak was found at an optical delay line translation stage position of  $\approx -14.6$  mm. Table 5.1 lists the movements of the ITO actuator motors and provides the key to figure 5.8, which shows the results overlaid, with the translation stage position converted to time delay. There appears to be no effect on the intensity of the main peak (the one between 1.5 and 3 ps), only a time-shift that is due to the difference in the optical pathlength as the angle of the ITO changes.

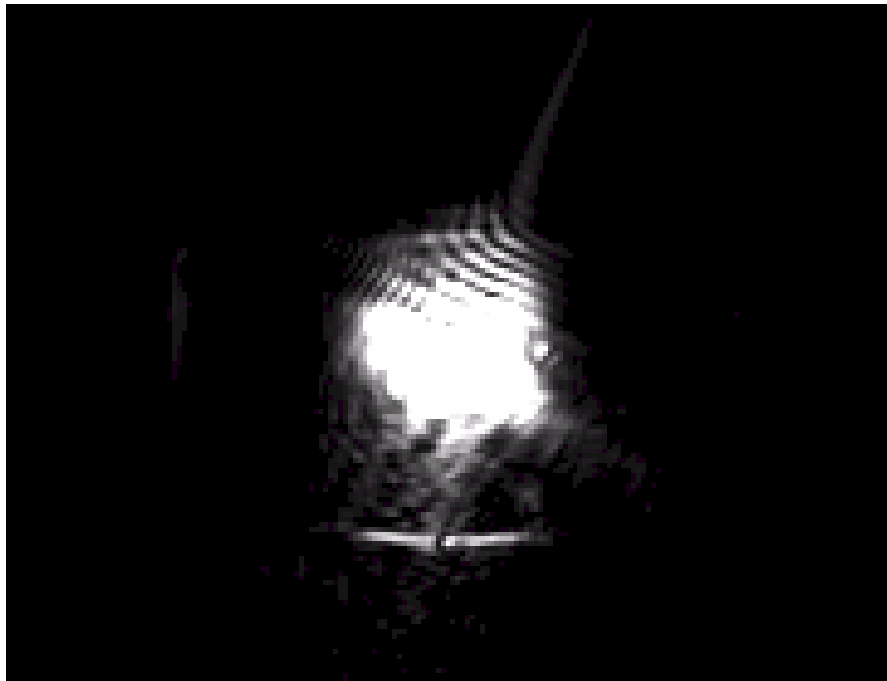


FIGURE 5.6: Probe beam and the pump beam (no antenna present) overlapping on the ZnTe crystal inside ALICE

This is evidence that the terahertz beam is not forming a tightly focussed spot at the ZnTe crystal, nor therefore at the interaction point. The wider peaks seen after the main peak are also unexpectedly intense, with similar amplitude to the main peak, which was not the case for the measurements in the Diagnostics Room.

Following some optical realignment work, more data were collected, this time with

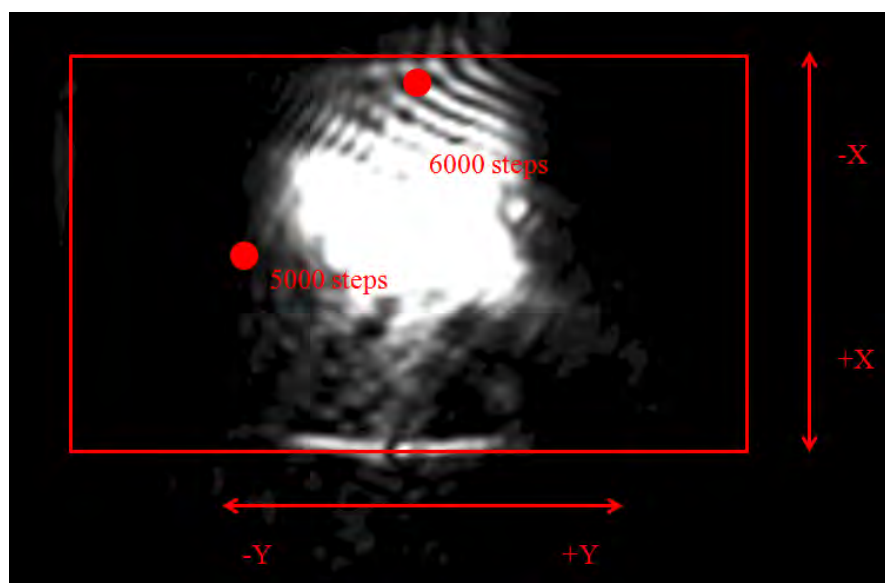


FIGURE 5.7: The direction and magnitude of the movement of the centre of the pump beam (antenna removed) relative to the centre of the ZnTe crystal as a function of the sign and number of ITO actuator motor steps

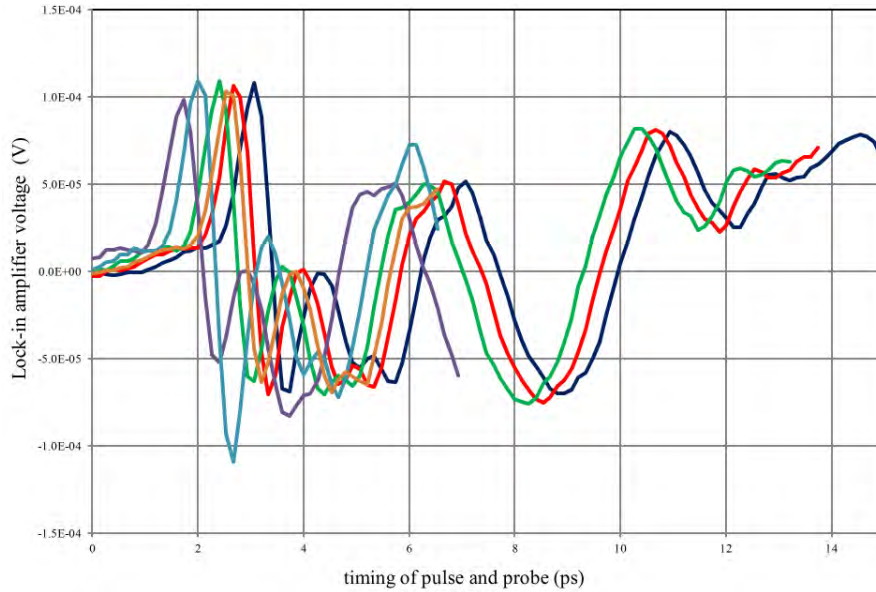


FIGURE 5.8: Photodiode/lock-in amplifier signal (plotted against relative timing of the terahertz and probe pulses) as a function of ITO angle as measured in actuator motor steps. The key to the colours is in table 5.1. The antenna is operating at 100 kV

<i>plot colour</i>	<i>number of steps X-direction</i>	<i>number of steps Y-direction</i>
dark blue	0	-5,000
red	0	0
green	0	+5,000
purple	0	+15,000
light blue	+10,000	0
orange	-10,000	0

TABLE 5.1: The X and Y movements of the ITO actuator motors and the key to the data displayed in figure 5.8

the antenna at 80 kV and the main peak having moved to a translation stage position of  $-9.85$  mm. These data are shown in figure 5.9. In addition to unexpectedly large signals after the main peak (seen earlier) there would also appear to be further unexplained peaks before the main one. With the translation stage fixed at  $-9.85$  mm (i.e. the position of the largest signal peak) data were recorded as a function of the number of ITO actuator drive steps (with the antenna at 80 kV). Figures 5.10 and 5.11 show these data, in the horizontal (X) and vertical (Y) directions. As a weak maximum was found a time scan was undertaken at 80 kV and at the optimum ITO X and Y tilt; see figure 5.12.

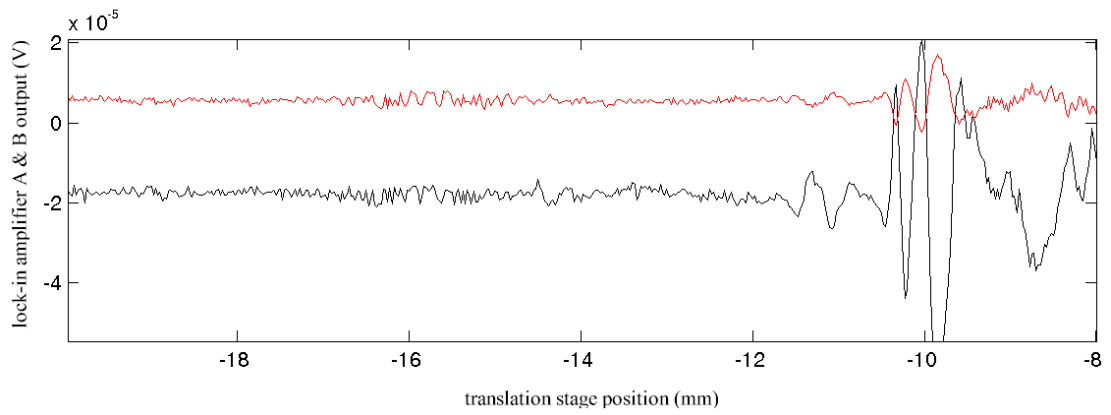


FIGURE 5.9: Photodiode/lock-in amplifier signal as a function of translation stage position with the antenna at 80 kV. The main peak has moved to a translation stage position of  $-9.85$  mm following some re-alignment. Lock-in amplifier channel A (black) and channel B (red)

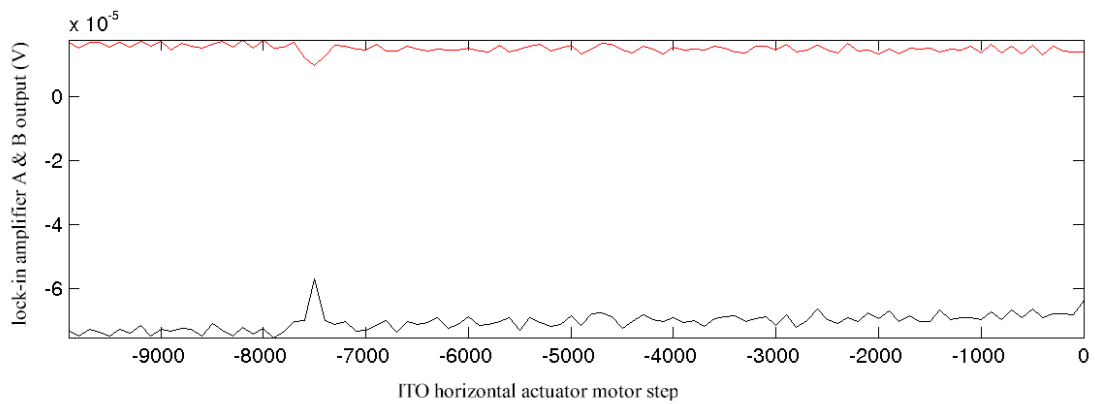


FIGURE 5.10: Photodiode/lock-in amplifier signal as a function of the number of ITO horizontal actuator motor steps, at a fixed translation stage position of  $-9.85$  mm. Lock-in amplifier channel A (black) and channel B (red)

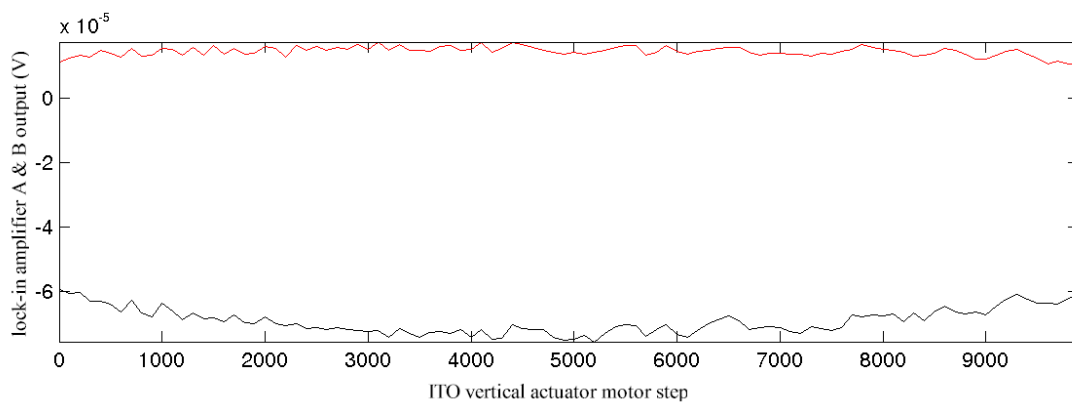


FIGURE 5.11: Photodiode/lock-in amplifier signal as a function of the number of ITO vertical actuator motor steps, at a fixed translation stage position of  $-9.85$  mm. Lock-in amplifier channel A (black) and channel B (red)

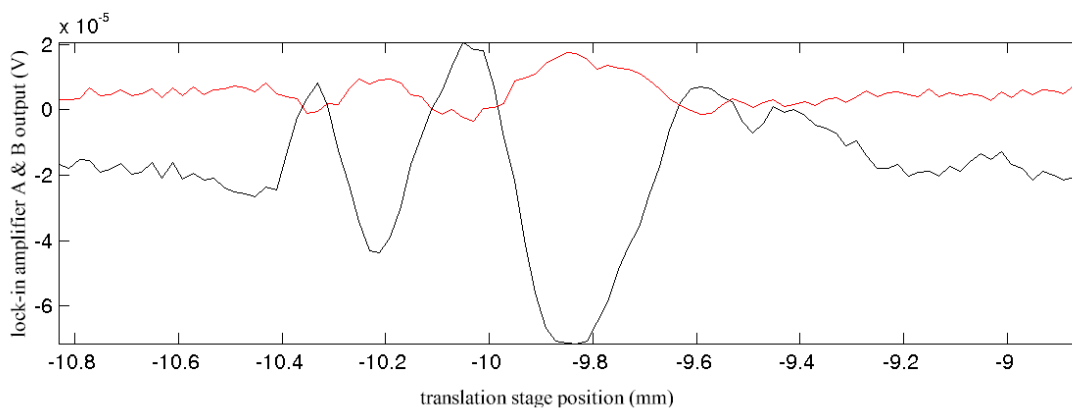


FIGURE 5.12: Photodiode/lock-in amplifier signal as a function of translation stage position with the antenna at 80 kV and the optimum ITO horizontal and vertical tilt for maximum signal strength. Lock-in amplifier channel A (black) and channel B (red)

### 5.2.5 Terahertz signal as a function of antenna voltage

Following the optimization of the overlap of the terahertz pulse with the laser probe beam on the ZnTe crystal recorded in the previous section, the behavior of the signal recorded by the lock-in amplifier as the antenna voltage was increased from 80 kV to 130 kV was recorded. Figure 5.13 shows the change in the signal as the antenna voltage was increased from 80 kV to 130 kV while sitting on this peak position. Figure 5.14 shows the results of a time scan at this increased voltage. The range between the largest positive and negative peaks of the signal is  $1.5 \times 10^{-4}$  V. The increase in antenna voltage was by a factor of 1.6; the increase in the peak-to-peak signal was by a factor of 1.7, which is a reasonable agreement for such a crude measurement.

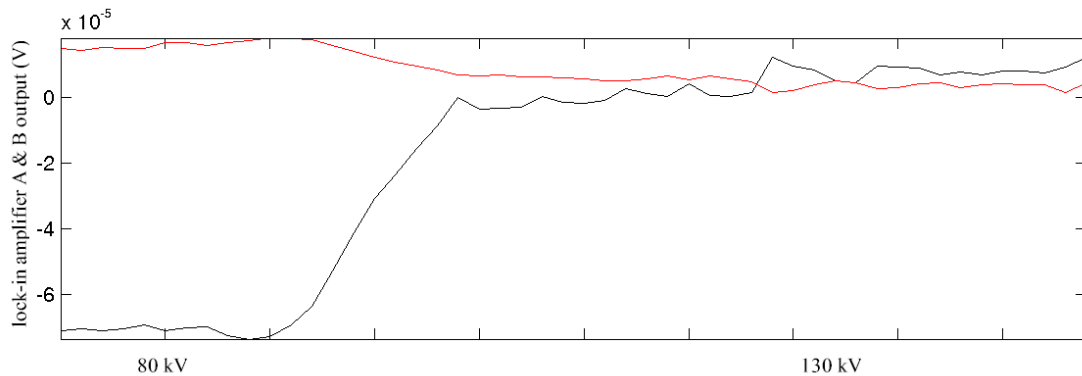


FIGURE 5.13: Photodiode/lock-in amplifier signal at a fixed translation stage position of -9.85 mm as the antenna voltage is increased from 80 to 130 kV. Lock-in amplifier channel A (black) and channel B (red)

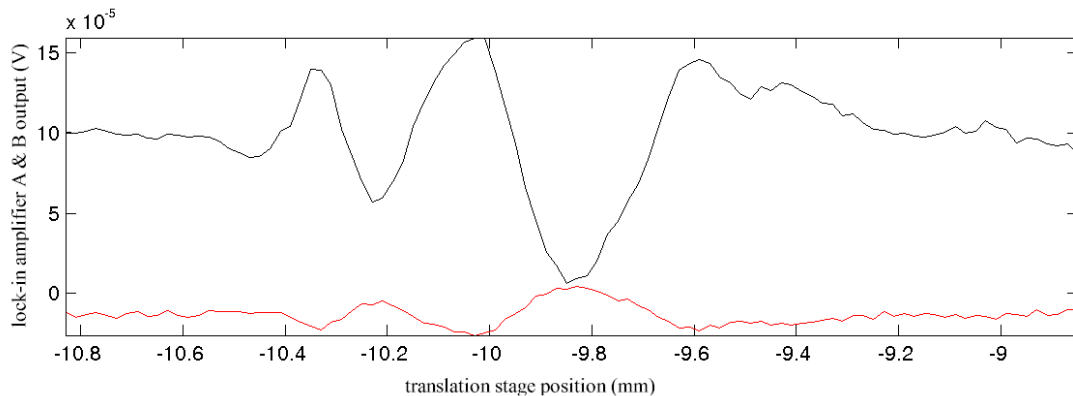


FIGURE 5.14: Photodiode/lock-in amplifier signal recorded with the antenna at 130 kV. Lock-in amplifier channel A (black) and channel B (red)

### 5.2.6 Signal as a function of terahertz focussing

Because the experiments described in the previous section seemed to demonstrate only a weak dependence of the measured terahertz field strength with the alignment of the beam on the ZnTe crystal, it would appear that the terahertz was not forming a tightly

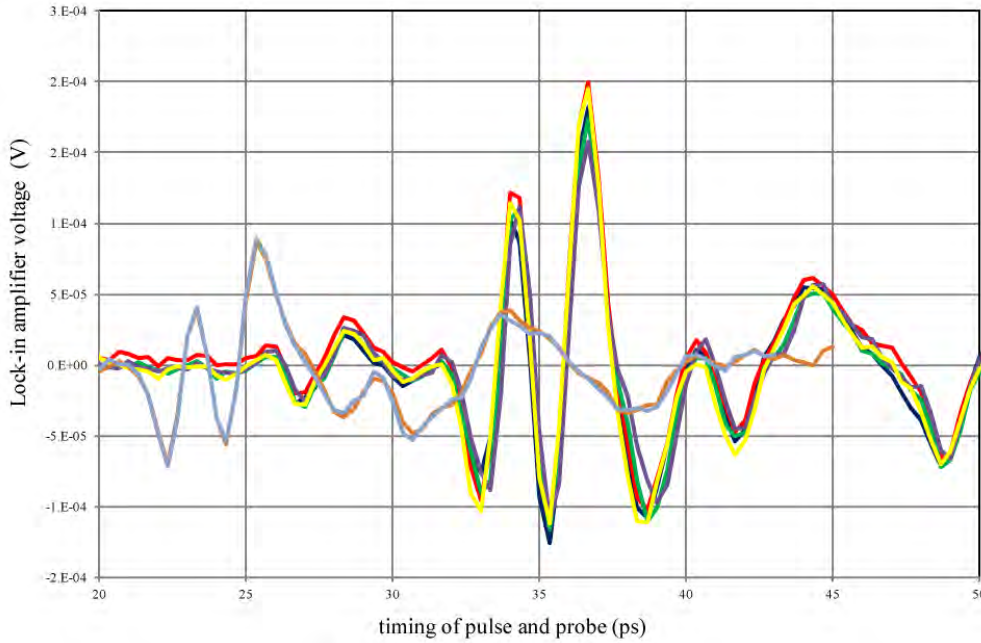


FIGURE 5.15: Photodiode/lock-in amplifier signal recorded with the antenna at 100 kV at different terahertz focus positions. Plot colour, relative mirror (12) position and the position of the corresponding focus in Straight 2 of ALICE given by table 5.2

focussed spot. To investigate this further, lens (12), which focuses the pump beam before the antenna, was placed on a manually-adjustable slide, so that its longitudinal position could be changed, thus altering the longitudinal position at which the focus was formed. As explained in Chapter 1, the terahertz beam produced by the antenna should come to a focus at the same longitudinal position as the pump laser without the antenna.

A series of time scans were undertaken at 100 kV antenna voltage and different focussing lens positions. Table 5.2 shows the position of mirror (12) (relative to where it is when the pump beam comes to a focus on the ZnTe crystal) and the position of the corresponding focus in Straight 2, with the plot colour corresponding to that data in figure 5.15, which shows the results overlaid on one chart. A positive value of the position means that the focussing lens (12) has been moved closer to the diverging lens (10). The positions and amplitudes of the main peaks are mainly unchanged, except

Chart colour	Relative position of lens (12) (mm)	Approximate focus position
yellow	-14	beyond ZnTe crystal
dark blue	0	on ZnTe crystal
red	+24	between ZnTe crystal and ST2-LM-MIR-01
green	+74	200 mm before ST2-LM-MIR-01
purple	+124	350 mm before ST2-LM-MIR-01
brown/grey	-	(12) removed: no focus formed

TABLE 5.2: Relative position of lens (12), the position of the corresponding focus in Straight 2 of ALICE and the corresponding colour on figure 5.15

when the focus lens is removed, which brings the peaks forward in time due to the refractive index of the lens material. The amplitude of the peak without the lens is also reduced by a factor of about two.

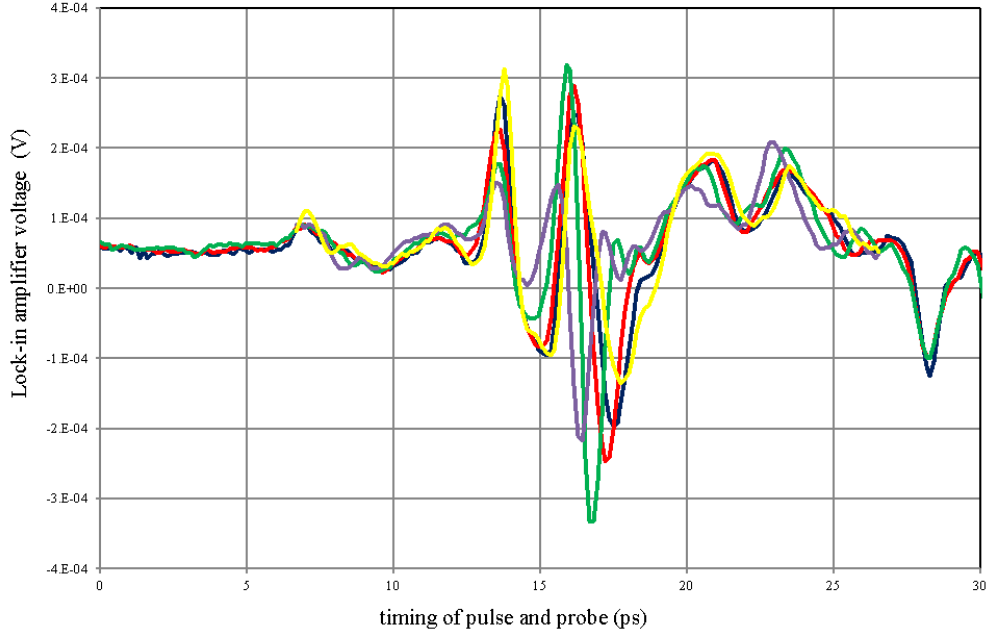


FIGURE 5.16: Photodiode/lock-in amplifier signal recorded with the antenna at 40 kV at different terahertz focus positions. Plot colour, absolute mirror (12) position and the position of the corresponding focus in Straight 2 of ALICE given by table 5.3

Subsequently the manually-adjustable slide for lens (12) was replaced by a motorized stage and a new set of data collected at an antenna voltage of 40kV. With the ZnTe crystal transverse position at -14 mm and other optical adjustments associated with the installation of the stage, the largest signal was recorded at an optical delay line stage position of 4.65 mm. Table 5.3 shows the calculated position of the focus in Straight 2 with the plot colour corresponding to the data in figure 5.16, which shows the results overlaid on one chart. In this case a larger value for the position means that the focussing lens (12) has been moved closer to the diverging lens (10).

It can be seen from both these sets of data that changing the position of the focussing lens had little effect, although interestingly with the antenna at a lower voltage (in

<i>Chart colour</i>	<i>Absolute position of lens (12) (mm)</i>	<i>Approximate focus position</i>
yellow	160	beyond ZnTe crystal
dark blue	175	on ZnTe crystal
red	189	midway between ZnTe crystal and ST2-LM-MIR-01
green	220	on ST2-LM-MIR-01
purple	290	300 mm before ST2-LM-MIR-01

TABLE 5.3: Absolute position of lens (12), the position of the corresponding focus in Straight 2 of ALICE and the corresponding colour on figure 5.16

figure 5.16) there was definitely an increase in the peaks at  $\approx 16$  and  $17$  ps and a reduction of the peak at  $\approx 13$  ps, as the focus position is brought closer to ST2-LM-MIR-01. However the inescapable conclusion is that the terahertz pulse was not forming a very well-focussed spot and therefore the terahertz electric field strength would be significantly smaller than it ought to have been.

### 5.2.7 Investigation of the signal as a function of the transverse antenna alignment

Following careful re-alignment of the probe beam on to the photodiodes to maximize the signal, an investigation was undertaken of the effect of moving the whole high-voltage enclosure of the antenna transversely on the optical table. Because the high-voltage enclosure has circular apertures for the pump beam to enter and the terahertz beam to exit, and the pump beam is set up to slightly overfill the entrance aperture, the effect of this would be that both edges of the antenna would not be illuminated fully. This would not necessarily be a symmetrical effect; this depends on by how much the pump beam overfills the entrance aperture. Figure 5.17 shows the results after moving the enclosure approximately 2 cm to the right and 2 cm to the left, as well as an average of the two sets of data from the centre position (before and after moving - these are shown in figure 5.18). Comparing the plots from the non-central positions, all the peaks are of opposite polarity with the antenna enclosure towards one side compared to the other. The trace from the central position is almost the sum of the other two traces, except for one peak at 11 ps. Exactly the same result is seen from the channel B data. Figure 5.18 shows photodiode data from channel A of the lock-in amplifier, recorded at 130kV, before the high-voltage enclosure was moved from and after it was returned to the approximate centre. The peak at 9 ps, that has opposite polarity in the data from the left movement compared to the right, was minimized when the enclosure was returned to the centre. This can be seen to have had little effect.

### 5.2.8 Effect of part-illumination of the antenna

The time domain structure of the terahertz pulse was investigated as parts of the pump beam illuminating the wafer were blocked with aluminium foil. The antenna was operated at 100 kV. Figure 5.19 shows a comparison of the measured signal from the illumination of the whole antenna with that from just the top or the bottom; all the peaks visible in the whole-antenna signal are present and have the same polarity in the data from the part-illuminated antenna. Figure 5.20 shows a comparison of the measured signal from illumination of the whole antenna with that from just the left or the right; apart from the largest peak in the whole-antenna signal, when the left and right signal peaks would appear to have the same polarity, all other peaks from the left and right of the antenna are of opposite polarity. These data are qualitatively very similar to those recorded when the whole high-voltage assembly was moved left or right.

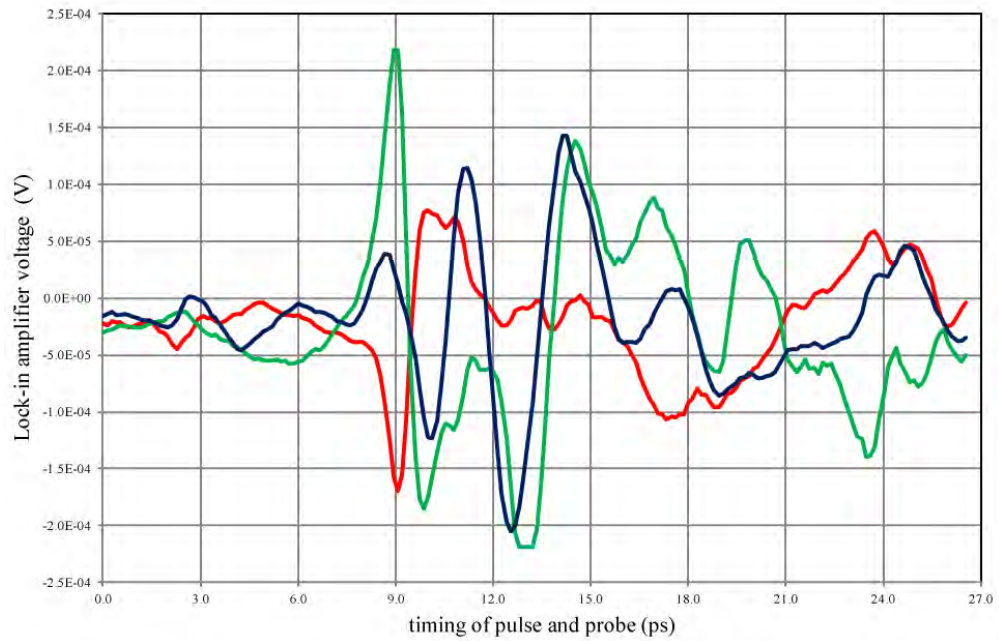


FIGURE 5.17: Photodiode/lock-in amplifier channel A, recorded with the antenna at 130 kV, with the high-voltage enclosure central (blue), moved approximately 2 cm to the right (red) and 2 cm to the left (green)

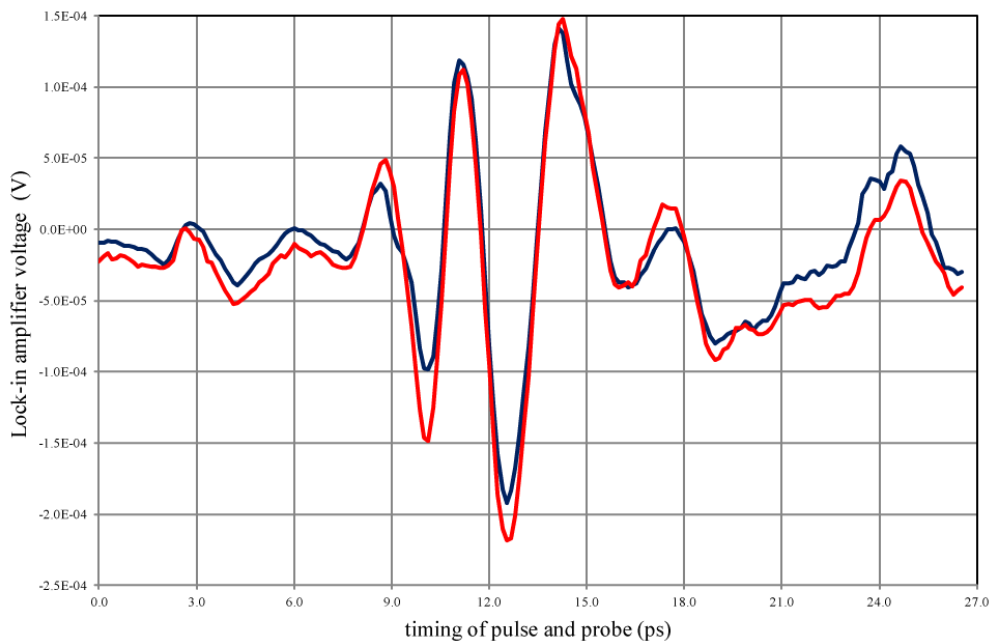


FIGURE 5.18: Photodiode/lock-in amplifier channel A, recorded with the antenna at 130 kV, before the high-voltage enclosure was moved (blue) and after it was returned to the approximate centre (red)

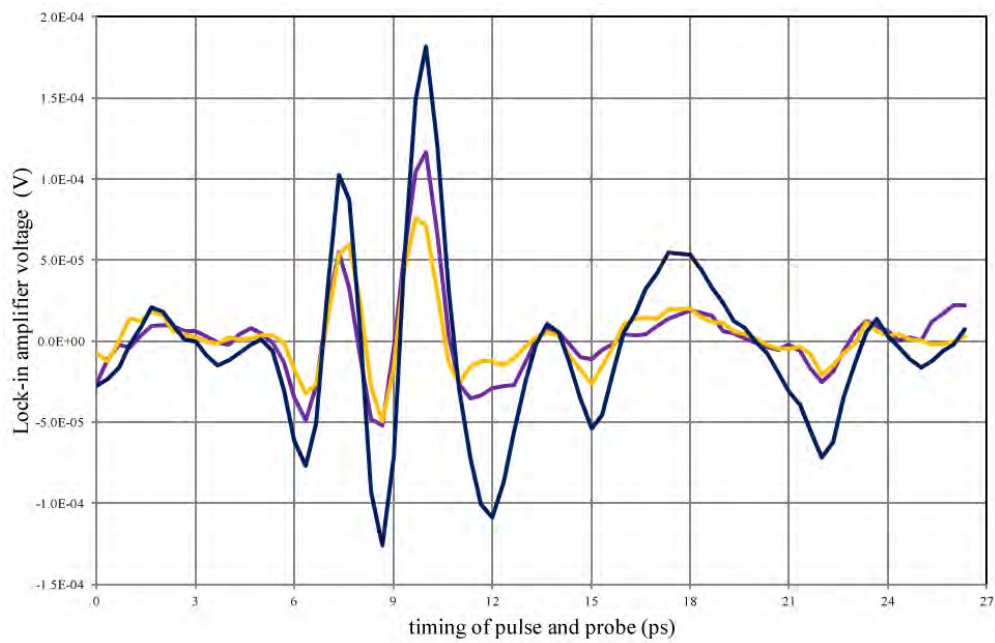


FIGURE 5.19: Comparison of the photodiode/lock-in amplifier channel A signal from illumination of the whole antenna (blue), with that from just the top (purple) or the bottom (yellow), recorded with the antenna at 100 kV

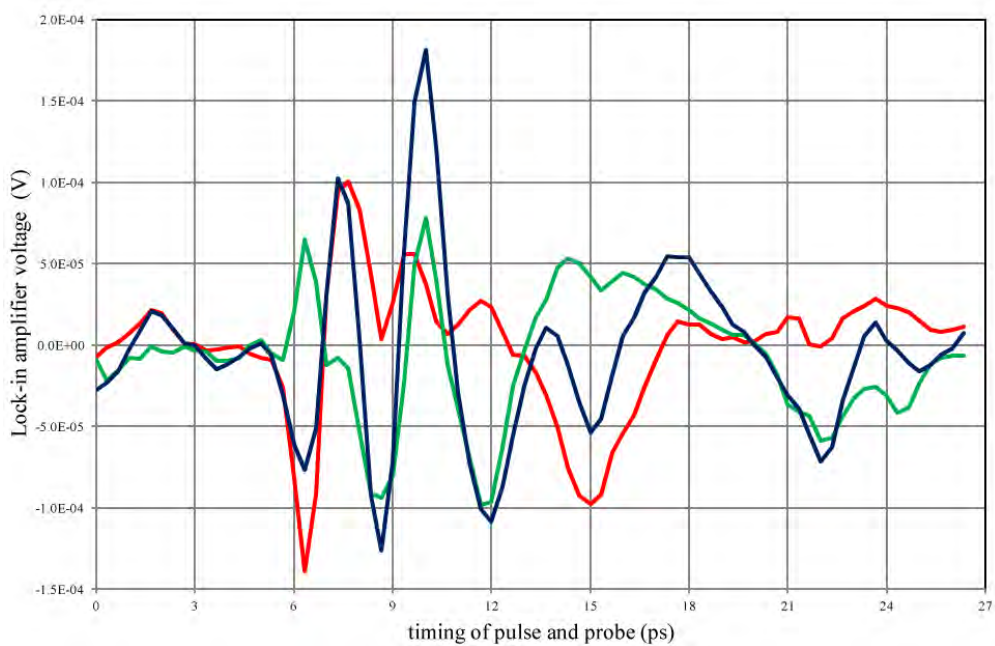


FIGURE 5.20: Comparison of the photodiode/lock-in amplifier channel A signal from illumination of the whole antenna (blue), with that from just the left (green) or the right (red), recorded with the antenna at 100 kV

## 5.3 ALICE beam set up and measurement

### 5.3.1 Establishment of the basic beam parameters

Table 4.3 shows the ALICE beam parameters chosen for the AEMITR experiment. As a starting point, a new ALICE set up was produced by YS, in which the most fundamental parameters: beam energy, bunch charge and energy spread were set to the values required. This was achieved mainly by adjustments to the injector section of ALICE and also the main linac. Bunch charge was set by adjusting the attenuation of the photoinjector laser, thus controlling the amount of charge produced by the cathode. The energy spread was minimized by adjusting the phases of the buncher cavity, the second booster cavity (BC2) and both linac cavities (LC1 and LC2). The first booster cavity (BC1) is generally left unmodified in most ALICE setups, as the capture of the non-relativistic beam by the fields in the first cell is very sensitive to the RF phase and this has a major effect on all subsequent parameters. The operational phase of the accelerating cavities is specified as the off-crest angle; i.e. relative to the phase that gives maximum field and therefore maximum acceleration (on-crest). These settings were  $BC1/2 = -20/+40^\circ$  and  $LC1/2 = 0/0^\circ$  (i.e. on-crest). The required buncher phase is that for which the electron bunch transits the buncher cavity as the RF amplitude is zero (so there is no net acceleration - known as zero-cross phase) and bunching occurs (the electrons at the beginning of the bunch seeing a decelerating gradient, the electrons at the end of the bunch seeing an accelerating gradient). This gave an energy spread of  $\sim 14$  keV RMS (or 0.06%). Finally the kinetic energy was set in both the injector (to 6.5 MeV) and in the rest of the machine (to 22.5 MeV).

As described in Chapter 4, new machine optics were developed to give a small beam waist at the interaction point. The required quadrupole magnetic field gradients were then translated to magnet currents using the table of measured magnet properties which were then manually entered into the ALICE control system. Small manual adjustments to the quadrupole currents while looking at the image of the beam at the interaction point and in the chicane were then made to finalize the basic setup. All the magnet parameters were then saved using ALICE's Back-Up and Restore Tool (BURT).

Subsequent experimental shifts would generally follow the pattern of reloading the last AEMITR optics using the BURT system, which would restore all the magnet currents (and hence magnetic field strengths and gradients, ignoring potential hysteresis effects, which could not be eliminated in the quadrupoles). RF system settings (buncher, booster and linac gradients (power) and phases) would be manually set to their values from the time at which the now-restored magnet currents had been saved.

### 5.3.2 RF system settings

However, due to drift in the relative phase of the two RF Master Oscillator (MO) outputs: 1.3 GHz for the RF system itself and 81.25 MHz for the photoinjector laser, the phases of the three RF devices (buncher, booster and linac) had to be reset for each

experimental run. The buncher zero-cross phase was found using a macro embedded in an Excel spreadsheet which takes data from an oscilloscope recording the arrival time of electron bunches from the gun at the first BPM, referenced to the RF phase. This measurement is made at low and high buncher power as a function of buncher phase; at zero-cross there will be no net acceleration and therefore no difference in the time of flight to the BPM between low and high buncher power. The phases of the four accelerating cavities could be found by looking at the beam position on a screen in a region of high dispersion and determining the phase that gave maximum beam energy. The nominal off-crest phases of the booster and linac cavities, determined in the initial setup, were then set. Because of the importance of achieving minimum energy spread these values were refined; first in the injector using only BC2 to minimize the horizontal beam size on a screen in a region of high dispersion, INJ-DIA-YAG-05. This process was then repeated with the phases of LC1 and LC2 and screen AR1-DIA-OTR-01. The two linac cavities were kept at identical phases, which were very close to zero as the energy spread is dominated by the setup of the injector.

The same two screens were used to set the energy; first in the injector and then after the linac. Taking care to degauss the dipole magnets in the injector first (cycling the current in steps between zero amperes and the maximum value possible, in order to eliminate variations in the field due to hysteresis) the energy of the electrons leaving the injector was set by adjusting the gradient in BC1 and BC2, to position the beam central on the screen INJ-DIA-YAG-05 with the powered dipole magnet that precedes it (INJ-MAG-DIP-01) set to the reference current for the desired injector energy. This process was then repeated with both linac cavities, except that the beam was positioned centrally on AR1-DIA-OTR-01 with the current in dipole magnet AR1-MAG-DIP-01 set to its reference value.

Figure 5.21 and Figure 5.22 show the images of the electron beam on screens INJ-DIA-YAG-05 and AR1-DIA-OTR-01 respectively following minimization of the energy spread and setting of the beam energy.

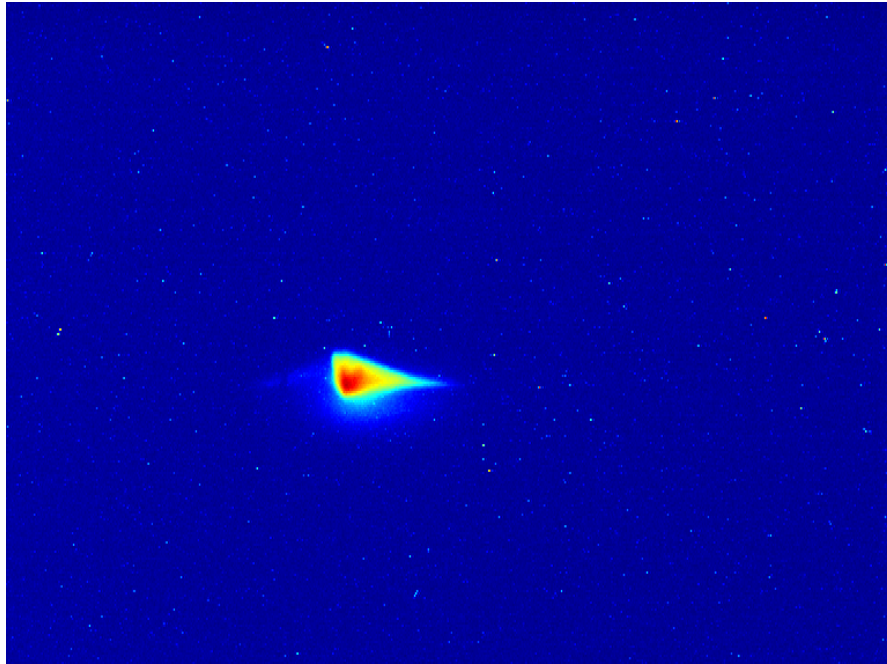


FIGURE 5.21: Image of the electron beam on screen INJ-DIA-YAG-05 following minimization of the energy spread and setting of the injector energy

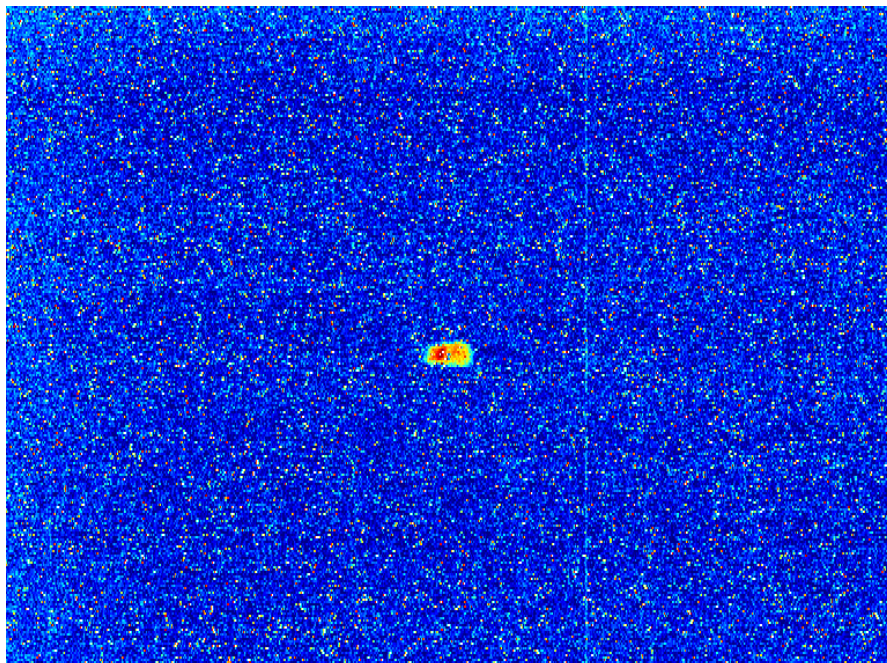


FIGURE 5.22: Image of the electron beam on screen AR1-DIA-OTR-01 following minimization of the energy spread and setting the full energy

### 5.3.3 Obtaining the desired beam waists via quadrupole scans (AW)

Because of the significant re-optimization of the RF system settings at the start of each AEMITR shift there was always some variation in the Twiss parameters of the beam as it left the linac, due to changes in the amount of RF focussing. Because of the very precise control of beam size required at the interaction point and at the chicane screen, it was necessary to measure the Twiss parameters at the linac exit before the start of each experimental period. As described in Chapter 4, the Twiss parameters were measured via quadrupole scans in Straight 2 and then propagated back to the linac exit in an accelerator optics code such as MAD. The linac exit Twiss parameters were then matched forward to the required values at the interaction point in Straight 2, generating a revised table of quadrupole magnet gradients and subsequently magnet currents. A typical set of screen images from ST2-DIA-OTR-01 acquired during a quadrupole scan of ST2-MAG-QUAD-02 are shown in Figure 5.23.

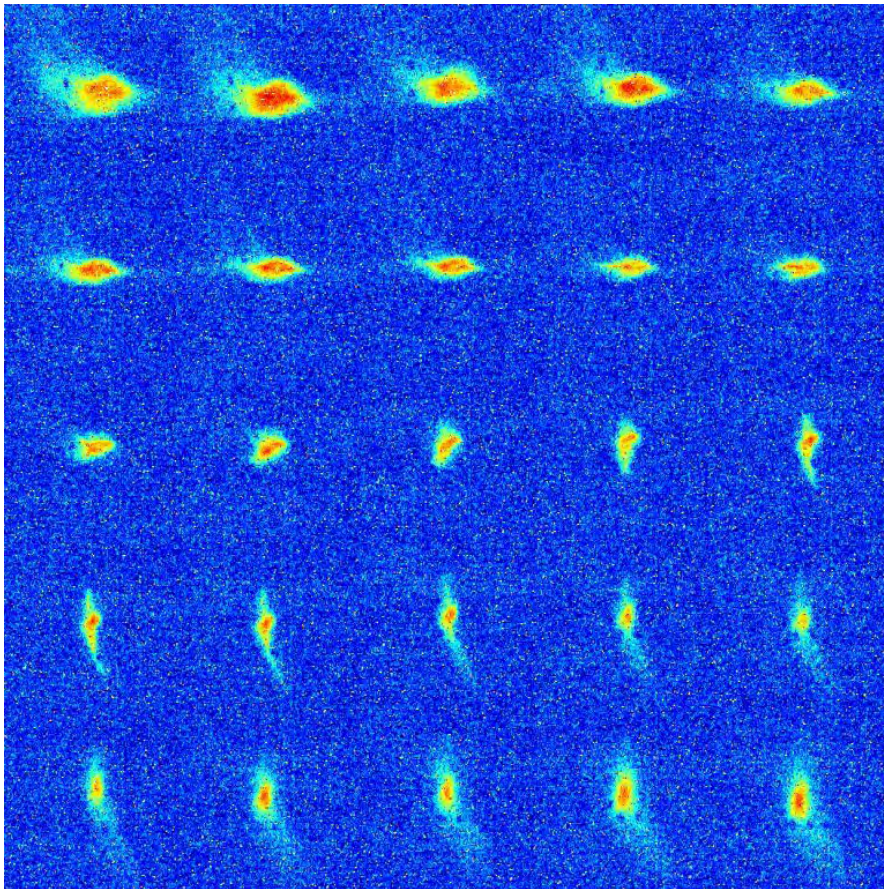


FIGURE 5.23: Screen images from ST2-DIA-OTR-01 acquired as quadrupole ST2-MAG-QUAD-02 is changed from 0.80 to 2.00 A in 50 mA steps

Figure 5.24 shows a plot of  $\sigma^2$  vs  $(1 - k_1 L)$ , for both horizontal and vertical directions, measured on the screen images of figure 5.23, along with the quadratic fits to the data.

Table 5.4 shows the values for the Twiss parameters and emittance derived from the curve fitting.

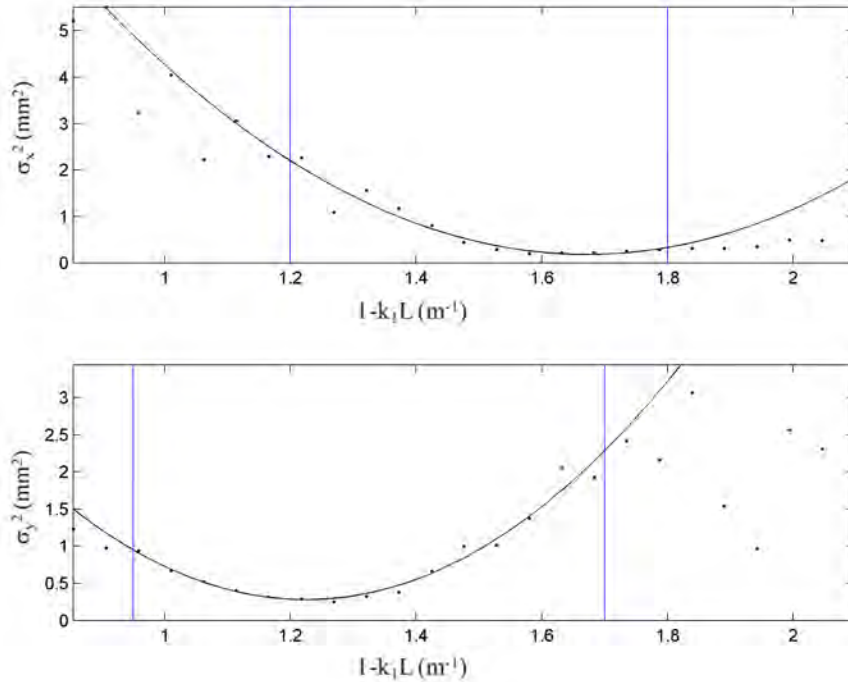


FIGURE 5.24: Plot of  $\sigma^2$  vs  $(1 - k_1L)$ , for both horizontal and vertical directions, along with the fitted quadratics. The blue lines indicate the region within which the data was used to calculate the fit

$\alpha_x$	-10.21	
$\beta_x$	7.09	m
$\gamma\epsilon_x$	2.95	$\mu\text{m}$
$\alpha_y$	8.19	
$\beta_y$	5.62	m
$\gamma\epsilon_y$	3.64	$\mu\text{m}$

TABLE 5.4: Twiss parameters and emittance derived from analysis of quadrupole scan screen images of figure 5.23, after calculating a quadratic fit to the data as shown in Figure 5.24

Following the measurement of the Twiss parameters in Straight 2 using quadrupole scans, they could be propagated back to the linac exit and then used as the initial values in a MAD model of the electron optics for AEMITR. Once the calculated quadrupole gradients had been applied, measurements of the beam size around the machine allowed the comparison of the model with reality. Figure 5.25 shows the result of this exercise. The black and red lines are the horizontal and vertical  $\beta$  functions while the circles represent the measurements of the  $\beta$  functions at screens around the machine, calculated from the measured beamsizes. An rms energy spread ( $\sigma_E$ ) of 10 keV is assumed.

Despite the good agreement between the MAD model and the measured beam size, sometimes a small manual adjustment of the quadrupoles in Straight 2 gave a tighter focused spot in the chicane. Figure 5.26 shows an example of the improvement that could be made to the beam image in the chicane by manual adjustment of the quadrupoles ST2-MAG-QUAD-03 and ST2-MAG-QUAD-04.

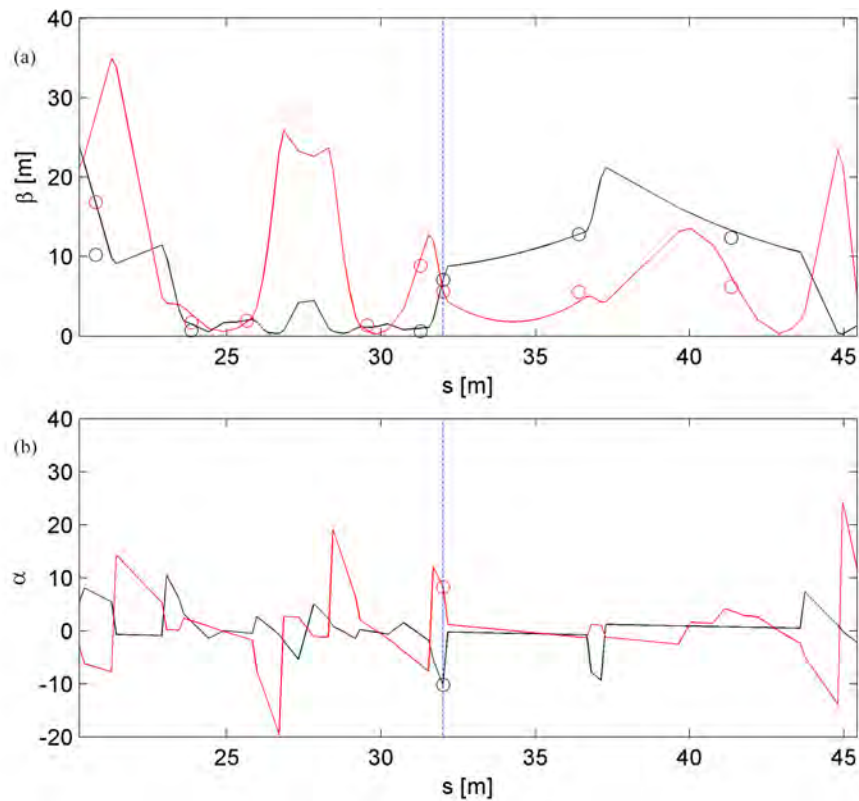


FIGURE 5.25: A comparison of Twiss parameters derived from screen measurements around ALICE (circles) with the calculated values from the MAD electron optics model based on the quadrupole scan data analyzed in this section; (a) and (b) are the beta and alpha functions respectively (horizontal is black and vertical is red). The blue line indicates the position of the start of the quadrupole magnet used in the quadrupole scan.

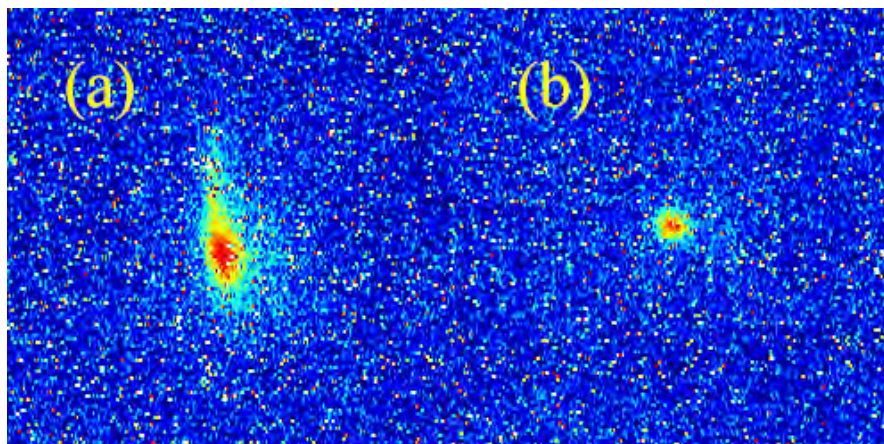


FIGURE 5.26: An example of the improvement that could be made to the beam image in the chicane by manual adjustment of the Straight 2 quadrupole gradients from the values predicted by the model; (a) before, where  $\sigma_x = 0.46$  and  $\sigma_y = 0.71$  mm (b) after, where  $\sigma_x = 0.34$  and  $\sigma_y = 0.44$  mm

### 5.3.4 Dispersion measurements

Apart from achieving the small beam waist at the interaction point and the detection point in the chicane, the other important aspect of the new AEMITR optics was measurement of the dispersion in the chicane, which allows one to measure the additional energy spread induced into the electron bunch as a horizontal beam size increase and thus to quantify the energy modulation induced by the interaction with the terahertz. Quantifying the dispersion is also a test of the agreement between real accelerator tuning and the machine optics model.

Using the known magnet parameters for the first dipole in Arc 1 (AR1-MAG-DIP-01) it was possible to calibrate the beam energy as a function of linac gradient. To measure the dispersion at the detection screen in the chicane (ST2-DIA-YAG-01), the horizontal and vertical beam centroid positions at the screen were recorded as a function of linac gradient and therefore energy. Because the train-to-train energy jitter adds noise to the position measurement, a few screen images were recorded at two different energies (linac gradients) and the average centroid position calculated for each set. The dispersion was then calculated as described in Chapter 4. Table 5.5 shows the results of the beam centroid measurement at ST2-DIA-YAG-01, the energies at the two positions and the calculated dispersion.

LC2 gradient	18.2	16.7	
Kinetic energy	22.63	22.09	MeV
$\Delta E/E$		2.4	%
Mean centroid position	11.044	22.997	mm
$\Delta x$		11.95	mm
$\eta_x$		0.50	m

TABLE 5.5: Dispersion calculation using the average beam centroid position on ST2-DIA-YAG-01 measured at two energies.

The value of the dispersion predicted by the MAD model at this point in the lattice is about 0.42 m; so a value of 0.50 m is consistent but not exactly the same. This means the dispersion at the interaction point is presumably not exactly zero which it should have been with properly tuned optics.

### 5.3.5 Steering through the apertures in Straight 2

In order for the terahertz beam and the electron beam to co-propagate along the accelerator beam tube, the electron beam had to pass through a 5 mm diameter hole in a 45° metal mirror (ST2-LM-MIR-01) which reflects the terahertz beam down the electron beam path. A second 10 mm diameter hole in the aperture plate (one of two devices referred to in the control system as ST2-LM-YAG-01) 1.35 m downstream is designed to block the terahertz beam (via diffraction) while the electron beam passes through unaffected. The centres of these apertures had already been aligned (Section 4.4) on a reference line established between the centre points of the OTR screens upstream and

downstream of this section of the accelerator (ST2-OTR-01 and 02). The only steering coils for modifying the trajectory of the electron beam are upstream of both apertures; primarily ST2-HCOR-01 and VCOR-01 but also the correctors and dipoles in Arc 1 if necessary.

Due to small variations in the accelerator set up for each AEMITR run and the consequential variation in the electron optics, it was necessary to establish the settings for the trajectory to pass through both apertures each time an interaction experiment was attempted. The following procedure was developed to do this:

1. Ensure that both the mirror and the aperture plate are fully retracted.
2. Insert ST2-OTR-02. Using a suitable train length (usually a few microseconds) adjust ST2-QUAD-01 and ST2-QUAD-02 so that the beam forms a vertical stripe on ST2-OTR-02. Although this is not essential, it makes it easier to locate the aperture in the aperture plate and to map out the image on ST2-OTR-02.
3. Insert the aperture plate - this will drive the motorised stage to 125 mm; then drive it to the end of its travel (which is just less than 130 mm) by entering 130 mm manually.
4. Using ST2-HCOR-01, scan the beam to map out the image of the aperture plate aperture on ST2-OTR-02 and draw the outline of the aperture on the display using a whiteboard marker.
5. Restore ST2-QUAD-01 and ST2-QUAD-02 to their nominal settings and extract the aperture plate.
6. Steer the beam (using ST2-HCOR-01 and ST2-VCOR-01) so that it is at the centre of the outline of the aperture on ST2-OTR-02 marked on the display.
7. Reduce the train length to single bunch (so as to avoid damage to the YAG screen). Change from the aperture plate to the YAG at ST2-LM-YAG-01. Mark the image of the beam on the display.

Now it is necessary to steer through the ST2-LM-MIR-01 so that the image of the beam on ST2-LM-YAG-01 is identical to that found in step 7. Then, if the YAG of ST2-LM-YAG-01 is replaced by the aperture plate, the beam will go through both apertures.

8. Insert the ST2-LM-MIR-01. Scan the beam using ST2-HCOR-01 and ST2-VCOR-01 to locate the aperture.

If at this stage, the centre of the image of the mirror aperture on ST2-LM-YAG-01 is NOT coincident with the beam image found in step 7, a further step is necessary:

9. Use ST2-HCOR-01 and ST2-VCOR-01 as well as correctors and dipoles in Arc 1 to achieve this.
10. If step 9 is required, the whole procedure should be repeated from the start.

Figure 5.27 shows four images of the beam on ST2-DIA-YAG-01 with the following apertures in the beam pipe: a) none; b) mirror only; c) aperture plate only and d) both mirror and aperture plate.

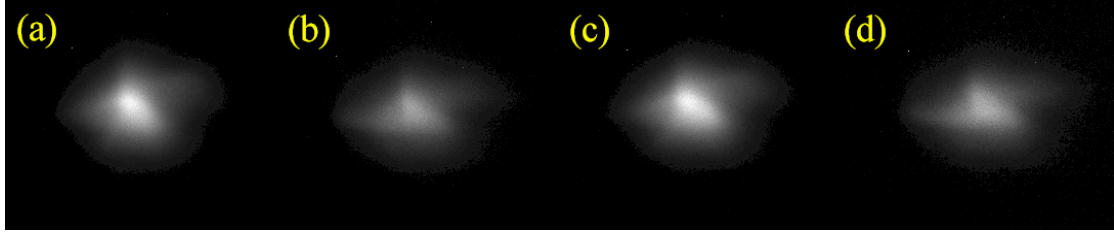


FIGURE 5.27: Images of the electron beam on ST2-DIA-YAG-01 with the following apertures in the beam pipe: a) none; b) mirror only; c) aperture plate only and d) both mirror and aperture plate.

### 5.3.6 Setting up laser-accelerator synchronization

As explained in section 4.3.4, for this experiment to have been a success it was necessary that the electron beam and the terahertz pulse overlapped for as long as possible as they passed through the interaction region. The laser pump beam optical delay stage has a total adjustment range of  $\approx 1.3$  ns and a minimum time step of  $\approx 70$  fs, which was used to scan the relative timing of the terahertz pulse and the electron bunch. If the difference in arrival time was greater than this range then a cruder timing adjustment was necessary, using the Coherent Synchrolock-AP system.

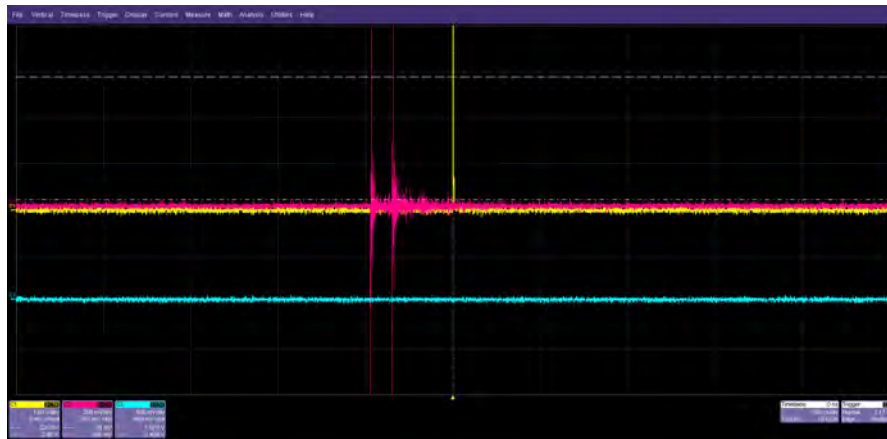


FIGURE 5.28: Oscilloscope display showing signal from the BPM of two bunches (magenta) and the photodiode a signal (yellow)

The relative arrival timing of the electron bunches and the Ti:S laser was measured in Straight 2, with a fast photodiode detecting the laser light being reflected off ST2-OTR-02 whilst a single BPM button (part of ST2-DIA-BPM-02) recorded the passage of the electron beam. These were both connected to an oscilloscope. Figure 5.29 shows the experimental arrangement schematically with the important dimensions labelled A, B, C and D, while figure 5.28 shows the signal from the BPM of two bunches (magenta)

and the photodiode a signal (yellow), captured on the oscilloscope. The time difference between the traces from the laser reflecting off ST2-OTR-02 and BPM signal from the first electron bunch is  $\approx 70$  ns.

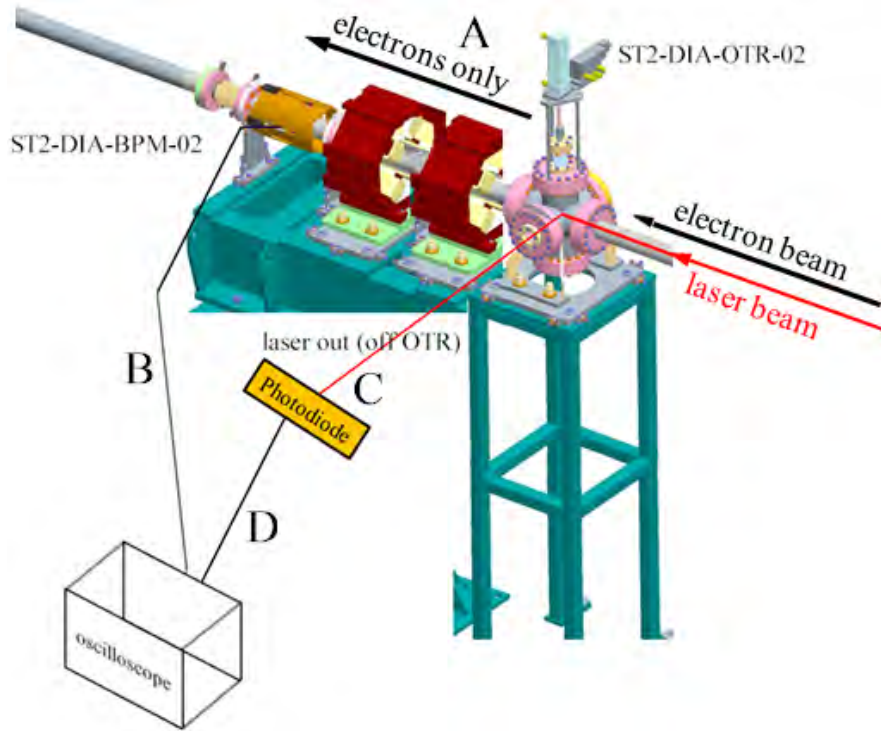


FIGURE 5.29: Schematic of the experimental arrangement used to measure the relative timing of the electron bunch and terahertz pulse in Straight 2, with the important dimensions labelled A, B, C and D

From measurement of the length of the two different paths taken by the electrons and the light, in both vacuum and the cables connecting the photodiode and BPM button to the oscilloscope, the measured time difference between the two signals on the oscilloscope could be converted to the time difference between the electron bunch and the laser pulse (and hence the terahertz pulse) in Straight 2. The values for A, B, C and D along with their conversion into time (assuming signals travel at the speed of light  $c$  in vacuum and at  $2c/3$  in RG58 coaxial cable) are given in table 5.6

A	distance from ST2-OTR-02 to ST2-DIA-BPM-02	1.05	m	3.5	ns
B	cable length from ST2-DIA-BPM-02 to oscilloscope	2.2	m	11	ns
C	distance from ST2-OTR-02 to photodiode	0.2	m	0.67	ns
D	cable length from photodiode to oscilloscope	3.0	m	15	ns
A + B	electron signal path			14.50	ns
C + D	photon signal path			15.67	ns
CD - AB	timing difference			1.17	ns

TABLE 5.6: Pertinent dimensions and corresponding timings from the measurement of the relative timing of the electron bunch and terahertz pulse in Straight 2

Thus the signal from the laser (via the photodiode) will arrive at the oscilloscope approximately 1.2 ns *after* the signal from the electrons, if they are perfectly synchronized inside Straight 2 of the accelerator. If the Coherent Synchrolock-AP system is adjusted so that the oscilloscope displays the signal from the photodiode 1.2 ns *after* the signal from the BPM then there will be maximum temporal overlap of the pulses inside Straight 2. Figure 5.30 shows a plot of the Coherent Synchrolock-AP fundamental phase (the parameter that sets the delay of the laser pulse relative to the ALICE RF system, and therefore the electron beam) against the time difference between the signal from the laser and the signal from the electrons as measured on the oscilloscope.

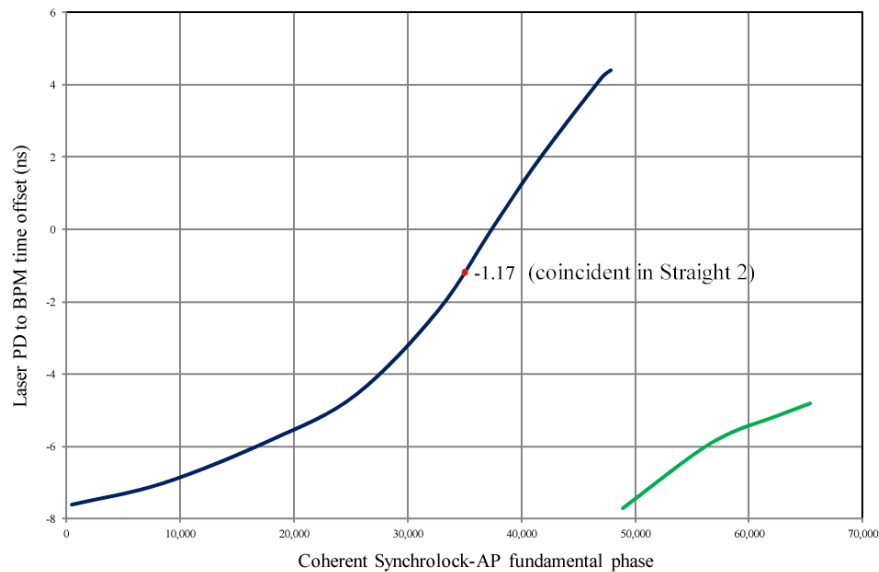


FIGURE 5.30: Coherent Synchrolock-AP fundamental phase versus the time difference between the signal from the laser and the signal from the electrons as measured on the oscilloscope. The point at which the electrons and the terahertz radiation pass down Straight 2 in synchrony is shown in red.

## 5.4 Searches for interaction between the terahertz radiation and the electron beam

### 5.4.1 Introduction

Despite the disappointing results of the measurements of the electric field strength of the terahertz pulses when made inside the accelerator, two opportunities were available to look for interaction. We decided to go ahead and make use of these as a full system test, to gain experience and identify areas for improvement in the future. Unfortunately an even weaker terahertz electric field was produced than had been characterized earlier as it was not possible to maintain the voltage on the antenna that had been achieved during the earlier experiments. It was discovered at a later date that the trigger pulse for the high-voltage pulser had to be longer than 800  $\mu\text{s}$  for the pulser to operate correctly and this may not have been the case.

### 5.4.2 Measurements on 6/11/11

ALICE was set up with AEMITR machine optics using the usual quadrupole scan method. Steering through the two apertures in Straight 2 was completed and terahertz generation was set up at 45kV antenna voltage (the maximum available at the time). The manually adjustable lens (12) was left at a position which would nominally focus the terahertz pulses at the interaction point in Straight 2. The data acquisition program was set up to capture the image of the beam in the chicane on screen ST2-DIA-YAG-01 at each step of the terahertz pump beam optical delay translation stage.

Synchronization between the probe laser and the electron beam was established as described in Chapter 4, using a photodiode pick up for the laser and a BPM pick up for the electrons; it had been calculated earlier that the signal from the laser arrives at the oscilloscope approximately 1.2 ns after the signal from the electrons, if they are perfectly synchronized inside Straight 2 of the accelerator. This point corresponds to a Coherent Synchrolock-AP fundamental phase value of 34900. If they are aligned in time on the oscilloscope, then the terahertz (laser) is 1.2 ns before the electrons in Straight 2. This point corresponds to a Synchrolock fundamental phase value of 37400.

During measurements of the terahertz electric field strength, the optical delay line allows the timing of the pump laser beam (which is converted to terahertz) to be varied relative to the probe laser beam. Because the ALICE laser systems (both the photocathode laser and the Ti:S) are synchronized to the ALICE RF system, the optical delay line can therefore also be used to vary the time of arrival of the terahertz pulses relative to the electron bunches. The temporal overlap of the terahertz and pump beams at the interaction point was determined previously, with the ZnTe crystal in the accelerator, to be at an optical delay line stage position of 4.65 mm. As the maximum range of this stage is  $\pm 100$  mm, the maximum time window available from the operation of the optical delay line is 1,333 ps. The measurements reported here were made over an optical delay line translation stage range of +90 to -90 mm, corresponding to a time window of 1,200 ps.

The experimental parameters for a selection of data sets are listed in table 5.7, along with the corresponding figure numbers. The data displayed is the horizontal and vertical sizes ( $\sigma_x$  and  $\sigma_y$ ) of the beam image recorded on the chicane YAG screen (ST2-DIA-YAG-01). In order to try and reduce the noise in the measurements (due to train-to-train instability) each data point in the figures is a rolling average of five consecutive measurements, divided by the overall average. The Synchrolock-AP phase provided a coarse adjustment of the timing of the electron bunches and the terahertz pulses. This was then combined with the range and fine step control provided by the optical delay line to explore in detail a larger time window than could have been reached by either mechanism independently. Obviously, care was taken to ensure that there were no gaps in the range of timings explored. These data should be compared to figure 1.21, which shows what we would expect to see under the best possible circumstances, with all beam parameters the same as figure 1.19.

There is no evidence of a change in the electron beam size in figure 5.35, where it would be expected to be seen if there had been any interaction. Detailed analysis of the data, to improve the signal-to-noise ratio, did not reveal anything further. A number of further sets of data were collected, after making step changes in the Synchrolock phase, chosen so that for adjacent sets of data there was always some overlap of the time window. No evidence of interaction was detected in these additional measurements.

Part way through the collection of one of these sets of data a large global accelerator phase shift disrupted the excellent machine set-up and had to be recovered before further potential interaction data could be recorded. Figure 5.31 shows the effect of this sudden phase shift on the horizontal and vertical size of the beam image at the chicane YAG screen.

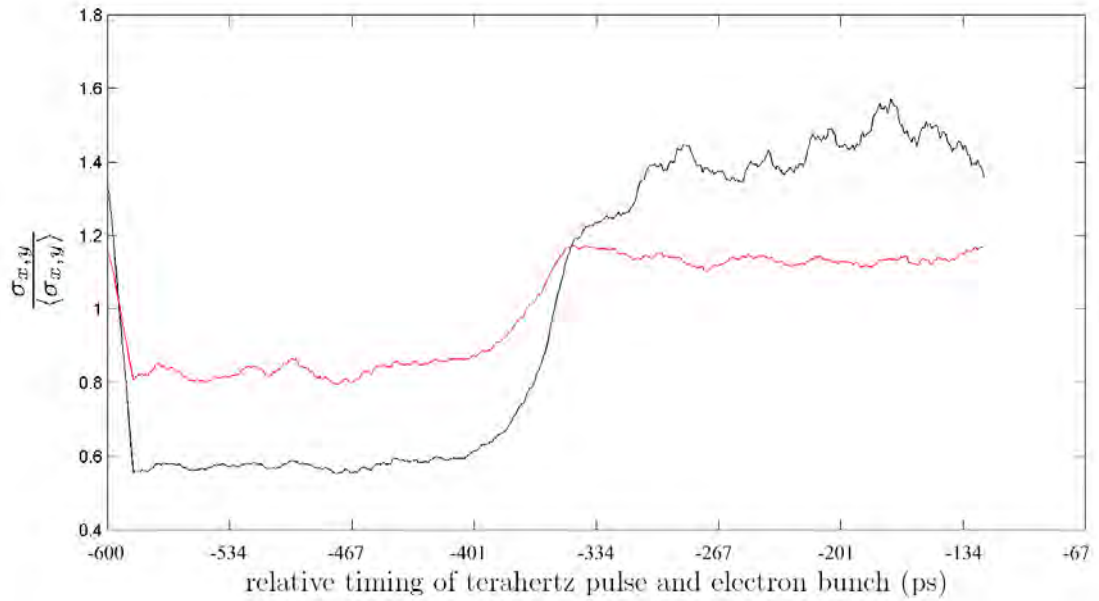


FIGURE 5.31: The effect of a sudden accelerator global phase shift on the horizontal and vertical beam sizes ( $\sigma_x$  and  $\sigma_y$ ) measured on the chicane YAG screen, during a scan of the relative timing of the electron bunch and the terahertz pulse. Each data point is a rolling average of five consecutive measurements, divided by the overall average.

Figure	Synchrolock phase	photodiode signal timing (ps)	terahertz pulse timing (ps)
5.32	28,800	-3540	-2370
5.33	30,850	-2770	-1600
5.34	33,410	-2000	-830
5.35	34,842	-1230	< 60
5.36	36,500	-460	710
5.37	38,000	310	1480

TABLE 5.7: Experimental data sets recorded on 6/11/11. A positive value for the photodiode signal timing indicates that it is measured on the 'scope to be before the electron BPM signal; a positive value for the terahertz pulse timing indicates that the terahertz pulse arrives before the electron bunch in Straight 2.

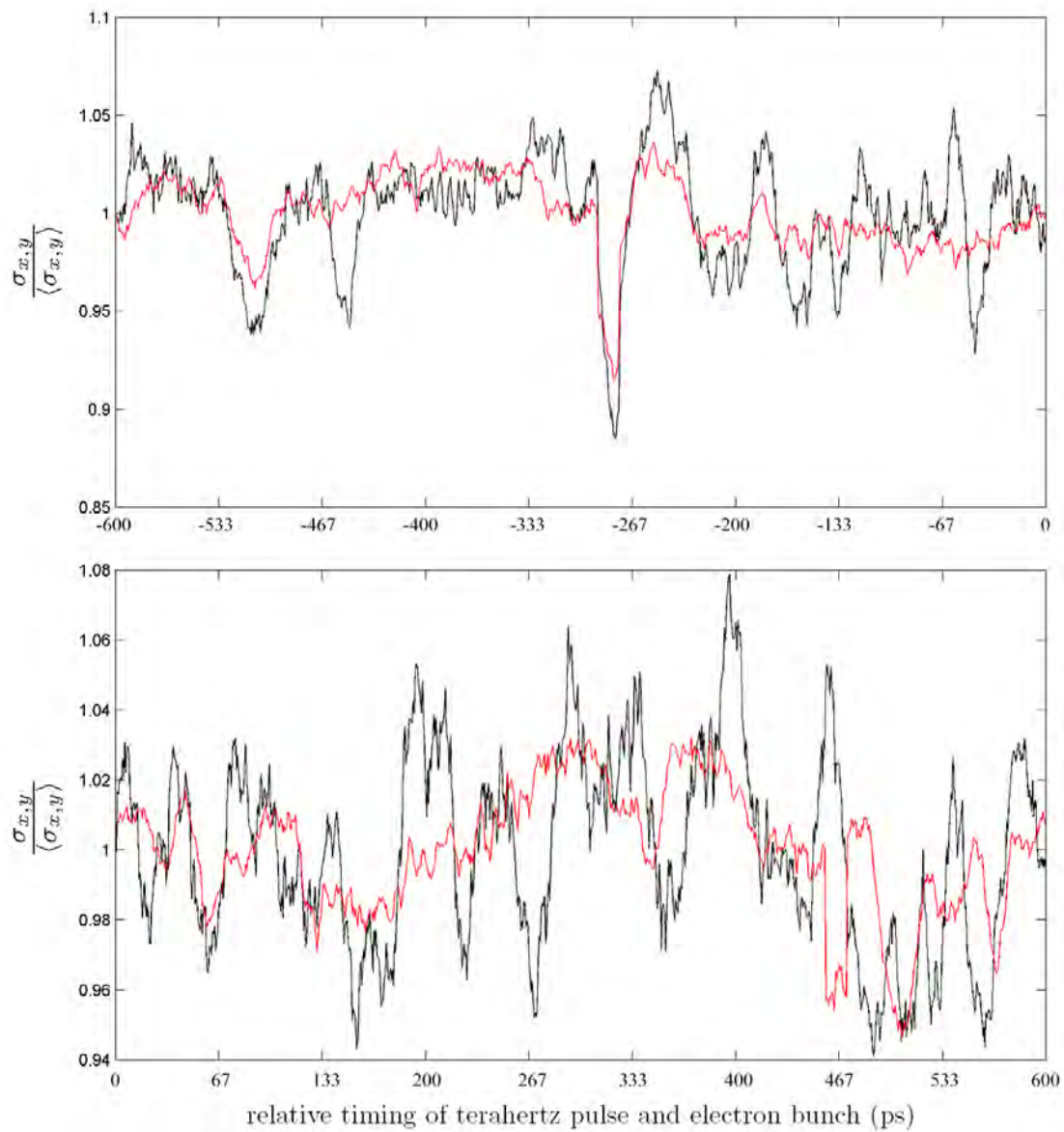


FIGURE 5.32: The horizontal (black) and vertical (red) beam sizes ( $\sigma_x$  and  $\sigma_y$ ) on the chicane YAG screen, as a function of the relative timing of the electron bunch and the terahertz pulse. Each data point is a rolling average of five consecutive measurements, divided by the overall average. The terahertz pulse is 2370 ps after the electron bunch in Straight 2.

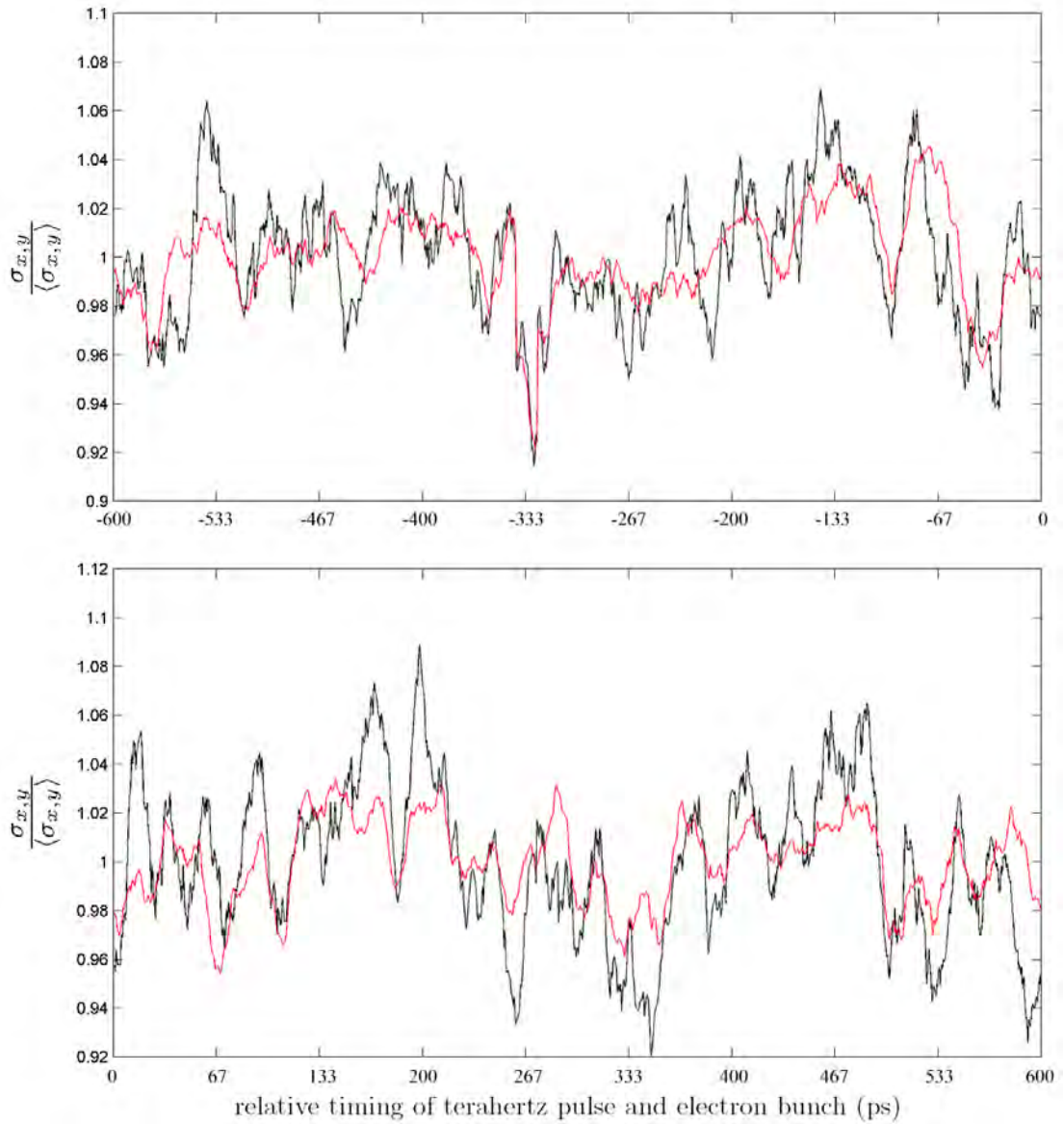


FIGURE 5.33: The horizontal (black) and vertical (red) beam sizes ( $\sigma_x$  and  $\sigma_y$ ) on the chicane YAG screen, as a function of the relative timing of the electron bunch and the terahertz pulse. Each data point is a rolling average of five consecutive measurements, divided by the overall average. The terahertz pulse is 1600 ps after the electron bunch in Straight 2.

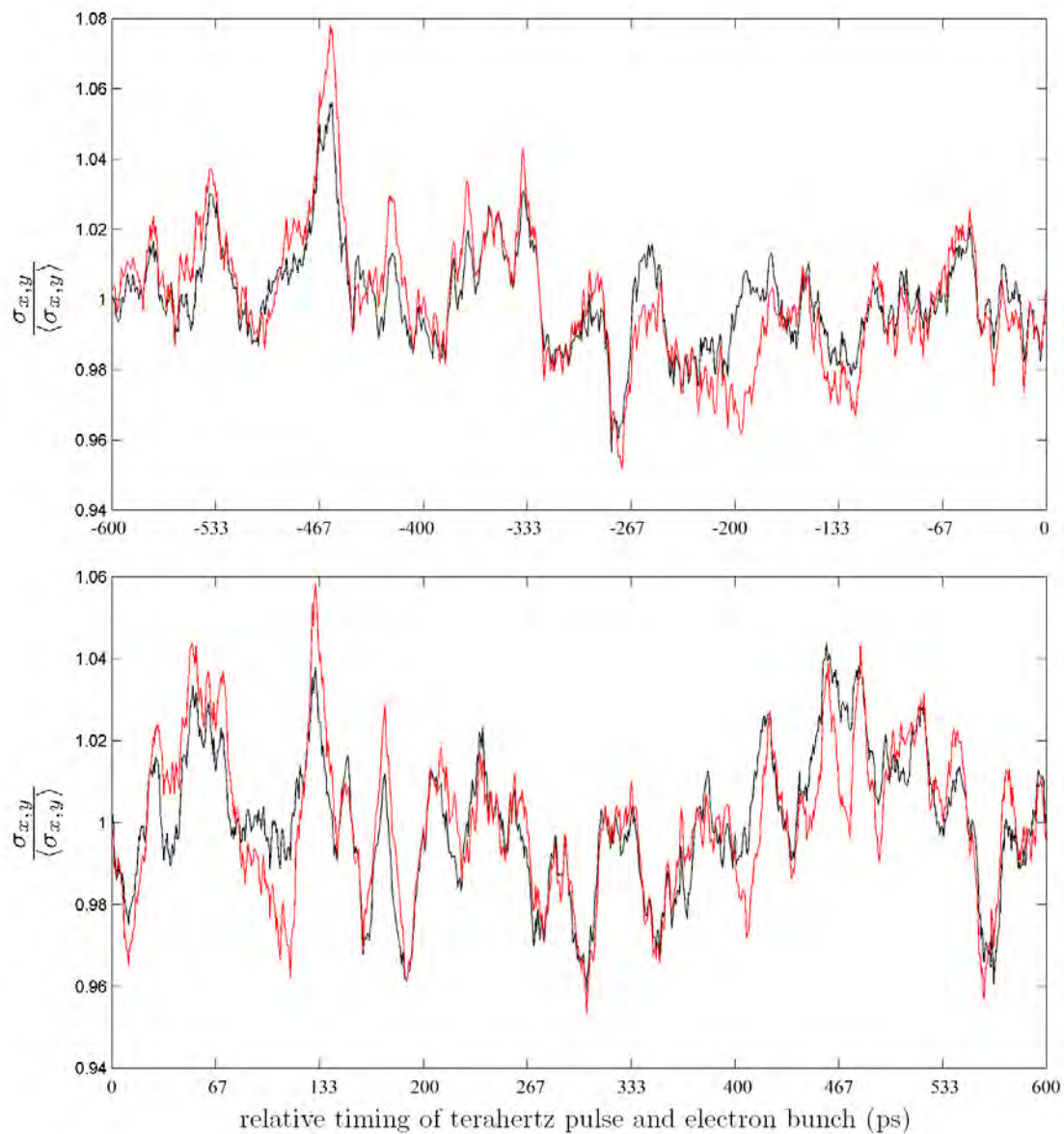


FIGURE 5.34: The horizontal (black) and vertical (red) beam sizes ( $\sigma_x$  and  $\sigma_y$ ) on the chicane YAG screen, as a function of the relative timing of the electron bunch and the terahertz pulse. Each data point is a rolling average of five consecutive measurements, divided by the overall average. The terahertz pulse is 830 ps after the electron bunch in Straight 2.

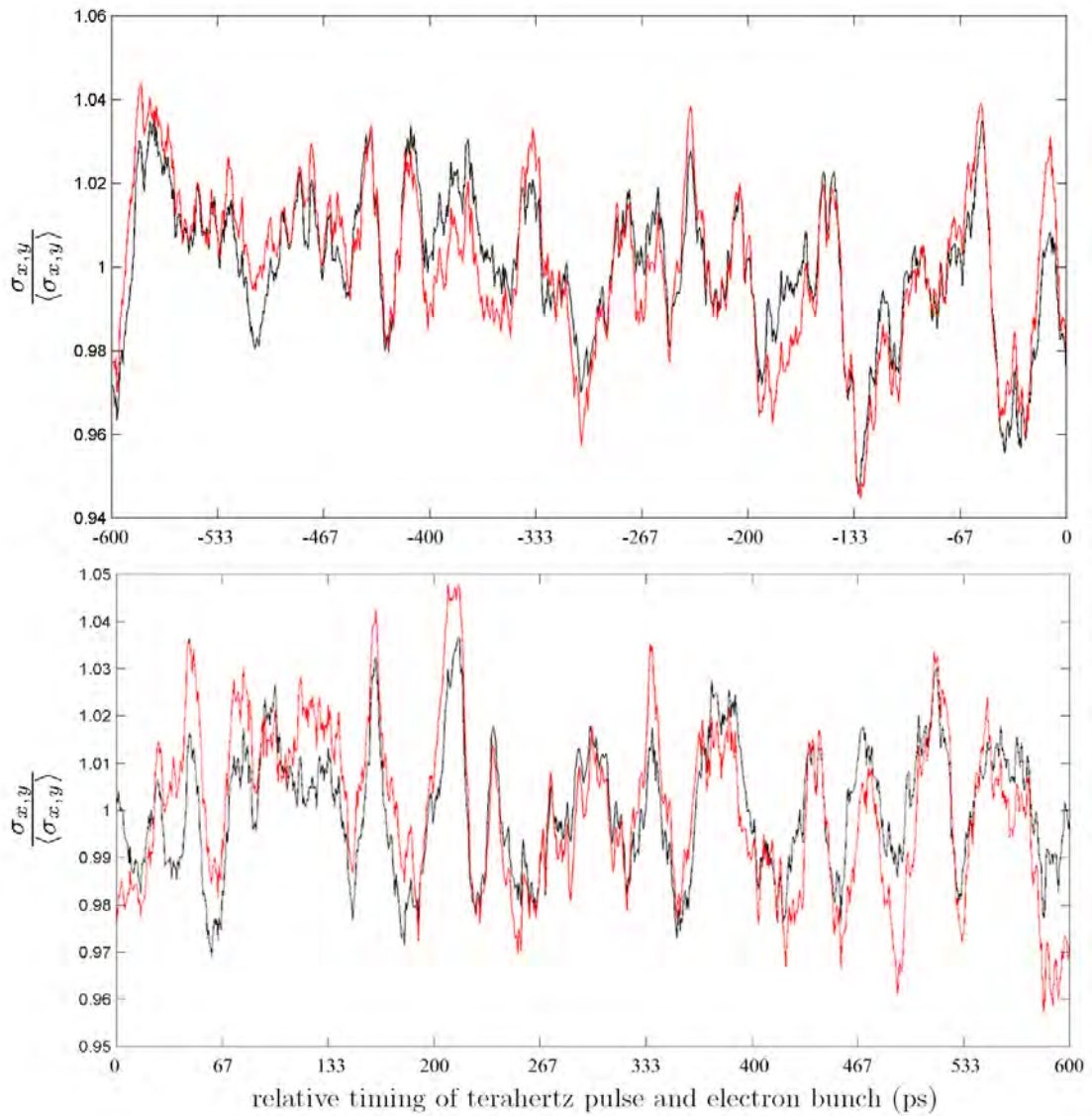


FIGURE 5.35: The horizontal (black) and vertical (red) beam sizes ( $\sigma_x$  and  $\sigma_y$ ) on the chicane YAG screen, as a function of the relative timing of the electron bunch and the terahertz pulse. Each data point is a rolling average of five consecutive measurements, divided by the overall average. The time window includes temporal overlap of the terahertz pulses and electron bunches in Straight 2 and is thus when we would have expected to have seen an interaction signal.

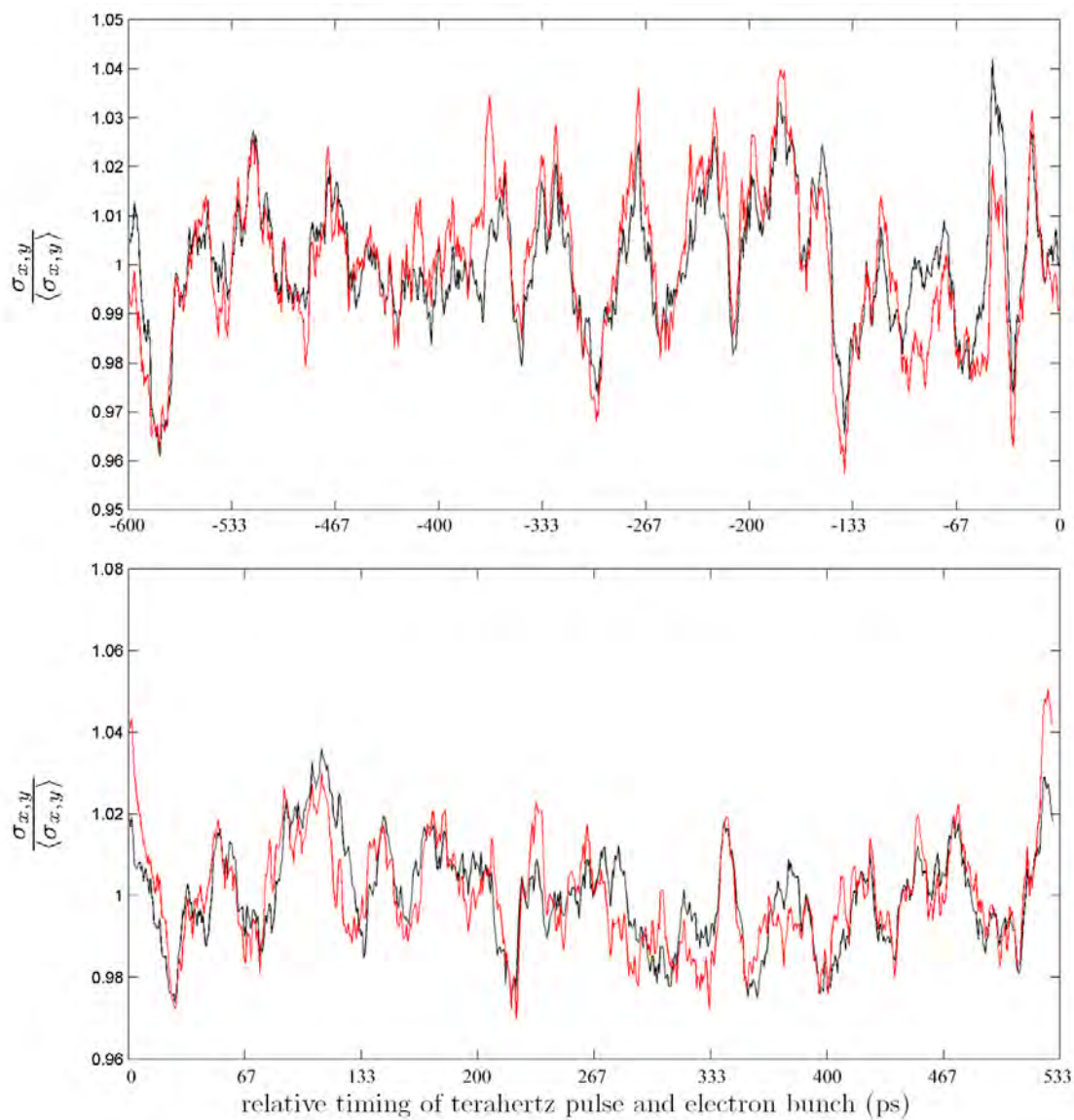


FIGURE 5.36: The horizontal (black) and vertical (red) beam sizes ( $\sigma_x$  and  $\sigma_y$ ) measured on the chicane YAG screen, as a function of the relative timing of the electron bunch and the terahertz pulse. Each data point is a rolling average of five consecutive measurements, divided by the overall average. The terahertz pulse is 710 ps before the electron bunch in Straight 2.

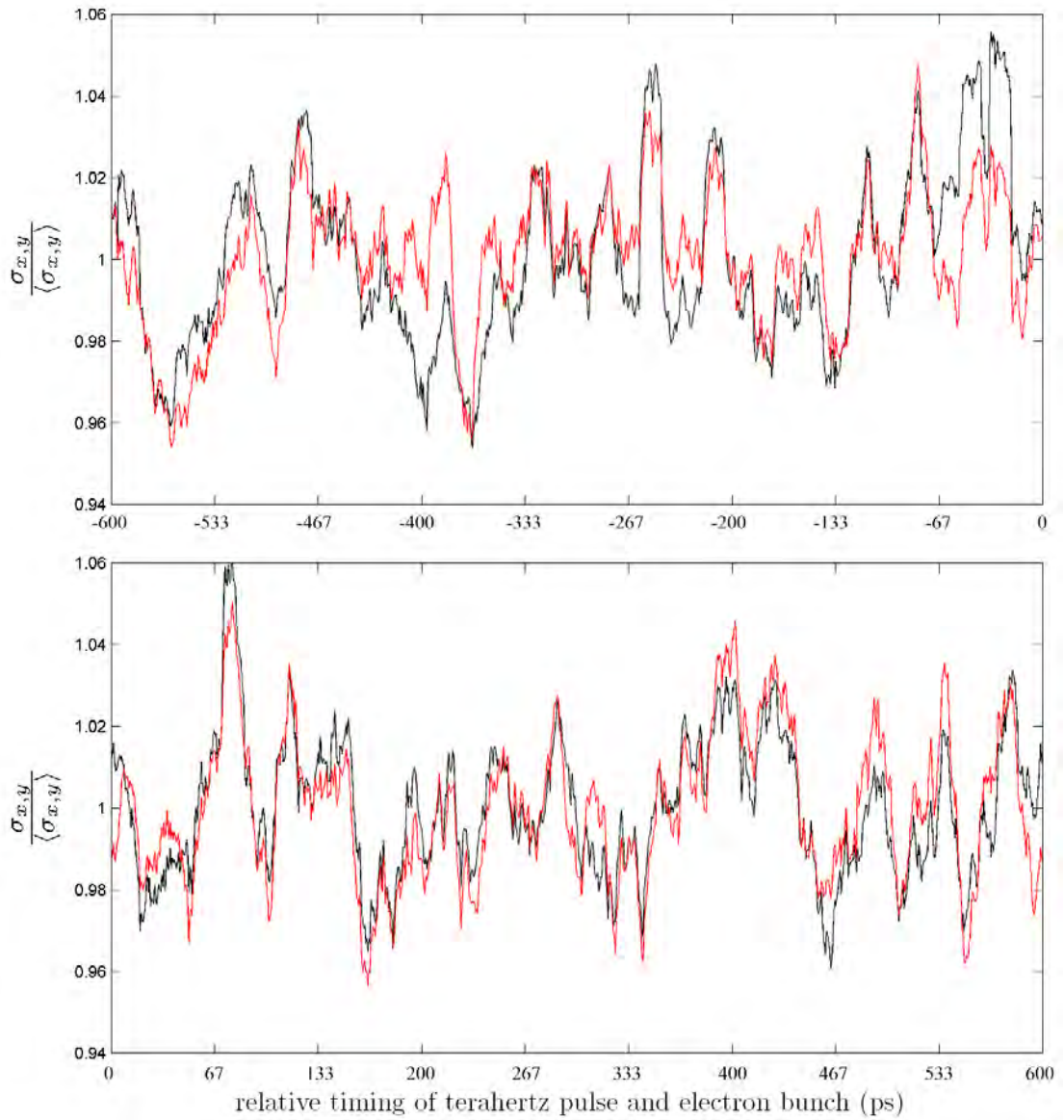


FIGURE 5.37: The horizontal (black) and vertical (red) beam sizes ( $\sigma_x$  and  $\sigma_y$ ) measured on the chicane YAG screen, as a function of the relative timing of the electron bunch and the terahertz pulse. Each data point is a rolling average of five consecutive measurements, divided by the overall average. The terahertz pulse is 1480 ps before the electron bunch in Straight 2.

### 5.4.3 Measurements on 24/11/11

A second opportunity was available to look for an interaction signal, with the position of the terahertz focus an additional experimental variable, following the installation of motorized stage for lens (12). Data were collected with the terahertz forming a focus at the nominal interaction point (coincident with the ZnTe crystal used to measure the terahertz electric field strength) and with the focus being formed at the mirror (ST2-LM-MIR-01), in Straight 2. Unfortunately further problems with the operation of the high-voltage pulser and the antenna meant that the data were collected at a voltage of only 30 kV. With the same set up and cable lengths used in the earlier synchronization measurements, a Coherent Synchrolock-AP fundamental phase value of 37670 gave the laser diode signal 45 ps in advance of the BPM.

Figure 5.38 shows the horizontal and vertical sizes ( $\sigma_x$  and  $\sigma_y$ ) of the beam image recorded on the chicane YAG screen (ST2-DIA-YAG-01) whilst the optical delay line stage is driven from -100 to +100 mm in steps of 0.15 mm. The Synchrolock fundamental phase is at 34800, so that the laser diode signal is 1300 ps after the BPM signal, which corresponds to approximate overlap of the terahertz and the electrons within Straight 2. The lens (12) focus stage is at 190 mm, so that the terahertz focus is at the nominal interaction point. Each data point is a rolling average of five consecutive measurements, divided by the overall average.

Figure 5.39 shows the horizontal and vertical sizes ( $\sigma_x$  and  $\sigma_y$ ) of the beam image recorded on the chicane YAG screen (ST2-DIA-YAG-01) whilst the optical delay line

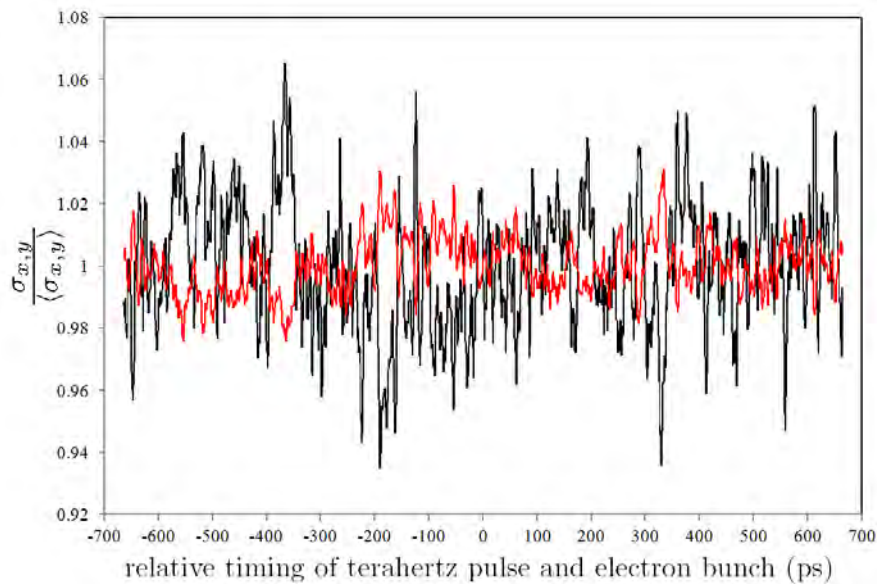


FIGURE 5.38: The horizontal (black) and the vertical (red) beam sizes ( $\sigma_x$  and  $\sigma_y$ ) on the chicane YAG screen as a function of the relative timing of the electron bunch and the terahertz pulse. Each data point is a rolling average of five consecutive measurements, divided by the overall average. The terahertz focus at the nominal interaction location and the time window includes the temporal overlap of the terahertz pulses and electron bunches.

stage is driven from -50 to +50 mm, in steps of 0.15 mm. The Synchrolock fundamental phase is at 34800, so that the laser diode signal is 1300 ps after the BPM signal, which corresponds to approximate overlap of the terahertz and the electrons within Straight 2. The lens (12) focus stage is now at 220 mm, so that the terahertz focus is approximately on the mirror ST2-LM-MIR-01 inside the accelerator vacuum envelope.

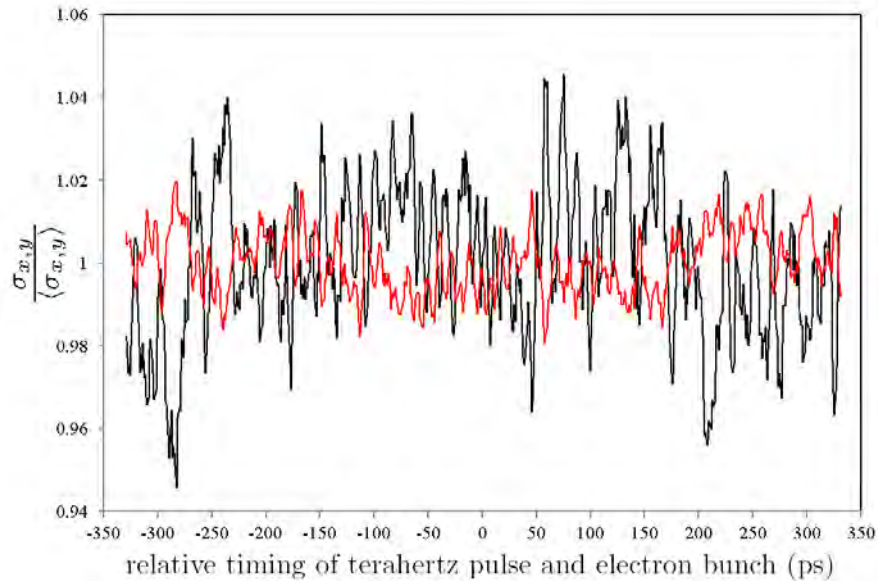


FIGURE 5.39: The horizontal (black) and the vertical (red) beam sizes ( $\sigma_x$  and  $\sigma_y$ ) on the chicane YAG screen as a function of the relative timing of the electron bunch and the terahertz pulse. Each data point is a rolling average of five consecutive measurements, divided by the overall average. The terahertz focus is approximately on the mirror ST2-LM-MIR-01 and the time window includes the temporal overlap of the terahertz pulses and electron bunches.

Figure 5.40 shows data recorded with the same conditions as figure 5.39, except the aperture plate is withdrawn; its purpose is to stop terahertz propagation beyond the interaction point.

Figure 5.41 shows data recorded with the same conditions as figure 5.39, except this time the pump laser was stopped (so there can be no terahertz present in the accelerator).

Again here is no evidence of a change in the electron beam size in figure 5.38 or figure 5.39, where it would be expected to be seen if there had been any interaction, even after careful analysis of the data to improve the signal-to-noise ratio. Neither is there any noticeable difference when the aperture plate is removed or the laser stopped. Considering that these measurements were made with an antenna voltage of only 30 kV, compared to 45 kV for the previous set of measurements (when nothing was seen either) this was not a great surprise.

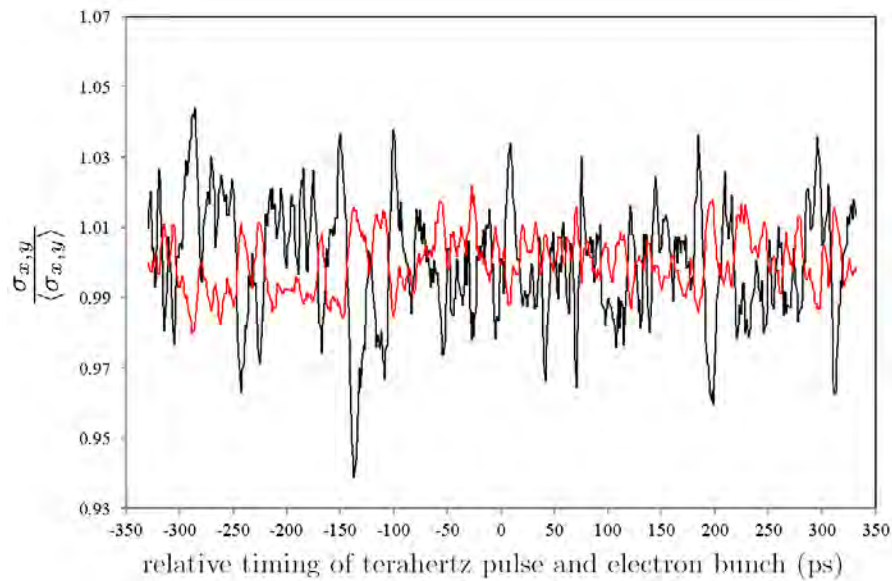


FIGURE 5.40: The horizontal (black) and the vertical (red) beam sizes ( $\sigma_x$  and  $\sigma_y$ ) on the chicane YAG screen as a function of the relative timing of the electron bunch and the terahertz pulse. Each data point is a rolling average of five consecutive measurements, divided by the overall average. The terahertz focus is approximately on the mirror ST2-LM-MIR-01 and the time window includes the temporal overlap of the terahertz pulses and electron bunches. The aperture plate is not present.

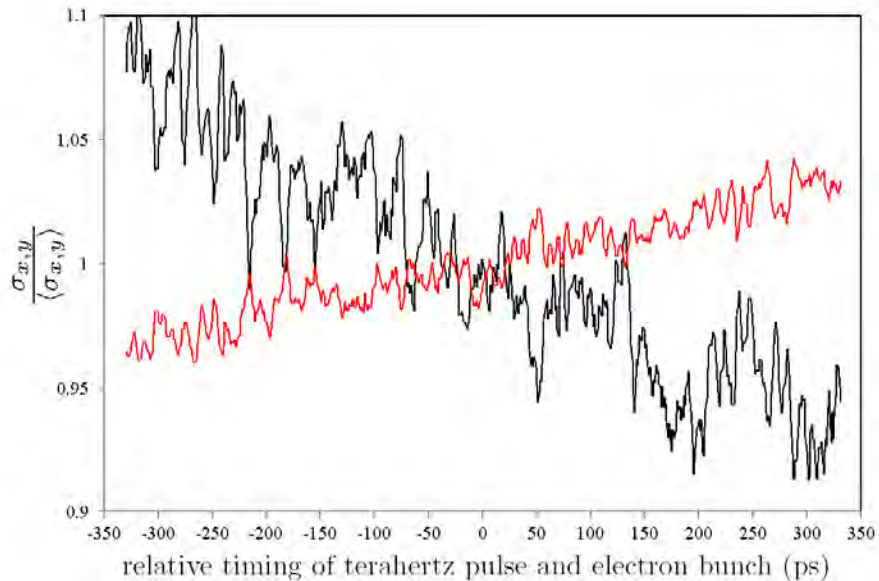


FIGURE 5.41: The horizontal (black) and the vertical (red) beam sizes ( $\sigma_x$  and  $\sigma_y$ ) on the chicane YAG screen as a function of the relative timing of the electron bunch and the terahertz pulse. Each data point is a rolling average of five consecutive measurements, divided by the overall average. The terahertz focus is approximately on the mirror ST2-LM-MIR-01 and the time window includes the temporal overlap of the terahertz pulses and electron bunches in Straight 2. The aperture plate is in place but the pump laser is off, so no terahertz can be present.

## 5.5 Chapter summary

This chapter has recorded the experimental work done with the ALICE accelerator, for both establishing in-situ terahertz generation and measurement, and searches for interaction between the terahertz radiation and the electron beam. The measurements of the terahertz electric field strength generated within the ALICE accelerator hall were not easy to reconcile with the expectation described in chapter 1 or the results recorded in chapter 3 in the Diagnostics Room. The reduced-energy operating regime for ALICE identified in chapter 4 was successfully established and verified. Unfortunately the experimental searches for an interaction between the terahertz radiation and the electron beam were apparently unsuccessful.



## Chapter 6

# Summary and Conclusions

### 6.1 Introduction

This thesis describes the work done in preparation for the demonstration of free-space interaction of terahertz radiation with relativistic electrons, while this chapter is an analysis of what was achieved and what might be possible in the future.

A new terahertz-generating antenna system including an optimized electrode profile and pulsed HV power supply was developed, that could be operated routinely at 130 kV. The electrode profile was developed via extensive modelling in Opera 2D. The antenna design prior to this optimization could only be operated at less than 10 kV before breakdown occurred. This (greater than one order of magnitude) increase in the operating voltage resulted in a significant increase in the electric field strength of the terahertz radiation produced.

We have operated a robust and repeatable procedure to measure the electric field strength of a radially-polarized terahertz pulse in the ALICE Diagnostic Room, for radiation produced by the electrical breakdown of a radially-symmetric photoconductive antenna; furthermore this method has been used to characterize the improved antenna design. Detailed measurements of the properties of the emitted radiation were made.

The ALICE accelerator at Daresbury Laboratory was modified in order to enable the interaction of terahertz radiation with relativistic electrons and also to detect the results of said interaction. A new set of accelerator and beam parameters, for both transverse and longitudinal properties, was developed which were favourable to the success of the experiment. A method for re-establishing the accelerator set up reliably was developed.

A second terahertz-generation facility was built inside the ALICE experimental hall, replicating the one in the ALICE Diagnostic Room.

Finally, two attempts were made to detect an induced energy modulation in a specially configured electron beam, following its interaction with terahertz radiation generated in the ALICE accelerator hall. Even without a positive result, these experiments served as a test of the full system, enabling us to gain valuable experience and identify those areas of the experiment that would benefit from improved equipment, methods or understanding in future studies.

## 6.2 Is there any signal demonstrating interaction between terahertz radiation and electron bunches?

Despite carefully processing the data (examples of which are shown in figures 5.32 to 5.40) by averaging to reduce the noise level, looking for changes in the aspect ratio of the beam image and more, there does not appear to be a visible interaction signal in the data. Although it may have been possible, under the most favourable circumstances, to have observed an interaction signal already, the complexity of the experiment means that it is not surprising that further improvements and optimizations are needed before evidence of an interaction is obtained. The work done so far, leading to the full system tests reported in Chapter 5, has been essential in allowing us to identify and prioritize areas for improvement.

## 6.3 Why did we not see a signal demonstrating interaction?

The possible reasons why we did not see any sign of an interaction between the terahertz radiation and electron bunches include:

1. The noise level on the experimental measurements was such that the interaction signal was not visible, even after extensive processing of the data;
2. The electric field strength of the terahertz radiation inside the ALICE accelerator was not as large as that predicted by simulation or measured in the ALICE Diagnostics Room, thus leading to a smaller interaction signal;
3. The required spatial alignment of the terahertz radiation and electron bunches was not achieved;
4. Temporal overlap of the terahertz pulses and electron bunches was not achieved in any of the timing windows we used.

Each of these is explored in detail in the subsequent sections and potential future improvements in the equipment and methods used are identified.

### 6.3.1 Poor signal-to-noise ratio

To improve the signal-to-noise ratio the possible options are self-evident:

- Increase the signal size;
- Reduce the experimental noise level.

The two sets of data acquired while looking for an interaction signal were recorded with an antenna voltage of 45 and 30 kV. This should be compared to the highest voltage achieved reliably in the ALICE Diagnostics Room measurements of 130 kV. The reason

for using 45 and 30 kV was partially due to the fact that the antenna had been used extensively in the ALICE Diagnostics Room and many small breakdowns had led to an accumulation of defects on the wafer itself which served to limit the voltage that it could hold off. Incorrect triggering of the high-voltage pulsed power supply also reduced the operating voltage. To increase the terahertz radiation electric field strength the following steps can be taken in future experiments:

1. Use a new antenna assembly to maximize the voltage that can be applied before it breaks down;
2. Operate the HV pulser at its full capacity;
3. Use a different HV pulser that will provide shorter pulses which should allow higher voltages to be achieved without breakdown;
4. Experiment with the proposed improved centre electrode profile that will allow a higher voltage across the wafer for the same maximum field on the wafer surface.

Another method of increasing the signal size would be to reduce the electron beam energy further below that used in these experiments (22.5 MeV). Assuming that the interaction with the terahertz pulse gives a fixed absolute energy modulation to the electrons, the relative energy modulation is larger at lower beam energy. When viewed at a dispersive position in the lattice, this will result in a larger beam size modulation. However, a lower beam energy will result in a larger geometric emittance and relative energy spread, and some apparent increase in the beam instability.

The main source of noise is the train-to-train variation in the ALICE beam properties; particularly beam energy. This leads to small changes in position of the electron beam on the screens (due to dispersion) and small changes in beam size (due to changed focussing by the quadrupoles as the beam trajectory moves). This train-to-train beam variation can be eliminated by using gated cameras to capture the image of two electron bunches in the same train; one without terahertz present and one with. Initial experiments have already been undertaken (the results of which were obtained too late to be included in this thesis) to prove that this concept can be implemented successfully. It has been demonstrated that single bunches can be produced in a single ALICE bunch train with sufficient time interval (of order a few 100 ns) that the light from the YAG screen has decayed sufficiently to record independent images of each bunch. Furthermore, the arrangement of two gated cameras, each triggered with sufficient accuracy to capture these independent images from the same screen, has also been demonstrated.

### **6.3.2 Apparent failure to replicate the terahertz radiation electric field strength measured in the ALICE Diagnostics Room inside the ALICE accelerator**

A number of possible explanations for this have been identified; some of which have already been experimentally tested since the work recorded in this thesis was completed:

- Either the terahertz radiation does not come to as small a focus inside the accelerator's beam tube as it does on the optical bench in the ALICE Diagnostics Room or the focus is not in the same longitudinal position;
- The temporal characteristics of the terahertz pulses are not preserved within the accelerator;
- The temporal characteristics of the probe laser beam are not preserved within the accelerator, leading to an apparent (but spurious) measured degradation in the temporal characteristics of the terahertz pulses;
- The polarization state of the probe laser beam is not preserved within the accelerator, leading to further apparent (but spurious) measured degradation in the terahertz pulses structure;
- The polarization state of the terahertz pulses is not preserved within the accelerator, leading to a reduced electric field in the required direction at the interaction point with the electrons.

The first of these points is the most interesting and the one at which most experimental effort was directed since the completion of the interaction measurements described in this thesis. The experimental results shown in figures 5.15 and 5.16 do not suggest the terahertz beam is forming a focus at a different position to that expected; instead the measurements indicate a very weak degree of focussing. The Rayleigh length of the terahertz focus should be several centimetres, so it is unlikely that we did not have the focus on the ZnTe crystal for any of these data sets, or detect proximity to it. There has been no adequate resolution of this question to date.

Some work was also undertaken to determine whether the terahertz pulse would propagate inside the ALICE accelerator beam tube without disruption; there was no strong indication that it would not.

The results in figure 5.4 clearly show that the polarization state of the probe laser beam is not preserved following passage through the accelerator. This could be due to birefringence in the entrance and exit windows of the accelerator, or (more speculatively) scattering off optical elements and other components within or near the beam path. Particular attention has been given to the hole in the centre of the mirror ST2-LM-MIR-01, which may provide several surfaces for stray probe laser reflections. Some of these would continue in the general direction of the ZnTe crystal following multiple reflections from the inside the ALICE accelerator beam tube.

The complex temporal profile of the terahertz pulse, as measured in the accelerator, in contrast to that measured in the ALICE Diagnostics Room, is still difficult to explain. This could be due to our measurements not being made at the focus of the terahertz beam (for the reasons proposed above), disruption to the polarization state of the terahertz pulses or probe laser beam, some factor not yet identified, or a combination of all of these. Further experimental work in the ALICE Diagnostics Room and the ALICE

accelerator hall, to achieve further convergence of the two set-ups, is needed to answer that question.

### **6.3.3 Inadequate spatial alignment of the terahertz radiation and the electron beam**

Following the careful alignment of the various accelerator components in ALICE Straight 2 (that interacted with either the electron beam, the terahertz radiation, or both) a reproducible method was developed to steer the electron beam along an axis defined by these components. The optical system alignment was checked before each experiment. Furthermore, measurements were made of the terahertz electric field strength on the ZnTe crystal inside the accelerator as a function of ITO steering (figures 5.10 and 5.11). Such measurements would have identified any mis-alignment of the terahertz pulses, however they did not. Therefore it is not thought that spatial alignment of the two beams was a limiting factor.

### **6.3.4 Inadequate synchronization**

Although there was no obvious reason to doubt the reliability of our method of obtaining synchronization of the terahertz pulses and the electron bunches within the accelerator, a number of adjacent time windows were probed when looking for the interaction signal, making the the experiment quite lengthy. Future experiments may use a streak camera to ascertain the relative timing of the terahertz pulses and the electron bunches within the accelerator, which will provide improved accuracy compared to the present method. This should allow efforts to observe an interaction signal to focus on narrower time windows, which in turn should allow more detailed and careful observations (e.g. using greater levels of averaging) to be made.

## **6.4 Chapter summary**

We do not believe that at the present stage, there is evidence of an interaction between terahertz pulses and electron bunches in ALICE. However, the combination of the experimental experience that has been gained, along with the apparatus that has been developed, stand us in good stead to achieve a positive result in the next period of experimentation.



# Bibliography

- [1] ALICE, (Accelerators and Lasers In Combined Experiments). URL <http://www.stfc.ac.uk/ASTeC/Programmes/Alice/35997.aspx>.
- [2] LCLS design study report, January 1999. URL <http://www.slac.stanford.edu/pubs/slacreports/slac-r-521.html>.
- [3] L. -H. Yu, M. Babzien, I. Ben-Zvi, L. F. DiMauro, A. Doyuran, W. Graves, E. Johnson, S. Krinsky, R. Malone, I. Pogorelsky, J. Skaritka, G. Rakowsky, L. Solomon, X. J. Wang, M. Woodle, V. Yakimenko, S. G. Biedron, J. N. Galayda, E. Gluskin, J. Jagger, V. Sajaev, and I. Vasserman. High-Gain Harmonic Generation Free-Electron Laser. *Science*, 289:932, 2000.
- [4] R. W. Schoenlein, S. Chattopadhyay, H. H. W. Chong, T. E. Glover, P. A. Heimann, C. V. Shank, A. A. Zholents, and M. S. Zolotarev. Generation of femtosecond pulses of synchrotron radiation. *Science*, 287:2237, 2000.
- [5] D. J. Holder. First results from the ERL prototype (ALICE) at Daresbury. In *Proceedings of LINAC'08*, 2008.
- [6] J. D. Lawson. Lasers and accelerators. *IEEE Trans. Nucl. Sci.*, 26(3):4217, 1979.
- [7] P. M. Woodward. A method of calculating the field over a plane aperture required to produce a given polar diagram. *J. Inst. Electr. Eng.*, 93:1554, 1947.
- [8] A. L. Troha, J. R. Van Meter, E. C. Landahl, R. M. Alvis, Z. A. Unterberg, K. Li, N. C. Lurmann, jr, A. K. Kerman, and F. V. Hartemann. Vacuum electron acceleration by coherent dipole radiation. *Phys. Rev. E*, 60(1):926, 1999.
- [9] J. X. Wang, W. Scheid, M. Hoelss, and Y. K. Ho. Comment on "Vacuum electron acceleration by coherent dipole radiation". *Phys. Rev. E*, 6, 2002.
- [10] E. Esarey, P. Sprangle, and J. Krall. Laser acceleration of electrons in vacuum. *Phys. Rev. E*, 52(5):5443, 1995.
- [11] D. Lin, Q. Kong, Z. Chen, P. X. Wang, J. J. Xu, and Y. K. Ho. Scaling laws of electron acceleration driven by an intense laser pulse. *Appl. Phys. B*, 89:549, 2007.
- [12] Y-K. Ho. Absence of net acceleration of charged particles by a focused laser beam in free space. *Phys. Lett. A*, 184:440, 1994.

- 
- [13] R. B. Palmer. Interaction of relativistic particles and free electromagnetic waves in the presence of a static helical magnet. *J. Appl. Phys.*, 43(7):3014, 1972.
- [14] J. A. Edighoffer, W. D. Kimura, R. H. Pantell, M. A. Piestrup, and D. Y. Wang. Observation of inverse Cherenkov interaction between free electrons and laser light. *Phys. Rev. A*, 23(4):1848, 1981.
- [15] T. Tajima and J. M. Dawson. Laser electron accelerator. *Phys. Rev. Lett.*, 43(4):267, 1979.
- [16] T. Plettner, R. L. Byer, and C. McGuinness. Photonic-based laser driven electron beam deflection and focusing structures. *PRST - AB*, 12, 2009.
- [17] Z. Huang, G. Stupakov, and M. Zolotarev. Calculation and optimization of laser acceleration in vacuum. *PRST - AB*, 7, 2004.
- [18] F. Caspers and E. Jensen. Particle acceleration with the axial electric field of a TEM<sub>10</sub> mode laser beam. *CERN/PS*, 89-69, 1989.
- [19] M. O. Scully and M. S. Zubairy. Simple laser accelerator: optics and particle dynamics. *Phys. Rev. A*, 44(4):2656, 1991.
- [20] S. Liu, H. Guo, H. Tang, and M. Liu. Direct acceleration of electrons using single Hermite-Gaussian beam and Bessel beam in vacuum. *Phys. Lett. A*, 324:104, 2004.
- [21] P. X. Wang, Y. K. Ho, X. Q. Yuan, Q. Kong, N. Cao, A. M. Sessler, E. Esarey, and Y. Nishida. Vacuum electron acceleration by an intense laser. *Appl. Phys. Lett.*, 78(15):2253, 2001.
- [22] H. Zhang, S. Liu, and H. Guo. Direct acceleration of electrons by intense crossed Hermite-Gaussian laser beams. *Phys. Lett. A*, 367:402, 2007.
- [23] F. Zhou, D. Cline, Y. Ho, K. Kusche, I. Pogorelsky, L. Shao, and V. Yakimenko. Experimental test for novel vacuum laser acceleration at the BNL-ATF. *Adv. Acc. Concepts*, 11<sup>th</sup> Workshop, CP737.
- [24] Y. I. Salamin. Fields of a radially polarized Gaussian laser beam beyond the paraxial approximation. *Opt. Lett.*, 31(17):2619, 2006.
- [25] Y. I. Salamin. Mono-energetic GeV electrons from ionization in a radially polarized laser beam. *Opt. Lett.*, 32(1):90, 2007.
- [26] S. C. Tidwell, D. H. Ford, and W. D. Kimura. Generating radially polarized beams interferometrically. *Appl. Opt.*, 29(15):2234, 1990.
- [27] Y. I. Salamin. Low-diffraction direct particle acceleration by a radially polarized laser beam. *Phys. Lett. A*, 374:4950, 2010.

- [28] S. Quabis, R. Dorn, M. Eberler, O. Glöckl, and G. Leuchs. Focusing light to a tighter spot. *Opt. Comms.*, 179:1, 2000.
- [29] R. Dorn, S. Quabis, and G. Leuchs. Sharper focus for a radially polarized light beam. *Phys. Rev. Lett.*, 91(23), 2003.
- [30] D. H. Auston. Picosecond optoelectronic switching and gating in silicon. *Appl. Phys. Lett.*, 26(3):101, 1975.
- [31] B. B. Hu, J. T. Darrow, X. C. Zhang, and D. H. Auston. Optically steerable photoconducting antennas. *Appl. Phys. Lett.*, 56(10):886, 1990.
- [32] D. You, R. R. Jones, and P. H. Bucksbaum. Generation of high-power sub-single-cycle 500-fs electromagnetic pulses. *Opt. Lett.*, 18(4):290, 1993.
- [33] J. H. Sun, J. G. Gallacher, N. Limos, R. Issac, J. M. Dias, Z. X. Huang, and D. A. Jaroszynski. High energy terahertz pulse emission from GaAs illuminated by a femtosecond laser. *Proc of SPIE*, 6840:68401B–1, 2008.
- [34] S. P. Jamison, B. Ersfeld, and D. A. Jaroszynski. Role of propagating ionisation fronts in semiconductor generation of sub-ps THz radiation. *Curr. Appl. Phys.*, 4: 217, 2004.
- [35] J. A. Deibel, M. D. Escarra, and D. M. Mittleman. Photoconductive terahertz antenna with radial symmetry. *Elect. Lett.*, 41(5):226, 2005.
- [36] J. A. Deibel, K. Wang, M. D. Escarra, and D. M. Mittleman. Enhanced coupling of terahertz radiation to cylindrical wire waveguides. *Opt. Exp.*, 14(1):279, 2006.
- [37] S. Winnerl, B. Zimmermann, F. Peter, H. Schneider, and M. Helm. Terahertz vector beams. In *Proceedings of 33<sup>rd</sup> International Conference on Infrared, Millimeter and Terahertz Waves*, 2008.
- [38] E. Budiarto, J. Margolies, S. Jeong, and J. Son. High-intensity terahertz pulses at 1-kHz repetition rate. *IEEE J. Quan. Elec.*, 32(10):1839, 1996.
- [39] K. Wynne and J. J. Carey. An integrated description of terahertz generation through optical rectification, charge transfer, and current surge. *Opt. Comms.*, 256:400, 2005.
- [40] V. N. Trukhin, A. V. Andrianov, and N. N. Zinov'ev. Generation of terahertz radiation by a photoconductive antenna. *Acta Phys. Pol. A*, 113(3):921, 2008.
- [41] G. Rodriguez, S. R. Caceres, and A. J. Taylor. Modeling of terahertz radiation from biased photoconductors: transient velocity effects. *Opt. Lett.*, 19(23):1994, 1994.
- [42] P. K. Benicewicz, J. P. Roberts, and A. J. Taylor. Scaling of terahertz radiation from large-aperture biased photoconductors. *JOSA B*, 11(12):2533, 1994.

- 
- [43] A. Gürtler, C. Winnewisser, H. Helm, and P. U. Jepsen. Terahertz pulse propagation in the near field and the far field. *JOSA A*, 17(1):74, 2000.
- [44] E. Budiarto, N. W. Pu, S. Jeong, and J. Bokor. Near-field propagation of terahertz pulses from a large-aperture antenna. *Opt. Lett.*, 23(3):213, 1998.
- [45] J. D. Jackson. *Classical Electrodynamics*. John Wiley and Sons, 3<sup>rd</sup> edition, 1998.
- [46] S. P. Jamison. The electro-optic effect for intense terahertz pulses. *Appl. Phys. B*, 91:241, 2008.
- [47] N. C. J. van der Valk, T. Wenckebach, and P. C. M. Planken. Full mathematical description of electro-optic detection in optically isotropic crystals. *JOSA B*, 21(3):622, 2004.
- [48] M. van Exter, Ch. Fattinger, and D. Grischkowsky. Terahertz time-domain spectroscopy of water vapor. *Opt. Lett.*, 14(20):1128, 1989.
- [49] G. A. Kachickas and L. H. Fisher. Formative time lags of uniform field breakdown in N<sub>2</sub>. *Phys. Rev.*, 88(4):878, 1952.
- [50] G. H. Welsh, D. A. Turton, D. R. Jones, D. A. Jaroszynski, and K. Wynne. 200 ns pulse high-voltage supply for terahertz field emission. *Rev. Sci. Inst.*, 78, 2007.
- [51] Vector Fields Software, OPERA. URL <http://www.cobham.com/about-cobham/aerospace-and-security/about-us/antenna-systems/kidlington/products.aspx>.
- [52] MAD-8, Home Page. URL <http://hansg.home.cern.ch/hansg/mad/mad8/mad8.html>.
- [53] F. Löhl. Measurement of the transverse emittance at the VUV-FEL. Diploma thesis, Department of Physics of the University of Hamburg, May 2005.
- [54] D. J. Holder. Modification of the EMMA injection line to act as a full-energy electron beam diagnostic for ALICE. Technical Report 29, Cockcroft Institute, 2009.